FLUIDICALLY RECONFIGURABLE MICROWAVE SYSTEMS WITH CONDUCTIVE AND DIELECTRIC LIQUID MATERIALS

A Thesis Submitted to
the Graduate School of
İzmir Institute of Technology
in Partial Fulfillment of the Requirements for the Degree of

DOCTOR OF PHILOSOPHY

in Electronics and Communication Engineering

by
Anıl KARATAY

November 2024
İZMİR

We approve the thesis of **Anıl KARATAY**

Examining Committee Members:

Prof. Dr. Mustafa Aziz ALTINKAYA
Department of Electrical and Electronics Engineering, İzmir Institute of Technology

Prof. Dr. Alp KUŞTEPELİ
Department of Electrical and Electronics Engineering, İzmir Institute of Technology

Prof. Dr. Mustafa SEÇMEN
Department of Electrical and Electronics Engineering, Yaşar University

Prof. Dr. Mehmet Salih DİNLEYİCİ
Department of Electrical and Electronics Engineering, İzmir Institute of Technology

Assoc. Prof. Dr. Avni AKSOY
Institute of Accelerator Technologies, Ankara University

08 November 2024

Prof. Dr. Mustafa Aziz ALTINKAYA
Supervisor, Department of Electrical and
Electronics Engineering
İzmir Institute of Technology

Assoc. Prof. Dr. Fatih YAMAN
Co-Supervisor, Dept. of Electr. and Electron.
Engineering, İzmir Institute of Technology
ASTeC, UKRI-STFC Daresbury Laboratory

Prof. Dr. Mustafa Aziz ALTINKAYA
Head of the Department of
Electrical and Electronics Engineering

Prof. Dr. Mehtap EANES
Dean of the Graduate School

ACKNOWLEDGMENTS

First and foremost, I would like to express my deepest gratitude to my advisor, Assoc. Prof. Dr. Fatih Yaman, whose exceptional guidance, insight, and unwavering support have been instrumental in the completion of this thesis. I would also like to express my sincere gratitude to our department's current chair, Prof. Dr. Mustafa Aziz Altınkaya, for accepting my supervision to carry out solely the bureaucratic procedures of the graduate institute.

I owe thanks to my thesis progress committee members, Prof. Dr. Alp Kuştepeli and Prof. Dr. Mustafa Seçmen, for their valuable comments and constructive criticisms. I also thank Prof. Dr. Mehmet Salih Dinleyici and Assoc. Prof. Dr. Avni Aksoy for their valuable contributions and efforts in the thesis committee.

I would like to thank my friends Fatih Onay and Bilal Orkan Olcay for their friendship and motivational support. A special thanks to Enes Ataç for always being a steady source of motivation and good humor. I truly appreciate it.

I would like to extend my deepest gratitude to my family for their invaluable encouragement and love throughout this journey. My deepest thanks go to my wife, Tüluğ Karatay, for her unwavering patience, encouragement, and understanding. I am also profoundly grateful to my parents, Hülya Karatay and Eyup Karatay, whose guidance and belief in me have been a constant source of strength. To my father-in-law, Sabri Uğur Küçüköğüt, I am thankful for his steady support. Finally, I would like to thank my brother, Hüsnü Can Karatay, and my sisters-in-law, Aybüke Beşevli and Ayten Çuhacı, for their moral support. I am truly fortunate to have such a supportive family by my side.

ABSTRACT

FLUIDICALLY RECONFIGURABLE MICROWAVE SYSTEMS WITH CONDUCTIVE AND DIELECTRIC LIQUID MATERIALS

In this thesis, a detailed investigation is presented on the use of liquid-assisted microwave components to overcome the limitations of traditional electrical and optical reconfiguration methods. First of all, a new dual-port antenna operating at 6.6 GHz and 7 GHz is proposed, prioritizing miniaturization and low computational load. The most important feature of this antenna is that its ports have independent frequency reconfiguration capacity through liquid metal. Then, a liquid metal controlled dual-band Doppler radar system using Vivaldi antennas designed with operating frequencies of 2.45 GHz and 5.8 GHz was developed. The proposed radar system is also integrated with a power divider for liquid-metal displacement, allowing seamless frequency switching between certain bands. A radar that can be controlled entirely by liquid displacement has been introduced to the literature with this method. The next goal of the thesis is to transform the liquid metal-controlled radar into a water-controlled form, which is a cost-effective and more accessible material. Therefore, an innovative mixture-based method for permittivity measurements is proposed. The proposed algorithm accelerates the determination of unknown material permittivity and reduces the computational dependence on 3D electromagnetic solvers. To achieve this goal, a cavity-based separated mode dual-band permittivity measurement system was established, and mode separation limits in conventional cavities were determined using Lagrange multipliers. Later, new cavity types that could exceed these limits were proposed, making the installation of the permittivity measurement mechanism easier. By combining separated mode cavities with an iterative measurement method that aims to find the permittivity of the unknown material by taking known mixtures as a reference, the permittivity and volume fraction of the water-based material were able to be determined, and Vivaldi antenna designs were updated to be controlled with water. This change allows liquid metal-based radar to be controlled with water, a more readily available and cost-effective material.

ÖZET

İLETKEN VE DİELEKTRİK SIVI MALZEMELER İLE AKIŞKAN OLARAK YENİDEN YAPILANDIRILABİLİR MİKRODALGA SİSTEMLERİ

Bu tezde, geleneksel elektriksel ve optik yeniden yapılandırma yöntemlerinin sınırlamalarının üstesinden gelmek amacıyla sıvı destekli mikrodalga bileşenlerinin kullanılmasına ilişkin detaylı bir araştırma sunulmuştur. Öncelikle, minyatürleştirmeye ve düşük hesaplama yüküne öncelik veren, 6.6 GHz ve 7 GHz'de çalışan yeni bir çift bağlantı noktalı anten önerilmiştir. Bu antenin en önemli özelliği, bağlantı noktalarının sıvı metal yoluyla bağımsız frekans yeniden yapılandırma kapasitesine sahip olmasıdır. Ardından, çalışma frekansları 2,45 GHz ve 5,8 GHz olarak tasarlanmış Vivaldi antenlerini kullanan sıvı metal kontrollü çift bantlı bir Doppler radar sistemi geliştirilmiştir. Önerilen radar sistemi aynı zamanda sıvı-metal yer değiştirmesi ile kontrol edilen bir güç bölücüyle de entegre edilerek belirli bantlar arasında kesintisiz frekans geçişine olanak tanımaktadır. Bu yöntem sayesinde literatüre tamamen sıvı yer değiştirmesi ile kontrol edilebilen bir radar kazandırılmıştır. Tezin bir sonraki amacı, sıvı metal kontrollü radarı, daha ucuz ve kolay erişilebilir bir malzeme olan su kontrollü bir forma dönüştürmektir. Bunun için geçirgenlik ölçümlerine başvurulmuş ve karışım bazlı yeni bir yöntem önerilmiştir. Önerilen algoritma, bilinmeyen malzeme geçirgenliğinin belirlenmesini hızlandırmakta ve 3 boyutlu elektromanyetik çözücülere olan hesaplama bağımlılığını azaltmaktadır. Bu amaca ulaşmak için kavite bazlı ayrık modlu çift bantlı geçirgenlik ölçüm sistemi kurulmuş ve geleneksel kavitelerdeki mod ayırma sınırları Lagrange çarpanları kullanılarak belirlenmiştir. Daha sonra bu sınırları aşabilecek yeni kavite tipleri önerilerek geçirgenlik ölçüm düzeneğinin kurulması daha kolay hale getirilmiştir. Ayrık modlu kaviteler, bilinen karışımları referans alarak bilinmeyen malzemenin geçirgenliğini bulmayı amaçlayan yinelemeli ölçüm yöntemiyle birleştirilerek su bazlı malzemenin geçirgenliği ve hacimsel fraksiyonu belirlenebilmiş ve Vivaldi anten tasarımları su ile kontrol edilebilecek şekilde güncellenmiştir. Bu değişiklik, sıvı metal bazlı radarın daha kolay bulunabilen ve uygun maliyetli bir malzeme olan suyla kontrol edilmesini sağlamıştır.

TABLE OF CONTENTS

LIST OF FIGURES

Figure	Page

Figure	Page

Figure **Page**

Figure	**Page**

LIST OF TABLES

LIST OF ABBREVIATIONS

CCDR .... Coffee-Can Doppler Radar
CST .... Computer Simulation Technology
DB .... Dual-Band
DGS .... Defected Ground Structure
DP .... Dual-Port
FBR .... Front-to-back ratio
FD .... Finite Difference
FDTD .... Finite Difference Time Domain
FEM .... Finite Element Method
FR-4 .... Flame Retardant-4
LM .... Liquid Metal
MEMS .... Microelectromechonical systems
MUT .... Material Under Test
MWS .... Microwave Studio
PD .... Power Divider
PIN .... Positive-Intrinsic-Negative
QW .... Quarter Wave
RF .... Radio Frequency
RMSE .... Root Mean Square Error
Rx .... Receiver
SB .... Single-Band
SIW .... Substrate Integrated Waveguide
TE .... Transverse Electric
TL .... Transmission Line
TM .... Transverse Magnetic
Tx .... Transmitter
VNA .... Vector Network Analyzer

CHAPTER 1

INTRODUCTION

Marked efforts have been spent improving the performance of reconfigurable microwave devices and responding to various demands in communications and radar systems. As for specific formations of the technical subsystems, the reconfigurability of the microwave devices should offer new avenues for enhancing functionality in filters, power dividers (PDs), frequency selective surfaces, tuners, absorbers, and a whole host of other structures within radio-frequency (RF) and microwave engineering. These traditional frameworks often carry inherent limitations that affect their adaptability as well as overall efficiency. This study would attempt to deviate from traditional methodologies in search of innovative strategies that tackle the limitations and heighten the adaptability of these electronic systems to modern-day uses.

1.1. Literature Search and Motivation of the Thesis

The synthesis of reconfigurable antenna and microwave device technology is summarized in the comprehensive review article (Christodoulou et al., 2012). This review does not cover liquid-based or liquid-assisted microwave device technology; instead, it focuses primarily on the discussion of material changes, with a particular focus on ferrites and crystal structures. The inclusion of liquid-assisted or liquid-based reconfigurable antenna and microwave devices in review articles is a relatively new phenomenon despite the historical use of such technologies prior to the 2012 publication. Figure 1.1, derived from a concurrent review article (Motovilova and Huang, 2020), describes the mechanisms for achieving the adaptive properties of reconfigurable antennas and other microwave devices. Expressing the increasing interest in liquid components in recent years, this review examines the fluidity and controllability properties of liquid materials within the scope of reconfiguration methodologies. Methods for changing the electromagnetic properties of microwave elements can be classified under four main groups: electrical, optical, physical, and material-based methodologies.

The three main groups of available methods for electrical reconfiguration of microwave components can be classified as RF-microelectromechanical system (MEMS), Positive-Instrinsic-Negative (PIN)-Diode, and varactor diodes (Khan et al.,2019). These methods, having high switching speeds, suffer from the degradation of antenna patterns upon integration. Besides, the achievable radiation efficiency through electrical techniques is limited because of the discrete characteristics of PIN diodes (Nikam et al., 2022). Also, RF-MEMS and varactor implementations may incur elevated power consumption due to the need for demanding bias voltage. On the other hand, the optical reconfiguration technique focuses on photoconductive material activation through a laser diode, diverging from electronic methods while preserving the intrinsic properties of the microwave device (Chen, 2016). However, laser diodes are bulky, costly to integrate, and hard to implement physically due to their high investment costs. Meanwhile, those with physical reconfiguration do not need biasing circuits or laser gadgetry. This technique has its advantages, which are high power capability and low losses. The limitations of the approach include slower switching speeds, issues associated with seamless integration, and challenges related to adjusting specific components. The last method, material-based, includes the reconfiguration technique, which can be categorized under a generalized classification of materials. The incorporation of other materials like ferroelectrics and ferrites shifts the intrinsic property of the permittivity and permeability when applied in electric and magnetic fields, respectively (Pozar and Sanchez, 1988). Similarly, the modulation of material properties correlates with variations in the applied voltage in liquid crystals. Although these structures have energy-efficient characteristics, they cause practical challenges due to their restricted operation temperature limits and complicated bias network requirements (Petosa, 2012; Yaghmaee et al., 2013).

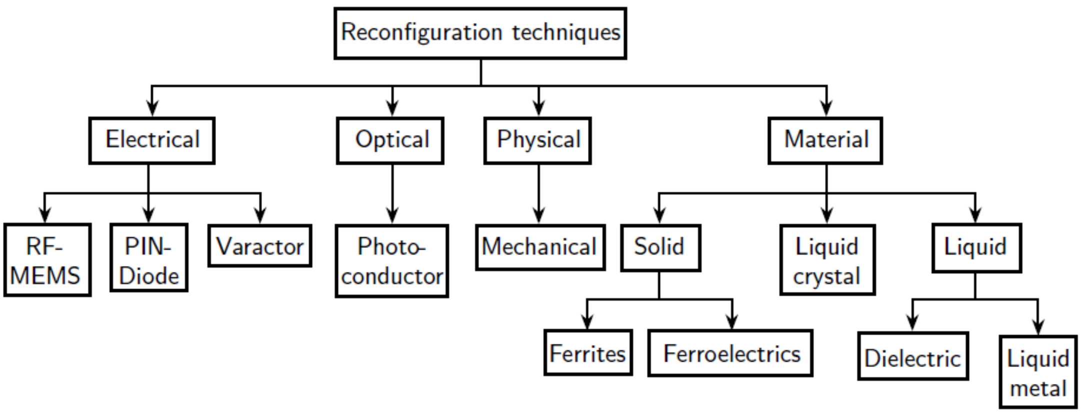

Figure 1.1. Reconfiguration techniques (Motovilova and Huang, 2020)

This thesis will pay particular attention to domains such as liquid-assisted microwave components, which currently evoke high interest from industrial and academic perspectives because of their unique characteristics. Features of this area, within this domain, including liquid metal (LM)-based or LM-assisted microwave devices, present inherent reconfigurability (Wu et al., 2023), possess high electrical conductivity and low loss to use in static antennas (Hayes et al., 2012; Bharambe et al., 2018), patterns (Ha et al., 2019; Hao et al., 2021), polarizations (Zhang et al., 2018; Lee et al., 2019), bandwidths (Alqurashi et al., 2020), frequency reconfigurable antennas (Li et al., 2021; Arbelaez et al., 2020), filters (McClung et al., 2018; Al-Yasir et al., 2019), metasurfaces (Sanusi et al., 2021), absorbers (Kim et al., 2016; Ling et al., 2015; Lei et al., 2021; Tian et al., 2021), power dividers (Wang et al., 2021), and switches (Sen and Kim, 2009; Vahabisani et al., 2017). Different from their electronically reconfigurable counterparts, their linearity is much higher. In microwave applications, LMs can be classified as being the main conductors (Khan et al., 2012; Guo et al., 2012), loading elements (Pourghorban Saghati et al., 2014; Murray and Franklin, 2014; Barrera and Huff, 2014), and short-circuit switches (King et al., 2013; Kelley et al., 2013).

Initially, we seek to complete an innovative and miniaturized antenna design, subsequently equipping it with frequency-reconfigurable capabilities through the utilization of LMs in Chapter 3. This study presents a novel fractal configuration for a dual-port (DP) antenna optimized for operation at both 6.6 and 7 GHz frequencies. The fundamental design strategy involves crafting an electrically compact and mirror-symmetric antenna, chosen strategically to alleviate the computational load for users requiring versatile frequency reconfiguration. This objective is systematically addressed through the application of a sophisticated 3D electromagnetic solver. Notably, the study emphasizes intentional simplicity in both simulation and fabrication aspects, abstaining from the integration of intricate structures such as a Substrate Integrated Waveguide (SIW) and additional phase-shifting circuitry, known to traditionally pose challenges in design and manufacturing processes. A distinctive feature of the proposed DP antenna is its intrinsic capability to independently tune the frequencies of its ports through novel modifications incorporating LM on the defected ground structure (DGS).

Once the reconfigurability of any feature of an antenna is demonstrated through the aid of LM, the following step involves multi-component or feature control, together with LM displacement, within a functional system. In the current body of literature, proof-of-concept is more focused, showing the practicalities and intricacies of different components rather than advancing the performance of functioning systems. In response to this research gap, we aim to come up with a concurrent design for different microwave components. In this thesis, our new step is the simultaneous design of the following microwave components:

1. Continuous wave operations of the MIT-Coffee-Can Doppler Radar (CCDR) were initiated with beam switching via LM in a single-band (SB) Vivaldi antenna working at 2.45 GHz. This antenna configuration is later converted into a dual-band (DB) Vivaldi antenna, transferring its operational frequency to 2.45 GHz and 5.8 GHz.

2. We introduce a novel PD capable of frequency switching between these two frequencies via LM displacement. This was integrated with the radar system, which provided a flexible radar that operated at different frequencies, thereby being adaptable in the face of interference threats.

These improved steps refine the CCDR equipped with continuous wave operations, as evidenced by pertinent studies (Carroll et al., 2016; Charvat et al., 2012; Karatay et al., 2019). Such configurations are widely used for short-range operations, first and foremost owing to cost-effectiveness and ease of deployment, hence making them the most viable option (Munoz-Ferreras et al., 2016; Pramudita and Suratman, 2021).

Table 1.1. Some popular LMs (Huang et al., 2021)

	Conductivity (MS/m)	Composition (%)	Melting (°C)
Hg	1	-	-39
EGaIn	3.4	Ga, In - 75, 25	16
Galinstan	3.3	Ga, In, Sn - 68.5, 21.5, 10	-19
$GaIn_{10}Ink$	3	Ga, In, O - $\sim$90, $\sim$10, 0.026	16
Ga	7.1	-	29

In this thesis, gallium is the chosen material for the application of LM, which is a non-toxic metal unlike Hg (Chen et al., 2007). However, materials possessing approximately equivalent conductivity values, such as EGaIn, Galinstan, or $GaIn_{10}Ink$, can serve the same purpose (Huang et al., 2021). To uphold the cost-effectiveness, we opt for pure gallium, which is a more economical, accessible, and non-toxic material upon contact. Despite its melting temperature of about 29 °C given in Table 1.1, this metal takes quite a long time to return to the solid state once adequately heated. Beyond the advantages given above, the LM-based components demonstrate enhanced operational durability due to their immunity to high temperatures and moisture, coupled with fewer maintenance requirements than that of the PIN diode configurations. In this context, the proposed approach has the potential to be applied in settings with limited resources, especially in situations where maintenance is challenging and there is a shortage of spare parts.

After finishing the radar with LM, a series of experiments are carried out to investigate the possibility of controlling the radar with more readily accessible liquids, including water-based dielectrics. A microwave cavity experimental setup is first proposed in order to easily measure the permittivity of water-based liquids at two different frequency bands. Note that, the microwave cavities are devices across a broad spectrum of contemporary measurement technologies and hold crucial roles in permittivity (Shi et al., 2022; Gutiérrez-Cano et al., 2019; Jha and Akhtar, 2014a; Krupka, 2006; Özkal and Yaman, 2023), permeability (Jha and Akhtar, 2014b; Gouveia et al., 2008), thickness determination (Li et al., 2022), and electron density measurement (Xiao et al., 2022). Microwave cavities are also widely used in many current-day technologies (Kharkovsky and Hasar, 2003; Forouzanfar and Joodaki, 2018; Jiang et al., 2021; Goryashko et al., 2018).

Another important contribution of the thesis is to make the measurement at the operating frequencies of the radar and to increase the measurement sensitivity by not exciting a different mode between these two frequencies. Researchers carry out research that excites a single mode while suppressing others. Single-mode excitations are prominently highlighted in numerous studies in the literature as applied across various domains, as reported by (Krupka (2006), Krupka (2006); Özkal and Yaman (2023), Özkal and Yaman (2023); Robinson et al. (2010), Robinson et al. (2010); Curet et al. (2008), Curet et al. (2008); Dutta et al. (2006), Dutta et al. (2006)). The objective has always been to adequately separate the frequencies of one mode from others, especially when spectral peaks related to different modes overlap. This separation between the first two modes at high frequencies has been made more advantageous since both frequency shifts and a decrease in quality factor occur during permittivity measurements. Consequently, in the frequency domain, there is a high probability that close modes will interfere. The demonstration of the analytical result from Lagrange multipliers shows a restriction of achieving the separation of the first two modes within rectangular and cylindrical cavities, manifesting low flexibilities of the placement for the first two modes at 2.45 and 5.8 GHz within the ISM bands. In these cavities, according to the analytical results, the second mode cannot be settled at 5.8 GHz, while the first mode settles at 2.45 GHz. To get around the issue, a novel miniaturized cavity is proposed for construction using 3D printing techniques, and an LM-assisted approach is applied for tuning frequency shifts caused by production errors. Since the quality factor of the 3D printed method is low for this measurement, a different separated mode cavity is proposed to be produced by the machining method, and the production of this cavity is completed with two different materials, aluminum and steel.

After separated mode cavity designs were accomplished, a new permittivity measurement algorithm based on the perturbation of DB cavities was studied. A novel approach of measuring complex permittivity in microwave frequency in simple cavity perturbation (Nohlert et al., 2020; Kim et al., 2020) offers numerous advantages, including simplicity, cost-effectiveness, non-destructiveness, rapidness, and versatility across diverse materials (Chang et al., 2012; Barter et al., 2018; Verma and Dube, 2005). Despite its high accuracy compared to other permittivity measurement methods and its suitability for small sample volumes (Sheen, 2009; La Gioia et al., 2018), difficulties arise when dealing with materials with high loss characteristics and its accuracy can be affected by the sample shape and size (Peng et al., 2013). Also, considering the design of various structures, the analytical approach is usually restricted to measuring permittivity at a single frequency (Kik, 2016; Sheen and Weng, 2016). Therefore, iterative techniques play a common role in obtaining precise permittivity measurements. The implementation of these methods can be done using dedicated commercial software tools, such as CST or HFSS (Santra and Limaye, 2005; Özkal and Yaman, 2023; Yu et al., 2021) or non-commercial numerical solvers (Thakur and Holmes, 2001). However, these tools generally require computationally expensive full mesh simulations at every iteration step, depending on factors such as electrical size, curvature, frequency range, and dielectric constant. For this reason, the present thesis introduces a novel permittivity measurement method by applying an iterative approach that eliminates the dependence on software tools. Instead of relying on highly complex simulations at each step, adjustments are made using the manipulation of the liquid volume fraction. This way, one can achieve precision without time-consuming simulations. Besides, between the first two resonant frequencies, switching the frequencies of the probe is achieved through the manipulation of LM.

The last step involves converting the Doppler radar to a water-based structure with the aim of making LM-controlled antennas controllable with a water-based mixture through modifications, especially with saline water. Since water is much more accessible, cost-effective, and has lower viscosity compared to gallium, this approach emerges as a significant improvement. Particularly, it holds the potential to be of importance for marine applications. Liquid dielectric microwave components have witnessed an increasing demand (Entesari and Saghati, 2016), and they are used in the designing of absorbers

(Zhang et al., 2020; Zou et al., 2022; Kwon et al., 2021), metamaterial components (Wang et al., 2020; Zhang et al., 2020; Stenishchev and Basharin, 2017), power dividers (Patel et al., 2023), and various antennas such as monopoles (Xing et al., 2015; Zou and Pan, 2015; Song et al., 2019; Zhou et al., 2016; Hua and Shen, 2015), patches (Sun and Luk, 2020a; Li and Luk, 2015; Sun and Luk, 2020b), horns (Ren et al., 2021), reflectors (Liang et al., 2018), dielectric resonators (Wang and Chu, 2019), and helical antennas (Ren et al., 2019). Further, literature encompasses different planar antennas utilizing microfluidic channels or cavities (Singh et al., 2019; Tang and Chen, 2017; Qian and Chu, 2017; Wang et al., 2017; Jobs et al., 2013; Hage-Ali et al., 2010); most research in this area also includes applications using water-based structures that can be seen through the optical transparency of water (Sun and Luk, 2017; Sayem et al., 2020; Sun and Luk, 2021). Dielectric liquids have gained prominence for several reasons. Their fluidity and reshapeability allow the realization of diverse structural shapes. The ease with which the physical and chemical properties of dielectric liquids can be manipulated facilitates the reconfiguration of electromagnetic properties in microwave components (Xing et al., 2019). The reason, in a word, is efficiency: it enables the cost-effective realization of a microwave device, especially by using materials that are essentially free, like water. As compared to other dielectric-based materials, microwave devices fabricated from water-based materials can show transparency, making them potential applications for solar panels. Moreover, these components are environmentally friendly and biocompatible. The controllable permittivity using various mixtures, coupled with high permittivity, enables effective miniaturization.

Contemporary studies of liquid-based microwave device studies are primarily associated with antenna technology (Hua et al., 2021; Xing et al., 2015; Abu Bakar et al., 2021). In the comparison of liquid-based, water-based, non-water-based, and conventional antennas, four key categories, efficiency, reconfigurability, fabrication, and safety, provide the underlying factors that are being assessed. High antenna efficiencies are common to all structures (Bennett et al., 2019). However, with increasing frequency in water-based antennas, the efficiency may be affected by the rising loss tangent (Bennett et al., 2019). On the other hand, literature reports instances of high antenna efficiency in water-based antennas (Hua et al., 2014). Concerning reconfigurability, liquid antennas may offer more opportunities than conventional ones. They would be able to use liquid pumps and gravitational methods other than traditional electrical methods. Reconfigurability in liquid antennas includes the versatility of adjusting electromagnetic properties of materials through chemical and thermal processes, thus being more flexible than in conventional antennas. On the other hand, the limitations of liquid antenna fabrication are higher compared to conventional counterparts. The holder requirement is one of them, and there could be a need for the microfluidic channel design. Tight insulation is critical to prevent leaks. In this stage, LM may be advantageous due to the potential solidification at operating temperatures; hence, holders may not always be required. Also, safety is a very critical parameter involving potential harm to human health and the environment. Conventional and water-based antennas are nearly risk-free when considering the likely hazards. LM and non-water-based antennas may introduce certain hazards from the used materials. On the other hand, toxic substances like mercury might pose health risks, and at certain stages of the fabrication process, flammable substances, such as transformer oil, could pose a fire risk.

Despite the drawbacks mentioned above, there is considerable superiority in liquid microwave structures, gaining intensity from their inherent reconfigurability. Not only this, but a layer of economic viability is also provided to the structures through the distinctive properties of liquids, being fluidic in nature and adaptable easily. Furthermore, highly dielectric media, such as water, play a pivotal role in diminishing size and bestowing some distinctive features, such as transparency, an attribute seldom seen in traditional microwave devices. Also, the purely mechanical nature of these materials makes these structures provide less interference on those electrical counterparts, along with fewer maintenance costs and fewer spare parts. Despite these advantages, there are some challenges that need to be solved, and further optimization of their performance remains to be improved. For this thesis, the contribution lies in substantiating the operational functionality of liquid-based microwave components, which was presented in the literature merely as a proof-of-concept. We establish the viability of these components operating within a radar system and demonstrate their controllability with liquid. This thesis commences with the implementation step, wherein gallium is applied to prove independent reconfiguration of ports in self-diplexing antennas, normally used in communication systems. Later, the design of Vivaldi antennas and their corresponding PD was done, showing for the first time in the literature the potential of actively controlling a Doppler radar through liquid-based reconfiguration. Extending the scope of work beyond LM utilization, this research explores the utility of dielectric liquids in governing an operational radar system. To fill this gap, a DB dielectric permittivity measurement method was proposed. Unlike conventional cavities, these measurements have been done with the separated mode cavity that boosts measurement precision. The iterative approach was run on the measurements using the separated mode cavity not only to improve accuracy but also to introduce a highly advantageous permittivity measurement system to the existing literature. After the development of the algorithm and test measurements, the saline water-controlled radar system was reconstructed. Different modifications were made to the antennas, wherein the reconfiguration method was switched from gallium-based to saline water. Consequently, the associated radar system became easily accessible and less costly and could be reconfigured in an automated manner. All these studies derived from this thesis were published in various journals (Karatay, 2022; Karatay and Yaman, 2024a; Karatay and Yaman, 2024b; Karatay and Yaman, 2024c).

1.2. Organization of the Thesis

The organization of the thesis is structured as follows. Chapter 2 stands towards a thorough description of the background information related to the thesis. Chapter 3 provides a novel self-diplexing microstrip antenna, presented with results for the described network. According to the research results, the proposed antenna brings the following advantages over the existing ones in terms of computational and manufacturing benefits. Furthermore, a DP antenna enables independent control of both ports while keeping the number of modifications required at a minimum. Changes can be performed using two fluid channels and minimal amounts of gallium. Chapter 4 is dedicated to presenting the design and fabrication processes of a Doppler radar controlled by LM. The study uses an MIT-CCDR-based Doppler radar with a PD, transmitter and receiver antenna that are highly robust due to main lobe control through LM. It is achieved with robustness compared to conventional electrical reconfiguration techniques for the simultaneous working of two separate bands at 2.45 GHz and 5.8 GHz. Chapter 5 and 6 introduce the DB dielectric permittivity method through separated mode cavities for reconfiguring a radar operating at 2.45 GHz and 5.8 GHz, replacing LM with a dielectric liquid-based approach. Chapter 5 details the design of a cavity with modes at these frequencies, overcoming analytical challenges to successfully position the first two modes at 2.45 GHz and 5.8 GHz for enhanced measurement performance. Chapter 6 presents an iterative approach toward an efficient way to determine the dielectric permittivity of unknown materials with the help of a mixture-based process, resulting in a rapid and more uncomplicated measurement process compared to the time-consuming iterative simulations. Chapter 7 summarizes design parameters and measurement results demonstrating control of the Doppler radar with saline water. Concluding remarks and future directions are presented in Chapter 8.

CHAPTER 2

BACKGROUND

In this chapter, we provide the mathematical background information related to the methods to be employed in the thesis. Basic information on fundamental properties of matters, antenna parameters and fabrication methods, fundamental cavity parameters, and cavity perturbation methods used in the thesis study are presented here. In addition, the fundamentals of numerical and analytical methods used throughout the thesis are also summarized in this chapter.

2.1. Fundamental Electrical Properties

Electrical properties of matter stand for understanding and governing the behavior of matter. Some of these parameters are permittivity (ε), permeability (μ), and conductivity (σ). Permittivity (ε) is the measure of the ability of electric field lines to flow through a medium. It is as significant as defining the behavior of capacitors and dielectric materials. Permittivity is usually divided into two factors: ε_0, the vacuum permittivity, and ε_r, the relative permittivity. Furthermore, permittivity is characterized by two separate components, real and imaginary.

$$\varepsilon = \varepsilon^{'} - j\varepsilon^{''} \tag{2.1}$$

$$\varepsilon = \varepsilon_r \varepsilon_0 \tag{2.2}$$

It can be related to the polarization vector $\vec{P}$ as follows.

$$\vec{D} = \varepsilon_0 \vec{E}_a + \vec{P} \tag{2.3}$$

where $\vec{E}_a$ denotes the applied electric field, $\vec{D}$ is the electric flux density vector. μ is analogous to permittivity but relates to a material's response to magnetic fields rather than electric fields. Similar to permittivity, permeability can be separated into vacuum permeability, μ_0, and relative permeability, μ_r. The relationship between the vacuum permeability, relative permeability, and permeability is given by:

$$\mu = \mu_r \mu_0 \tag{2.4}$$

Also, conductivity σ with a unit of Siemens/m (S/m) measures a material's ability to conduct electric current. It is the multiplicative inverse of resistivity ($\sigma = 1/\rho$) and is a critical parameter in determining the efficiency of electrical conduction within a material. The equation below indicates that introducing an electric field into a material will generate electrical currents, and their magnitude and direction will be directly proportional to the intensity of the electric field.

$$\vec{J} = (\sigma + j\omega\varepsilon)\vec{E} \tag{2.5}$$

where ω denotes the angular frequency and ε has both real and imaginary components. The effective conductivity to calculate the material losses can be defined as:

$$\sigma_{eff} = \sigma + \omega\varepsilon^{''} \tag{2.6}$$

2.2. Antennas

Antennas are essential components in communication and radar systems and other electromagnetic networks. They are designed to transmit or receive electromagnetic waves (Balanis, 2016). These devices convert electrical signals into electromagnetic waves for transmission or convert electromagnetic waves into electrical signals for reception. Some fundamental parameters, which are beamwidth, gain, and directivity of antennas, need to be considered at close quarters for optimization of coverage and resolution. In this section, the fundamental parameters of antennas and methods applicable to their fabrication are provided.

2.2.1. Antenna Parameters

In order to evaluate the performance of an antenna, it is essential to establish definitions for various parameters. This subsection provides the definitions of these parameters, e.g., radiation power density, radiation power intensity, directivity, gain, and realized gain. Beyond these, emphasis is placed on concepts such as beamwidth and bandwidth. Additionally, within this subsection, the advantages and disadvantages of gain measurement methods are also discussed.

The radiated power density in terms of the electric field vector and the magnetic field vector is given by the Poynting vector as:

$$\vec{W}_{\text{rad}} = \frac{1}{2}\,\mathrm{Re}\left(\vec{E} \times \vec{H}^{*}\right) \tag{2.7}$$

where $\vec{E}$ is the electric field vector, $\vec{H}$ is the magnetic field vector, and $\times$ denotes the vector cross product. The asterisk (*) represents the complex conjugate. The average radiated power can be written as follows.

$$P_{\text{rad}} = \oint_{S} \vec{W}_{\text{rad}} \cdot \mathrm{d}\vec{s} \tag{2.8}$$

The radiation intensity is related to the radiated power density and the distance from the source.

$$U = r^{2} W_{\text{rad}} \tag{2.9}$$

where $\vec{W}_{\text{rad}} = \hat{r} W_{\text{rad}}$. This equation represents the relationship between radiation intensity, radiated power density, and distance for isotropic radiation.

The term directivity points out an antenna's ability to focus its radiated power into a particular direction, as rated in terms of the ratio of the radiation intensity observed in that particular direction to the average radiation intensity across all directions. The average radiation intensity is obtained by dividing the total power radiated by an antenna by 4π. In those cases where a particular direction is not explicitly specified, it is generally understood to point to the direction of maximum radiation intensity. A nonisotropic source directivity can simply be defined as the proportion of its radiation intensity in an arbitrarily chosen direction relative to an isotropic source.

$$D = \frac{4\pi U}{P_{\text{rad}}} \tag{2.10}$$

If we are referring to the angle at which the antenna achieves maximum directivity, in this case, it is necessary to consider the angle at which it possesses maximum radiation intensity in calculations.

$$D_{\text{max}} = \frac{4\pi U_{\text{max}}}{P_{\text{rad}}} \tag{2.11}$$

Gain serves as a metric that factors in both the antenna's efficiency and its directional capabilities. It is important to note that directivity solely characterizes the antenna's directional features and is consequently influenced solely by its pattern. Gain is given as:

$$G = e_c e_d D \tag{2.12}$$

where e_c and e_d denote the conduction and dielectric efficiencies, respectively. The gain value that takes into account the reflection coefficient, along with considerations for the total efficiency of the antenna, is referred to as realized gain or absolute gain. The mathematical expression for this parameter is given as follows:

$$G_{\text{realized}} = e_c e_d e_r D \tag{2.13}$$

Here, e_r is given as the reflection efficiency. At this point, it is assumed that there is no polarization mismatch between the transmitter and receiver. If there is a mismatch in polarization as well, it would be appropriate to incorporate it into the calculations as a separate factor.

Various methods have been developed to measure this parameter. Measurements, often conducted in an anechoic chamber, can generally be categorized into two main headings: absolute gain measurements and gain transfer measurements. The absolute gain method encompasses numerous methods, including the two-antenna method, the three-antenna method, the extrapolation gain measurement method, and the ground reflection method. For instance, in the case of using two identical antennas in the absolute gain method with a distance of r, the gain can be roughly calculated by leveraging the Friis transmission equation.

$$G\left(\mathrm{dB}\right) = \frac{1}{2}\left(P_{\mathrm{r}}\left(\mathrm{dB}\right) - P_{\mathrm{t}}\left(\mathrm{dB}\right) + L_r\right) \tag{2.14}$$

$$L_r = 20\log_{10}\left(\frac{4\pi r}{\lambda}\right) \tag{2.15}$$

where λ denotes operating wavelength, P_{t} and P_{r} are the transmitted and received power, respectively. If the antennas are not identical, a system of three equations can be formed using three antennas. By doing so, a set of three unknowns and three equations can be obtained, allowing for the determination of the gains of the three antennas.

$$G_1\left(\mathrm{dB}\right) + G_2\left(\mathrm{dB}\right) = P_{\mathrm{r2}}\left(\mathrm{dB}\right) - P_{\mathrm{t1}}\left(\mathrm{dB}\right) + L_r \tag{2.16}$$

$$G_1\left(\mathrm{dB}\right) + G_3\left(\mathrm{dB}\right) = P_{\mathrm{r3}}\left(\mathrm{dB}\right) - P_{\mathrm{t1}}\left(\mathrm{dB}\right) + L_r \tag{2.17}$$

$$G_2\left(\mathrm{dB}\right) + G_3\left(\mathrm{dB}\right) = P_{\mathrm{r3}}\left(\mathrm{dB}\right) - P_{\mathrm{t2}}\left(\mathrm{dB}\right) + L_r \tag{2.18}$$

where numerical subscripts denote the antenna numbers. In all these measurements, attention should be given to ensuring that the impedances, polarizations, and maximum gain angles of the antennas match, and that the measurements are conducted in the far-field region. Nonetheless, none of the methods above provides a definitive solution for cable and connector losses. Therefore, the gain transfer method is often preferred. By initially conducting relative gain measurements and subsequently comparing them with the known gain of a standard antenna, this method utilizing a gain standard with a known gain allows for the determination of absolute gains.

$$G_{\mathrm{AUT}}\left(\mathrm{dB}\right) = G_{\mathrm{STD}}\left(\mathrm{dB}\right) + P_{\mathrm{AUT}}\left(\mathrm{dB}\right) - P_{\mathrm{STD}}\left(\mathrm{dB}\right) \tag{2.19}$$

where subscripts AUT and STD denote antenna under test and standart gain antenna, respectively. The method involves conducting relative gain measurements, where the gain of the antenna under test is compared to that of the standard gain antenna.

Bandwidth, another important parameter, refers to the range of frequencies over which the antenna can effectively transmit or receive signals. In general, bandwidth may refer to the frequency range between the upper and lower limits of the operating spectrum at which the specified criteria of performance of the antenna are met. Frequently used definitions of bandwidth include the frequency at which the S_{11} stays below a specified value, typically considered as -6 or -10 dB. Terms like gain bandwidth or polarization bandwidth, especially in the case of antennas where polarization behavior is intended, are often used. The implication here is whether the antenna works at the gain value or polarization across the frequency range designed.

Besides, beamwidth usually refers to the 3-dB beamwidth or half-power beamwidth, a crucial parameter that describes the angular span of an antenna's main lobe where the power is at least half of its maximum. This is considered an important metric, usually referred to as a tradeoff against the sidelobe level. As the beamwidth decreases, sidelobe levels tend to rise and vice versa. In addition to this, the beamwidth is very important in characterizing an antenna's resolution capabilities and defining its ability to distinguish between adjacent radiating sources or radar targets.

Another parameter used when characterizing an antenna is polarization. In a particular direction, the polarization is the direction of the electric field of the wave transmitted or radiated by the antenna, with the default being the polarization in the direction of maximum gain. By virtue of operating on different parts of the antenna pattern, the polarization in the radiated energy changes with the frequency, with parts of the pattern being described with differing polarizations. Polarization is defined by the time-varying direction and relative magnitude of the electric-field vector traced in space over time along the direction of propagation.

Consider the x and y components of the electric field of an electromagnetic wave propagating in the -z direction, given by:

$$\vec{E} = E_x\hat{x} + E_y\hat{y} \tag{2.20}$$

$$E_x = E_{0x}e^{j(\omega t + kz + \phi_x)} \tag{2.21}$$

$$E_y = E_{0y}e^{j(\omega t + kz + \phi_y)} \tag{2.22}$$

where E_{0x} and E_{0y} denote the amplitudes of the x- and y-components of the electric field, respectively; ω is the angular frequency of the wave; k is the wavenumber; z is the direction of propagation; and ϕ_x and ϕ_y are the initial phase offsets of the x- and y-components. For linear polarization, either one of the two orthogonal components must be zero, or the following condition should be satisfied.

$$\phi_y - \phi_x = n\pi \text{ where } n = 0, 1, 2, ... \tag{2.23}$$

For circular polarization, the magnitudes of the two orthogonal components should be equal, and the following condition must be satisfied.

$$\phi_y - \phi_x = \pm\left(\frac{\pi}{2} + 2n\pi\right),\ n = 0, 1, 2, ... \tag{2.24}$$

In the scenario where the magnitudes are equal, and the phase difference is odd multiples of 90 degrees, circular polarization can be identified. If the sign at the beginning of the parenthesis is plus, it denotes a clockwise direction, whereas if it is minus, it indicates a counterclockwise direction. However, had the propagation direction been +z instead of -z, the situation would be reversed.

Elliptic polarization is attained if the electromagnetic field has two orthogonal linear components. In a scenario where the magnitudes are not equal, it is essential to ensure that the phase difference is neither zero nor an integer multiple of π, as this would result in linear polarization. On the other hand, when the magnitudes are equal, it is paramount not to allow a time-phase difference between the components to be an odd multiple of $\pi/2$ in order to avoid circular polarization. At a particular position in time, the trajectory traced usually presents as a titled ellipse. The axial ratio is defined as the ratio of the major axis to the minor axis. Here, the major axis refers to the longest dimension of the polarization ellipse, representing the maximum electric field amplitude, while the minor axis is the shortest dimension, corresponding to the minimum electric field amplitude. It is calculated as follows.

$$AR = \frac{\text{Major axis}}{\text{Minor axis}}, \quad 1 \leq AR \leq \infty \tag{2.25}$$

The last parameter to be given in this subsection is the radar cross-section (RCS) (σ_{rcs}), and it describes the measure of the ability of a target to reflect signals in the radar system. It represents the scattering or reflecting properties of an object whenever illuminated with electromagnetic waves. It is dependent on size, shape, orientation, and material composition. In mathematical terms, it can be defined as the effective area that receives the incident radar power density and is most often represented in m^2. It is possible to represent the effective area that intercepts the incident radar power density by stating the relationship of the transmitted power, received power, and the range to the target in radar systems by the radar range equation, which can be written mathematically as:

$$P_r = P_t \frac{G_1 G_2 \lambda^2 \sigma_{rcs}}{(4\pi)^3 r^4} \tag{2.26}$$

2.2.2. Antenna Fabrication Techniques

In this subsection, the fabrication methods of various antennas produced within the thesis are detailed. The details of the production are provided, starting with the use of a copper-clad Flame Retardant-4 (FR-4) material with a photoresist coating on its outermost layer. Subsequently, the production process using an FR-4 material without any coating is elaborated through aerosol coating.

2.2.2.1. Chemical Etching Method

We will elaborate on the details of the photo corrosion-based chemical etching method below, and aspects of the production that need to be considered are detailed here. This entails 16×10 cm^2 Bungard FR-4 plates with a coating on both copper surfaces. Initially, on both sides of the copper-coated surfaces, there is a photoresist coating, as represented in Figure 2.1-(a). After masking, applied UV light to the photosensitive layer increases its solubility, as represented in Figure 2.1-(b). The exposure times can be 6 minutes or higher. Immersion of the plate in an aqueous NaOH solution is depicted in Figure 2.1-(c) and (d) and carries out the process of dissolving the exposed portions of the photoresist layer. A solution containing 5 g NaOH in 1 liter of water at 40 °C can be used to do that.

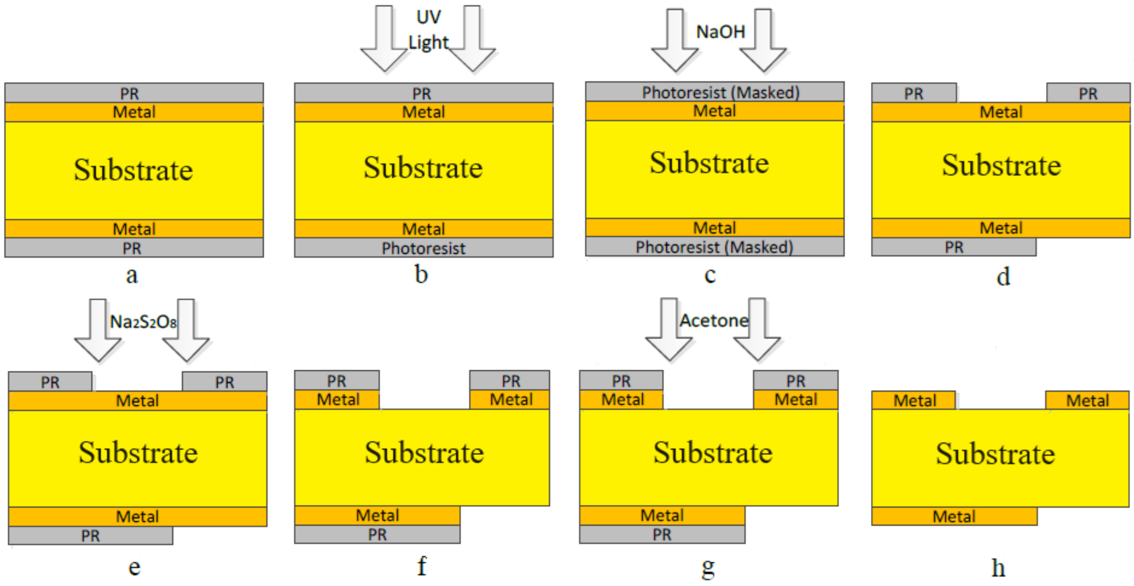

Figure 2.1. Chemical etching technique (Bozdag, 2014)

The remaining photoresist layer shields the copper from the sodium persulfate solution, causing only the exposed copper to dissolve, as seen in Figure 2.1-(e) and (f). Using water at 100 °C and adding approximately 350 g of sodium persulfate to 1 liter of water completes the copper etching process. After the copper is etched, acetone is applied to the remains of the photoresist layer that has not been etched by the process as mentioned above, as depicted in Figure 2.1-(h) and (i). Next, the unused section of the large FR-4 plate has to be cut from the antenna boundaries with a laboratory metal cutter.

(a) (b)

Figure 2.2. Chemicals used (a) Natrium Hydroxide (NaOH) (b) Sodium Persulfate

The chemicals used in the fabrication process can be seen in Figure 2.2. Protective equipment such as face masks, protective glasses, and lab coats are a must in the production process, as NaOH solution causes permanent damage, especially to clothes, and sodium persulfate solution can cause skin irritation, and inhalation of its vapor can cause lung damage.

2.2.2.2. 3D Printed Masking

Using 3D printing technology as a fabrication technique minimizes the production costs. Due to the cost of photoresist and copper-coated FR-4 substrates, it served as a cost-effective alternative, whereby a substrate with copper-free substrate was coated with a conducting layer by the use of a 3D printer and a conductive spray. The complements of the antenna design are generated using a 3D printer, which helps in designing and manufacturing these components as masks for the substrate. Consequently, in Figure 2.3, the substrate is coated with conductive aerosol spray and replicates the shape. This process contributes to a reduction in production costs.

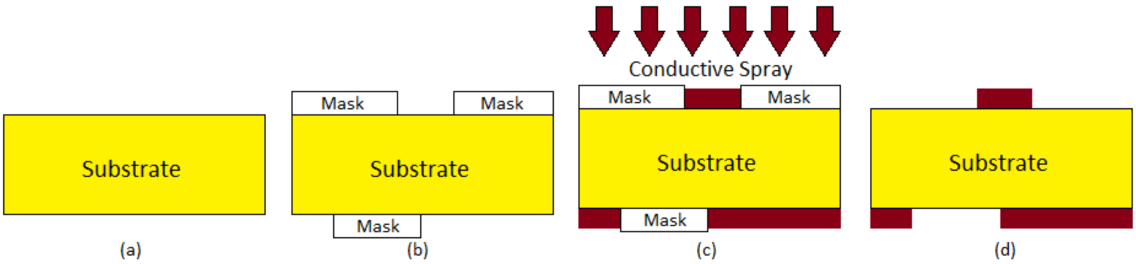

Figure 2.3. 3D printed masking-based fabrication (a) empty substrate (b) masking (c) coating (d) fabricated antenna (Karatay, 2022)

2.3. Cavities

Microwave cavities, which are designed to confine electromagnetic waves at specific frequencies, are commonly described in 3D configurations. These structures sustain the existence of two fundamental modes of propagation of electromagnetic waves: transverse electric (TE) and transverse magnetic (TM). These modes help to describe the distribution and polarization of the electric and magnetic fields in the cavity. For instance, electromagnetic waves propagating in TE modes have the electric field transverse to the propagation direction, with no electric field component along the propagation direction. On the other hand, in TM modes, the magnetic field is transverse to the direction of propagation (Pozar, 2011).

2.3.1. Cavity Parameters

Various parameters are employed to characterize a microwave cavity and its relationship with a coupler. This subsection delves into the mathematical background of these parameters. It is imperative to align the resonant frequency of a particular mode to the oscillation frequency of the power supply to facilitate efficient power transfer into the cavity. The resonant frequency for a cylindrical cavity is given by:

$$f_{nmp} = \frac{c}{2\pi\sqrt{\varepsilon_r \mu_r}} \sqrt{\left(\frac{\chi_{nm}}{r}\right)^2 + \left(\frac{p\pi}{l}\right)^2} \tag{2.27}$$

where r and l denote the radius and height of the cylindrical cavity, respectively. It is noteworthy that χ_{mn} represents the roots of Bessel functions for TM modes and the roots of the derivative of Bessel functions for TE modes. Expanding our understanding, the resonant frequency in a parallel RLC equivalent circuit is:

$$f = \frac{1}{2\pi\sqrt{L_{par} C_{par}}} \tag{2.28}$$

where L_{par} and C_{par} denote the inductance and capacitance of the parallel equivalent circuit, respectively. Additionally, for the dominant mode of a rectangular cavity, the resonant frequency can be expressed as:

$$f_{mnp} = \frac{c}{2\pi\sqrt{\varepsilon_r \mu_r}} \sqrt{\left(\frac{m\pi}{a}\right)^2 + \left(\frac{n\pi}{b}\right)^2 + \left(\frac{p\pi}{d}\right)^2} \tag{2.29}$$

where a, b, and d represent the dimensions of the rectangular cavity, while m, n, and p are the mode indices.

The quality factor is another critical parameter governing the power-handling capacity of a cavity and is directly proportional to the square root of the cavity wall conductivity. It is also influenced by the cavity's geometry. It is given with:

$$Q = \frac{\omega\mu \int_V |\vec{H}|^2 dv}{R_s \oint_S |\vec{H}_{||}|^2 ds} \tag{2.30}$$

$$R_s = \sqrt{\frac{\pi f \mu}{\sigma}} \tag{2.31}$$

where σ signifies the bulk conductivity of the material. Expressing the quality factor in terms of an equivalent parallel RLC circuit, it is characterized by:

$$Q = 2\pi f R_{par} C_{par} \tag{2.32}$$

where R_{par} represents the resistance of the parallel equivalent circuit of the corresponding mode. The loaded quality factor is determined as the ratio of the resonant frequency to the bandwidth, given by:

$$Q_{\mathrm{L}} = \frac{f_0}{\Delta f} \tag{2.33}$$

Here, $\Delta f = f_{-3dB}^{\text{high}} - f_{-3dB}^{\text{low}}$.

For the definition of a material-independent quality factor, a parameter named the geometry factor has been introduced, obtained through the normalization of the surface impedance given in Equation 2.34. In essence, the geometry factor only hinges on the geometry of the structure and remains consistent irrespective of the material composition. This implies that two cavities possessing the same shape but constructed from different materials exhibit identical geometry factors, even though their quality factors may differ.

$$G = R_s Q \tag{2.34}$$

Directly measuring the quality factor of a cavity is practically unattainable since the cavity is inevitably coupled to the circuitry of measurement instruments or other external circuits. In such instances, the measured quality factor represents the total Q value of the entire system. Extracting the cavity's inherent Q from the measured value requires knowledge of the external circuit in which cavity is coupled. One can model a resonant cavity, a series RLC circuit connected to a transmission line (TL) with a Z_0 characteristic impedance value. Q_0 and Q_{ext} of the corresponding mode can be expressed as:

$$Q_0 = \frac{\omega_0 R_{ser}}{L_{ser}} \tag{2.35}$$

$$Q_{ext} = \frac{\omega_0 Z_0}{L_{ser}} \tag{2.36}$$

where R_{ser} and L_{ser} denote the resistance and inductance of the series equivalent circuit, respectively. When Z_0 and the series resistance are equal to each other, Q_0 and Q_{ext} are also equal, indicating critical coupling. The final form of the expression is given by Equations 2.37 and 2.38. When the coupling factor, β, is around unity, the mode is in a critically coupled state, exhibiting a low reflection coefficient. Conversely, values of β approaching zero or infinity signify under-coupling or over-coupling, respectively, leading to a reflection coefficient amplitude close to unity.

$$\frac{1}{Q_L} = \frac{1}{Q_0} + \frac{1}{Q_{ext}} = \frac{1+\beta}{Q_0} \tag{2.37}$$

$$\beta = \frac{Q_0}{Q_{ext}} = \frac{S_{21}}{1 - S_{21}} \tag{2.38}$$

Here, Q_L is the measured value given in Equation 2.33. In cases where the coupling is sufficiently weak, Q_{ext} goes to infinity, and Q_L is equal to Q_0.

2.3.2. Cavity Perturbation

In real-world scenarios, cavity resonators are frequently altered through minor adjustments to their geometry or by introducing small components made of metallic or dielectric materials. For instance, the resonant frequency of a cavity resonator can be conveniently adjusted using a small screw inserted into the cavity volume. Another application involves assessing the dielectric constant by observing the shift in resonant frequency when a small dielectric sample is introduced into the cavity (Hill, 2009).

2.3.2.1. Metallic Perturbation

The shape perturbation technique is a tailored method designed for cavities and waveguides, offering an analytical approach to determining the effects of minor alterations in simple structures. Consider a resonant cavity mode with known electric and magnetic field distributions, $\vec{E}_0$ and $\vec{H}_0$, perturbed by a small defect on the conductor wall. The primary goal is to ascertain the frequency shift of the perturbed cavity mode using the field information from the unperturbed one. Ampère's and Faraday's equations are provided below for both cavities, with the assumption that the region is source-free.

$$\nabla \times \vec{E}_0 = -j\omega_0\mu\vec{H}_0 \tag{2.39}$$

$$\nabla \times \vec{H}_0 = j\omega_0\varepsilon\vec{E}_0 \tag{2.40}$$

$$\nabla \times \vec{E}_1 = -j\omega_1\mu\vec{H}_1 \tag{2.41}$$

$$\nabla \times \vec{H}_1 = j\omega_1\varepsilon\vec{E}_1 \tag{2.42}$$

Complex conjugates of Equation 2.39 are multiplied by $\vec{H}_1$, magnetic field of the perturbed cavity mode, and Equation 2.42 is multiplied by $\vec{E}_0^*$. Note that, $\vec{H}_1$ is defined as the electric field of the perturbed cavity mode. Subtraction of these equations results in Equations 2.43 and 2.44.

$$\nabla \cdot (\vec{E}_0^* \times \vec{H}_1) = j\omega_0\mu\vec{H}_1 \cdot \vec{H}_0^* - j\omega_1\varepsilon\vec{E}_1 \cdot \vec{E}_0^* \tag{2.43}$$

$$\nabla \cdot (\vec{E}_1 \times \vec{H}_0^*) = -j\omega_1\mu\vec{H}_1 \cdot \vec{H}_0^* + j\omega_0\varepsilon\vec{E}_1 \cdot \vec{E}_0^* \tag{2.44}$$

Subsequently, Equations 2.43 and 2.44 are combined, and a volume integral over the perturbed cavity volume, V_1, is calculated. Applying the divergence theorem transforms the volume integral into a surface integral, leading to Equation 2.45. Note that the tangential component of $\vec{E}_1$ is zero on the surface of the perturbed cavity.

$$\int_{V_1} \nabla \cdot (\vec{E}_0^* \times \vec{H}_1)\mathrm{d}v + \int_{V_1} \nabla \cdot (\vec{E}_1 \times \vec{H}_0^*)\mathrm{d}v = \oint_{S_1} (\vec{E}_0^* \times \vec{H}_1) \cdot \mathrm{d}\vec{s} + 0 \tag{2.45}$$

Combining the right-hand sides of Equations 2.43 and 2.44 yields Equation 2.46.

$$j\mu\Delta\omega(\vec{H}_1 \cdot \vec{H}_0^*) + j\varepsilon\Delta\omega(\vec{E}_1 \cdot \vec{E}_0^*) = j\Delta\omega(\varepsilon\vec{E}_0^* \cdot \vec{E}_1 + \mu\vec{H}_0^* \cdot \vec{H}_1) \tag{2.46}$$

Here, we consider $S_1 = S_0 - \Delta S$ and $\Delta\omega = \omega_0 - \omega_1$.

$$\oint_{S_0} (\vec{E}_0^* \times \vec{H}_1) \cdot \mathrm{d}\vec{s} - \oint_{\Delta S} (\vec{E}_0^* \times \vec{H}_1) \cdot \mathrm{d}\vec{s} = \int_{V_1} j\Delta\omega(\varepsilon\vec{E}_0^* \cdot \vec{E}_1 + \mu\vec{H}_0^* \cdot \vec{H}_1)\mathrm{d}v \tag{2.47}$$

where the $\vec{E}_{0_{tan}} = 0$ on the surface of unperturbed cavity. Assuming the perturbation on the cavity surface is small, the electric and magnetic field distributions of the perturbed cavity mode are considered equal to the unperturbed cavity mode.

$$\Delta\omega = \frac{\oint_{\Delta S}(\vec{E}_0^* \times \vec{H}_1) \cdot \mathrm{d}\vec{s}}{-\int_{V_1} j(\varepsilon\vec{E}_0^* \cdot \vec{E}_1 + \mu\vec{H}_0^* \cdot \vec{H}_1)\mathrm{d}v} \approx \frac{\oint_{\Delta S}(\vec{E}_0^* \times \vec{H}_0) \cdot \mathrm{d}\vec{s}}{-\int_{V_0} j(\varepsilon|\vec{E}_0|^2 + \mu|\vec{H}_0|^2)\mathrm{d}v} \tag{2.48}$$

Substituting Equation 2.43 into Equation 2.48 yields the normalized frequency shift:

$$\frac{\Delta\omega}{\omega_0} \approx \frac{\int_{\Delta V}(\varepsilon|\vec{E}_0|^2 - \mu|\vec{H}_0|^2\mathrm{d}v}{\int_{V_0}(\mu|\vec{H}_0|^2 + \varepsilon|\vec{E}_0|^2)\mathrm{d}v} \tag{2.49}$$

Note that the sign of terms in the numerator is associated with whether the defect on the cavity wall is inward or outward. In this notation, a minus sign may appear at the beginning of the equation for a different notation, considering the outward defect as positive and the inward defect as negative.

2.3.2.2. Dielectric Perturbation

A similar effect occurs when a portion or the entirety of a hollow cavity is filled with a dielectric material, resulting in a change in the resonance frequency of the corresponding mode. Here, the focus is on the quantification of this resonance frequency. Again, Ampère's and Faraday's equations are written for both cavities, and similar procedures can be repeated to find the frequency shift.

$$\nabla \times \vec{E}_0 = -j\omega_0\mu\vec{H}_0 \tag{2.50}$$

$$\nabla \times \vec{H}_0 = j\omega_0\varepsilon\vec{E}_0 \tag{2.51}$$

$$\nabla \times \vec{E}_1 = -j\omega_1\mu\vec{H}_1 \tag{2.52}$$

$$\nabla \times \vec{H}_1 = j\omega_1(\varepsilon + \Delta\varepsilon)\vec{E}_1 \tag{2.53}$$

where $\Delta\varepsilon$ denotes the change in the dielectric constant. After executing the same procedures, the frequency shift, under the assumption that the perturbing object is non-magnetic, can be expressed as follows.

$$\nabla \cdot (\vec{E}_0^* \times \vec{H}_1) = j\omega_0\mu\vec{H}_1 \cdot \vec{H}_0^* - j\omega_1(\varepsilon + \Delta\varepsilon)\vec{E}_1 \cdot \vec{E}_0^* \tag{2.54}$$

$$\nabla \cdot (\vec{E}_1 \times \vec{H}_0^*) = -j\omega_1\mu\vec{H}_1 \cdot \vec{H}_0^* + j\omega_0\varepsilon\vec{E}_1 \cdot \vec{E}_0^* \tag{2.55}$$

Sum the equations, perform integration over V_0 and apply the divergence theorem.

$$\oint_{S_0} (\vec{E}_0^* \times \vec{H}_1 + \vec{E}_1 \times \vec{H}_0^*) \cdot \mathrm{d}\vec{s} = 0 \tag{2.56}$$

$$j\int_{V_0} \Delta\omega(\varepsilon\vec{E}_0^* \cdot \vec{E}_1 + \mu\vec{H}_0^* \cdot \vec{H}_1) - (\omega_1\Delta\varepsilon)\vec{E}_0^* \cdot \vec{E}_1 \mathrm{d}v = 0 \tag{2.57}$$

When we isolate the normalized frequency shift, the following equation emerges.

$$\frac{\Delta\omega}{\omega_1} = \frac{\int_{V_0}(\Delta\varepsilon E_0^* \cdot \vec{E}_1)\mathrm{d}v}{\int_{V_0}(\mu\vec{H}_0^* \cdot \vec{H}_1 + \varepsilon E_0^* \cdot \vec{E}_1)\mathrm{d}v} \tag{2.58}$$

This equation provides an exact representation of the frequency shift, but its practical utility is limited due to the unknown nature of the exact fields in the perturbed cavity mode. However, if we assume the changes are small, we can approximate the resonant frequency shift as follows.

$$\frac{\Delta\omega}{\omega_0} \approx \frac{\int_{V_0}(\Delta\varepsilon|\vec{E}_0|^2)\mathrm{d}v}{\int_{V_0}(\mu|\vec{H}_0|^2 + \varepsilon|\vec{E}_0|^2)\mathrm{d}v} \tag{2.59}$$

where $\Delta\omega = \omega_0 - \omega_1$. According to the adopted notation, it is consistently observed that this quantity is positive. In essence, this implies that a perturbation induced by a dielectric material has the exclusive capability to reduce the resonant frequency of the perturbed mode, in contrast to metallic perturbations, which possess the capacity to elevate it.

2.4. Numerical Electromagnetism

Electromagnetic problems often present their complexity that requires numerical methods. Several numerical techniques are followed for simulating electromagnetic phenomena, such as Finite Element Method (FEM), Finite Difference (FD), and Finite Difference Time Domain (FDTD). From the perspective of this thesis, simulations were carried out with the aid of CST-MWS software using the FEM numerical technique. FEM is a numerical method used to solve partial differential equations and boundary value problems. It is one of the most applied techniques in a variety of fields, among others, engineering, physics, and applied mathematics. There is an underlying idea regarding FEM: the problem under investigation is made much simpler than the original problem by cutting the domain into finer parts. These smaller parts are called finite elements, and each of them approximates the behavior of the solution within its domain. Once the solution of the problem is expressed in piecewise form using these elements, the original problem is reduced to a collection of algebraic equations, which can be solved numerically.

Consider a Laplace's equation in 2D with triangular elements.

$$\Delta V = 0 \tag{2.60}$$

$$V(x, y) \approx \sum_{i}^{N} V_e(x, y) \tag{2.61}$$

where N is the number of elements. If we focus on the potential of an element, the node potentials can be expressed as follows:

$$\begin{bmatrix} V_{e1} \\ V_{e2} \\ V_{e2} \end{bmatrix} = \begin{bmatrix} 1 \; x_1 \; y_1 \\ 1 \; x_2 \; y_2 \\ 1 \; x_3 \; y_3 \end{bmatrix} \begin{bmatrix} a \\ b \\ c \end{bmatrix} \tag{2.62}$$

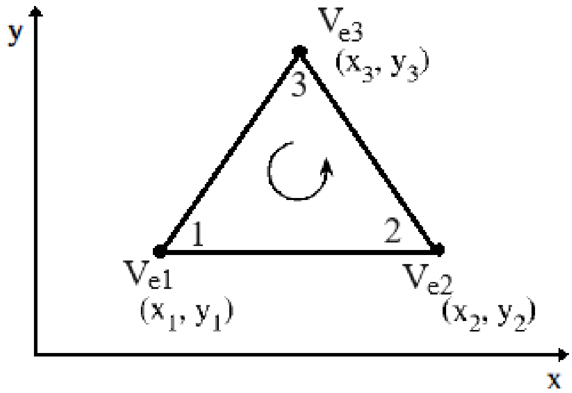

Figure 2.4. A triangular element

$$V_e(x, y) = \begin{bmatrix} 1 \; x \; y \end{bmatrix} \begin{bmatrix} 1 \; x_1 \; y_1 \\ 1 \; x_2 \; y_2 \\ 1 \; x_3 \; y_3 \end{bmatrix}^{-1} \begin{bmatrix} V_{e1} \\ V_{e2} \\ V_{e2} \end{bmatrix} \tag{2.63}$$

A global coefficient matrix should be constructed to observe the interaction between multiple elements, leading to the final solution. Detailed information on how to construct the global coefficient matrix can be found in (Sadiku, 2000). Throughout the thesis study, the CST-MWS software's frequency domain solver, as well as its eigenmode solver, utilize this algorithm for computation.

2.5. Lagrange Multipliers and Slack Variables

Consider the optimization problem of maximizing (or minimizing) a function $f(x)$ subject to inequality constraints:

$$\text{Maximize} \quad f(x) \tag{2.64}$$

$$\text{subject to} \quad g_i(x) \leq 0, \quad i = 1, 2, \ldots, m \tag{2.65}$$

where $x \in \mathbb{R}^n$ is the vector of decision variables, $f(x)$ is the objective function, and $g_i(x)$ are the inequality constraint functions. To solve this problem using Lagrange multipliers, we define the Lagrangian function as:

$$L(x, \vec{\lambda}) = f(x) - \sum_{i=1}^{m} \lambda_i g_i(x) \tag{2.66}$$

where $\vec{\lambda} = [\lambda_1, \lambda_2, \ldots, \lambda_m]^T$ are the Lagrange multipliers. To incorporate the inequality constraints into the optimization problem, we introduce slack variables $s_i^2 \geq 0$, such that the constraints become equalities as:

$$g_i(x) + s_i^2 = 0, \quad i = 1, 2, \ldots, m. \tag{2.67}$$

The Lagrangian function then becomes:

$$L(x, \vec{\lambda}, \vec{s}) = f(x) - \sum_{i=1}^{m} \lambda_i (g_i(x) + s_i^2) \tag{2.68}$$

Complementary slackness conditions are important in solving optimization problems with inequality constraints by using the Lagrange multipliers. These indicate that if the Lagrange multiplier is zero at an optimal solution for a given constraint, then the constraint is active. Alternatively, when the Lagrange multiplier is non-zero, then the constraint is inactive. These two conditions correspond to the Karush-Kuhn-Tucker conditions. Such conditions specify what happens when x^* is the optimal solution to a constrained optimization problem. It is applied to the gradients of the Lagrangian function being zero with the satisfied constraints, and it also satisfies the complementary slackness condition. Conditions of complementary slackness can be expressed as:

$$\lambda_i^* s_i^* = 0. \tag{2.69}$$

CHAPTER 3

LIQUID METAL-ASSISTED DUAL PORT ANTENNA

This chapter is devoted to DP self-diplexing microstrip antenna and presenting the outcomes of the proposed network. The operating frequencies of the antenna were selected as 6.6 GHz and 7 GHz because the 6 GHz band was opened for unlicensed use (Federal Communications Commission (FCC), 2020). The proposed antenna exhibits computational advantages over existing literature counterparts. This is achieved through the utilization of a standard microstrip, the reduction of the electrical size using a DGS, and taking advantage of the symmetry in the proposed network to simulate only half of the antenna. Notably, its geometry maintains a small electrical size at both frequencies and avoids the use of structures imposing additional computational burdens such as SIW. These approaches not only lead to a shorter simulation time but also contribute to minimizing production costs. In addition, the DP antenna under consideration allows for independent adjustment of both ports through minor modifications. This adaptability is achieved by altering dimensions related to defects on the ground plane or adjusting the widths of the ground planes. Some of these slight adjustments can be implemented using two fluid channels and 2.5 g of LM, specifically gallium. Additionally, a cost-effective 3D printer-assisted method is introduced for the fabrication of the proposed antenna. The results in this chapter have been published as an article in (Karatay, 2022).

3.1. Dual-Port Antenna Design

This section focuses on explaining the details of the antenna design and presenting the final dimensions of the antenna. In addition, we explore how parameters affect the operating frequency and describe how the infrastructure for LM-assisted frequency reconfiguration is set up. The dielectric properties of FR-4 substrate, defined with a height of h in Table 3.1, may vary from manufacturer to manufacturer and from model to model. However, simulations have been conducted by generally adopting a dielectric constant of 4.25 and a loss tangent value of 0.02. The front side of the proposed antenna comprises two ports facing each other and a circular fractal structure with three steps. On the back side, there are two separate ground planes and a total of four eight-shaped defects, as illustrated in Figure 3.1. The final values of the proposed design were determined using CST - Microwave Studio and are given in Table 3.1. The parameter h is the substrate height, and e represents the distance of the defects to the nearest edge, as shown in Figure 3.1-(b).

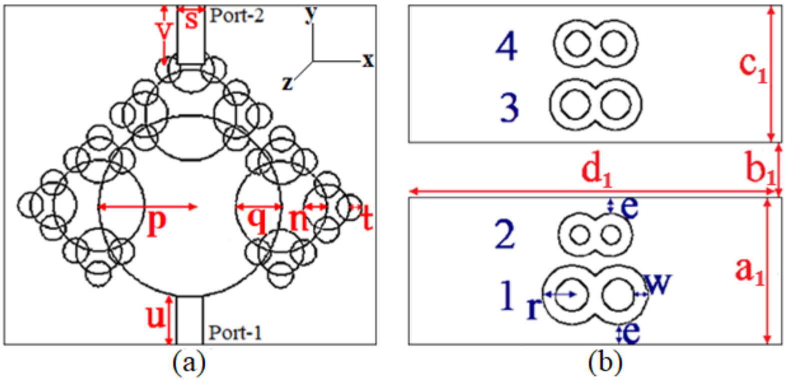

Figure 3.1. Dimensions of the DP antenna (a) front side (b) back side (Karatay, 2022)

Table 3.1. Dimensions of the proposed antenna in mm.

s	v	u	p	q	n	t	a_1	b_1	c_1	d_1	r_1
2.74	6	4.5	9	4.5	2.25	1.25	14.4	5.475	13.625	37	2.92
r_2	r_3	r_4	w_1	w_2	w_3	w_4	e_1	e_2	e_3	e_4	h
2.1	2.5	2.3	1.24	1.1	0.98	0.98	1.85	1.6	1.2	1.6	1.5

The filtering response of the DGS was evaluated prior to antenna design simulations. A DP microstrip line without defects, followed by one with a full gap and then an eight-shaped defect, was simulated. Figure 3.2 shows S_{11} parameters at each step. The microstrip line had over 20 dB return loss without defects. Introducing a rectangular gap increased the S_{11}, and with the eight-shaped defect, S_{11} dropped below -20 dB at specific frequencies. The DGS acts as an equivalent LC circuit, providing frequency-selective features where capacitance and inductance are given with:

$$C = \frac{\omega_c}{2Z_0(\omega_0^2 - \omega_c^2)} \tag{3.1}$$

$$L = \frac{1}{\omega_0^2 C} \tag{3.2}$$

where ω_0 and ω_c are the angular resonant frequency and cut-off frequency, respectively. Z_0 is the characteristic impedance.

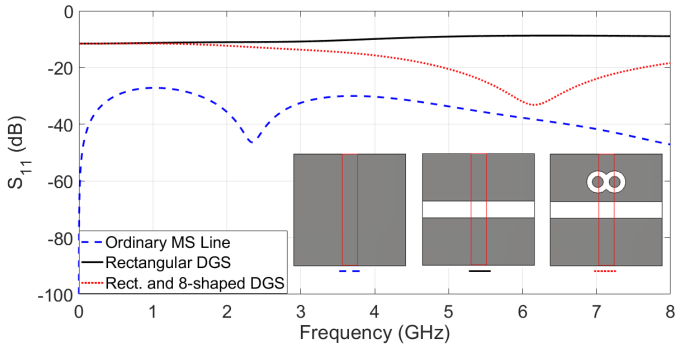

Figure 3.2. Filtering with DGS (Karatay, 2022)

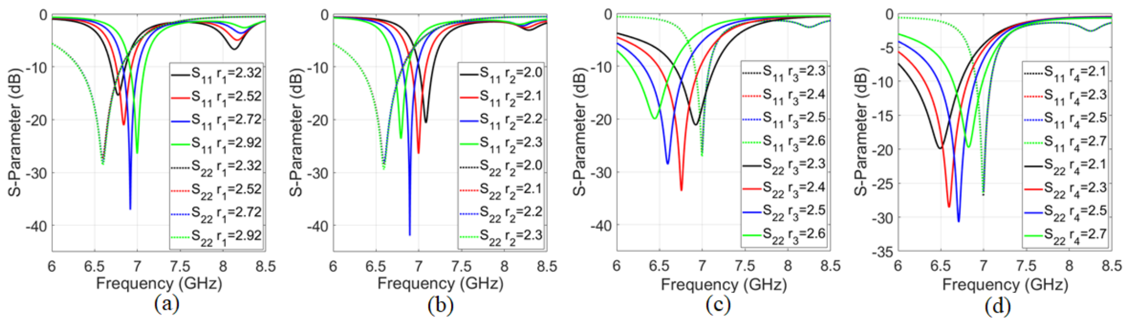

Figure 3.3. Effect of (a) r_1 (b) r_2 (c) r_3 (d) r_4 in mm on the S-parameters (Karatay, 2022)

The eight-shaped defects have been included in the design process with the intention of achieving symmetry while reducing the electrical length at dual frequencies, as shown in Figures 3.3 and 3.4. Symmetry, in this context, implies a mirrored arrangement of the antenna and ports with respect to a plane bisecting the structure. Figure 3.3 shows the effect of the outer radius (r) of eight-shaped defects on the operational frequency of the antenna, and the dimensions are marked in millimeters. Notably, r_1 and r_2 influence only the first port, while r_3 and r_4 affect the second port alone, showing flexibility for redesigns. The parameter S_{21} was excluded in the graphic representation because isolation between the ports appeared fairly similar from each other in simulations. Separate individual assessments of each defect's absence and its impact on S_{11}, S_{21}, and S_{22} are presented in Figures 3.4. Legends with 'w/o' show complete conversion of the corresponding defect region into the ground plane, and 'NOCHG' reflects a situation where no changes are applied to the proposed antenna. It is important to note that the absence of defects results in an increase in frequency, showing that there is a greater electrical length with an indication of resulting differentiation in the isolation parameter.

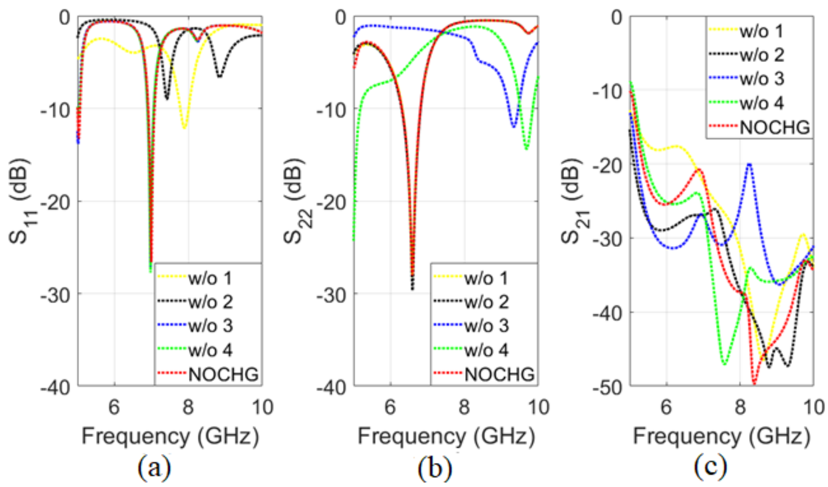

Figure 3.4. Lack of eight-shaped defects on (a) S_{11} (b) S_{22} (c) S_{21} (Karatay, 2022)

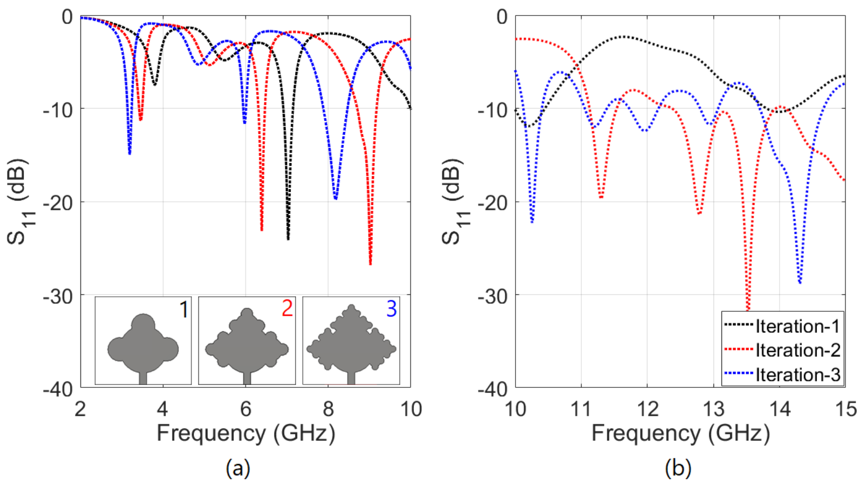

Figure 3.5. Effect of the fractals (a) 2-10 GHz (b) 10-15 GHz (Karatay, 2022)

In addition to this, another investigation was carried out on the effects of fractal geometry on the S_{11} parameter using simulation. Both the ground plane defects and the second port of the antenna were completely removed to isolate the effect of the fractal geometry. In this particular situation, there are two apparent trends. Between 2 and 10 GHz, there is a decline in operating frequency, indicating the electrical area reduction such that in Figure 3.5-(a), one can see an increasing tendency while keeping the total physical area constant. On the other hand, for frequencies ranging from 10 to 15 GHz, there is an upturn in the total number of dips with the growing number of iterations. This points to the consideration of great importance in the design of multiband or wideband antennas, illustrated in Figure 3.5-(b).

3.2. Simulation and Measurement Results

The antenna prototype was produced by chemical etching, while the SMA connectors were attached to the ports. Finally, S-parameter measurements were made with an HP 8720D 50 MHz-20 GHz Vector Network Analyzer (VNA), followed by measurement of the pattern and gain at the anechoic chamber. Figure 3.6 depicts a comparison between the simulated and measured S-parameters for the antenna. The lower right part of the graph illustrates a detailed view of the antenna front, back, and measurement setup in an anechoic chamber. Thus, observations that need consideration include dips in the lower right plot of S_{22} at 6.6 GHz in simulation and 6.615 GHz in measurements, with 7 GHz and 7.011 GHz showing dips in the S_{11} plot. Correspondingly, isolated values in simulation at operating frequencies are in good agreement at 22 dB, while the VNA measurements are at 24 dB and 26 dB. Realized gain values are given as follows from the simulation: 4.49 dBi for the first port, whose working frequency is 7 GHz in simulation and 4.17 dBi in measurement. For the second port, where the working frequency is 6.6 GHz, the realized gain is 4.09 dBi in simulation and 3.93 dBi in measurement.

Subsequently, the prototype production of the same antenna was executed using the 3D printed masking method, and fundamental parameters were measured with the assistance of a VNA; Figure 3.7. The conductive spray's susceptibility to high temperatures prevented the use of hot soldering. Consequently, SMA adapters were connected to the antenna using cold soldering, preventing impedance mismatch due to conductivity loss at the connection point. S_{11} showed a minimum of -19.5 dB at 7.03 GHz, and S_{22} demonstrated a dip of -34.8 dB at 6.55 GHz. The isolation between ports is -26 dB for both operating frequencies. The gain of the antenna manufactured using the new method was measured in an anechoic chamber. Due to the lower conductivity of the aerosol compared to copper, there is a slight decrease in gain; however, the measured gains at levels of 3.72 and 3.81 dBi, respectively, are sufficiently good for many applications.

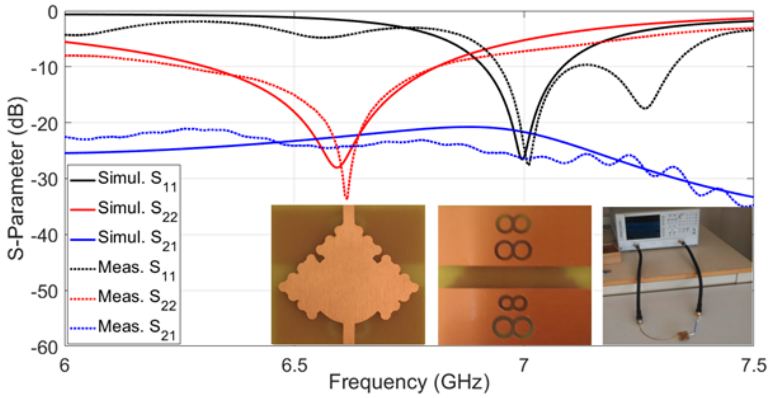

Figure 3.6. S-parameters of the antenna fabricated with chemical etching method (Karatay, 2022)

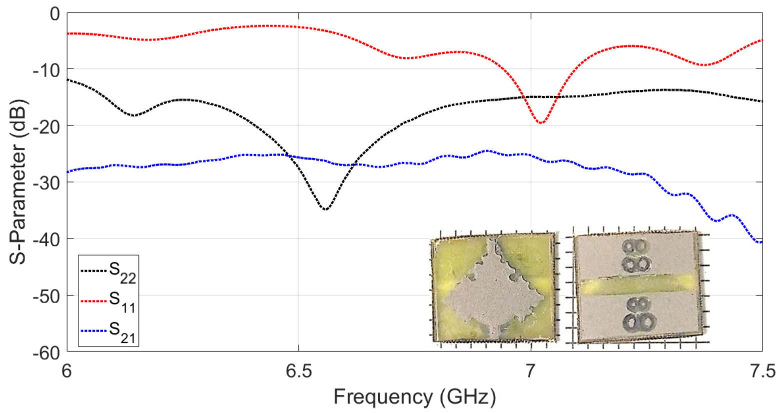

Figure 3.7. S-parameters of the antenna fabricated with the aid of a 3D printer (Karatay, 2022)

Figure 3.8 depicts the normalized patterns of the antenna fabricated with chemical etching for each port across two planes, as detailed in the coordinate system provided in Figure 3.1-(a). The subfigures present results for cross-polarization and co-polarization. A front-to-back ratio (FBR) of approximately 6 dB was observed for both ports. As it is assumed that the far-field pattern will not vary significantly for both antennas, an additional measurement was not required for the 3D-printed one. Due to the considerably lower cross-polarization power levels compared to co-polarization, approaching noise levels may result in discrepancies. Nevertheless, good cross-polarization suppression and agreement between simulation and measurement have been reported.

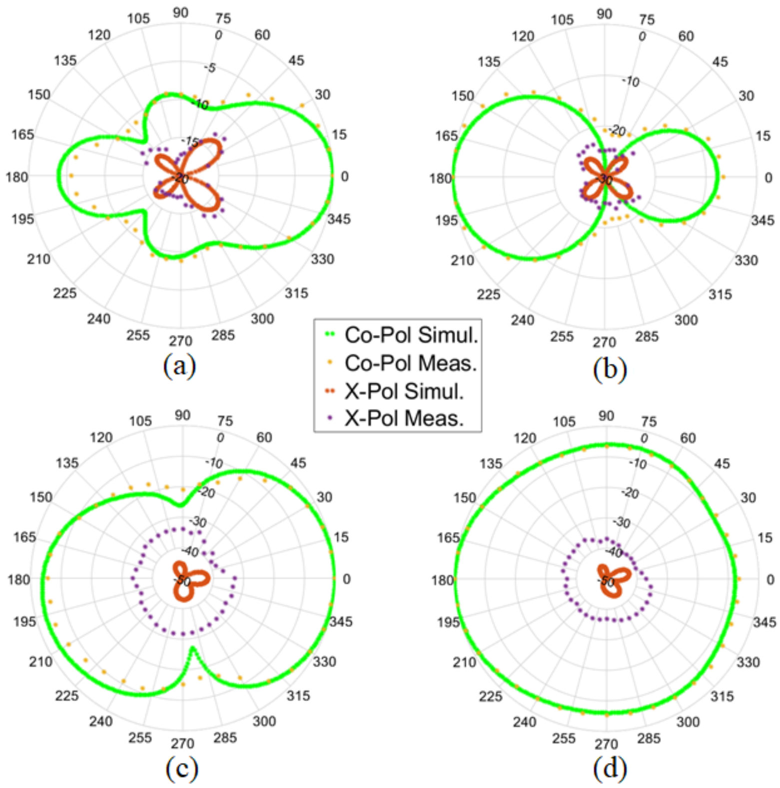

Figure 3.8. Normalized far-field graphs (a) x-z plane for port 2 (b) x-z plane for port 1 (c) y-z plane for port 2 (d) y-z plane for port 1 (Karatay, 2022)

3.3. Comparison

In this section, a comparison is provided between the proposed antenna and DP counterparts in the literature; see Table 3.2. Initially, the operating frequency of the proposed antenna is given along with the operating frequencies of those in the literature. While discussing advantages or disadvantages may not be meaningful, having information about the operating frequencies will be useful in calculating the electrical size. One of the significant advantages of the proposed antenna is the independent readjustment of the operating frequencies of both ports. This allows an end user interested in redesigning the antenna to maintain the operating frequency of one port while altering the other, either through reproduction or by utilizing LM-based reconfiguration methods. The electrical size of the proposed antenna is smaller than that of its counterparts in the literature. Calculations for both operating frequencies reveal that the proposed structure is noticeably compact in terms of both short and long wavelengths. Due to its mirror symmetry and microstrip-based structure, the operational load during the design phase is considerably lower compared to SIW structures and structures lacking symmetry features.

Table 3.2. Comparison of the proposed DP antenna with the literature (PSC: Phase-shifting circuit, MS: Microstrip, SIW: Substrate-integrated waveguide, SP: Symmetry plane) (Karatay, 2022)

	Frequency (GHz)	Indep. Ports	Area (λ^2_{long})	Area (λ^2_{short})	SP	Type
Proposed Antenna	6.6 & 7	✓	0.60	0.68	✓	MS
(Kumar and Raghavan, 2018)	8.2 & 10.6	✗	0.74	1.22	✗	SIW
(Nandi and Mohan, 2018)	8.6 & 9.8	✓	0.78	1.02	✗	SIW
(Nandi and Mohan, 2017)	8.3 & 10.5	✓	0.63	1.01	✓	SIW
(Mukherjee and Biswas, 2016)	9.0 & 11.2	✓	1.17	1.81	✗	SIW
(Nawaz and Tekin, 2015)	2.4	✗	1.16		✗	PSC
(Li et al., 2011)	2.6	✗	1.08		✗	MS
(Nawaz and Tekin, 2018)	2.4	✗	0.67		✗	MS

3.4. Liquid Metal-Assisted Frequency Reconfiguration

We built an experimental setup in which LM is demonstrated, having independent redesign capability. A dielectric holder was placed in the gap between the two ground planes, where it has two channels with a thickness of 0.9 mm. This arrangement enabled independent frequency reconfiguration for each port and three different frequency states: State-0, representing the empty holder; State-1, where the medium is placed near Port-1 with gallium; and State-2, where the medium is placed near Port-2 with gallium, as depicted in Fig. 3.9. Figure 3.10 provides the subsequent simulations and measurements for the frequency states. When the dielectric holder was empty, there was a tiny shift in the operating frequency of the first port. During the transition from State-0 to State-1, a 6.92 GHz simulated operating frequency in the first port moves to 6.63 GHz. In the measurement, a shift from 6.91 GHz to 6.55 GHz is observed. According to the measurements, the value of S_{22} in State-0 and State-1 was observed at 6.56 GHz, while in simulation, it was measured at 6.5 GHz. In State-2, the frequency of the S_{11} dip from

State-0 was the same as that of State-2. The dip of S_{22} in the measurement was 6.27 GHz, while in simulation, it was 6.20 GHz. Throughout the reconfiguration facilitated by LM, the physical area remains constant while its operating frequency reduces, signifying a decrease in the electrical size.

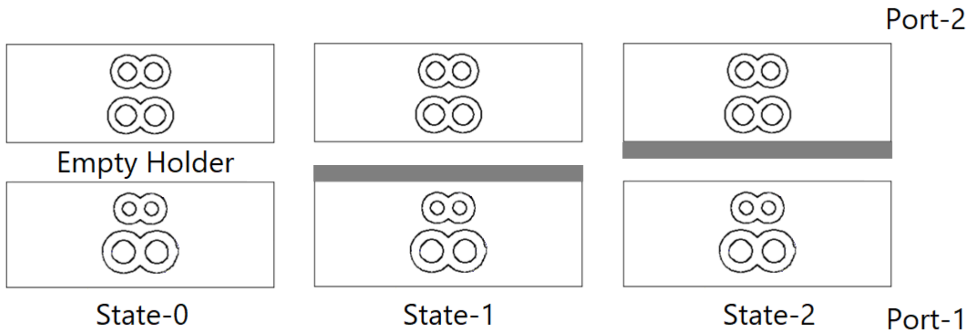

Figure 3.9. LM-based frequency states (Karatay, 2022)

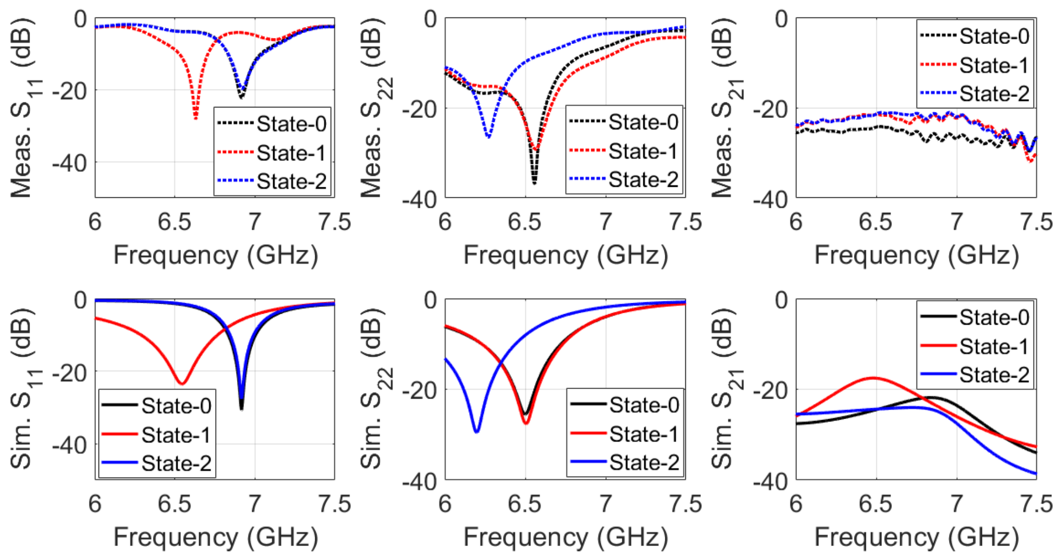

Figure 3.10. S-parameters of LM-assisted frequency reconfigurable DP antenna (Karatay, 2022)

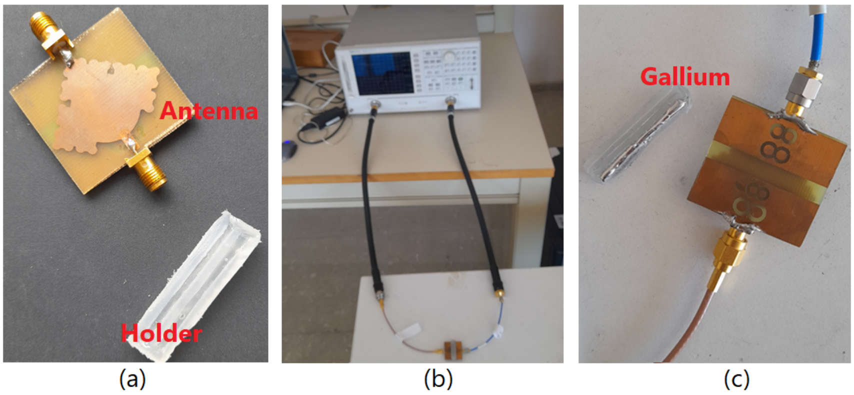

Figure 3.11. Photos of (a) the antenna with the empty holder (b) the setup (c) the antenna with the LM-filled holder (Karatay, 2022)

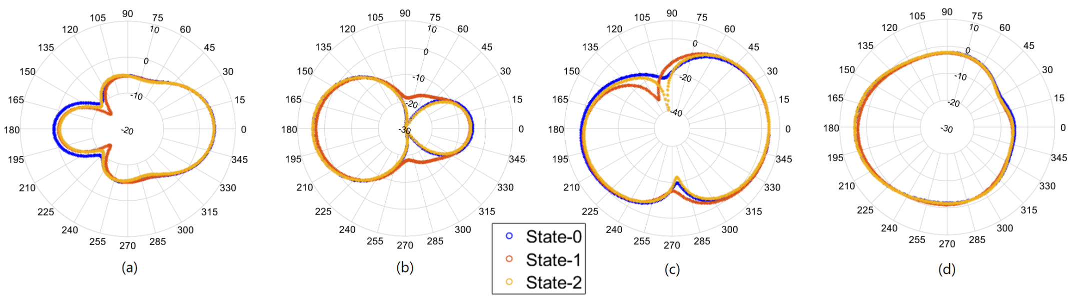

Figure 3.12. Far-field simulations at the operating frequencies for (a) x-z plane port 2 (b) x-z plane port 1 (c) y-z plane port 2 (d) y-z plane port 1 (Karatay, 2022)

Images illustrating the proposed antenna, the measurement setup, and filling the double-lined holder with LM can be found in Figure 3.11. Although it is recommended that VNA measurements be performed in an anechoic chamber, just like radiation pattern and gain measurements, there is no detriment in performing them in a laboratory environment without an anechoic chamber since we do not see a significant difference in the scattering parameter between these two scenarios. It is also imperative that other parameters do not deteriorate as a result of the frequency reconfiguration process. Therefore, the far-field pattern was checked with CST-MWS to see whether it had changed. Additionally, no significant variation has been observed in the far-field plot, as seen in Figure 3.12. No notable alteration was observed in the simulation and measurement regarding the maximum realized gain value at the antenna's revised operating frequency.

3.5. Discussions

This chapter discusses the independent reconfiguration of operating frequencies for a novel DP antenna using LM assistance, and the findings are concluded. First, an antenna is presented in the initial stage, operating at 7 GHz for the first port and 6.6 GHz for the second port. In order to make sure the coupling level remains below -20 dB between the antenna ports, attention has been given to coupling between ports. This antenna has several benefits compared to those available in the literature. Firstly, the electrical size of this antenna is small compared to other structures with similar properties in the literature, and, in terms of manufacturing, it is easy. A large proportion of such structures is built as SIW-based structures, where coupling is minimized using various modes of those structures. However, the production of SIW-based antennas is challenging and expensive. Moreover, their simulation requires a large computational load. The most significant solution to the problem of high computational load is mirror symmetry, which cuts both ports in half. Therefore, it is possible to simulate the electromagnetic behavior of the whole structure by simulating only half of the antenna. Secondly, going for a classical microstrip structure instead of SIW not only lowers the computational load but also helps in reducing the cost of fabrication.

The core novelty leading to the emergence of the proposed antenna is the ability to independently reconfigure the operating frequency of each port in the DP structure. Simulation results were presented concerning the dimensions and the absence of eight-shaped defects. It was shown that the operating frequency of that particular port is changed only within a dimension of the ground plane of that specific port. This result provides the basis for LM-assisted independent frequency reconfiguration. LM-assisted frequency reconfiguration requires several considerations. First and foremost, it is essential to ensure that the dielectric constant of the holder is not high, thus allowing a negligible range for frequency shifting in State-0. Second, the thickness of the used holder must be kept minimal, and the loss tangent value must be negligible. It ensures that both the frequency shift and the gain reduction are LM-induced and reduced, respectively.

The simulation and measurement results show that LM assists in the enlarged ground planes of the ports, making it possible for an independent reduction of their operating frequencies. One considerable advantage of the antenna lies in the fact that, during this process, not only is the operating frequency of the other port unchanged, but also there are no substantial changes in values such as gain and radiation pattern. It is crucial to consider the frequency of operation for this antenna, especially when considering the suitability of this band for unlicensed use. It may raise doubts about the practicality of the antenna in such applications. However, it would simultaneously lead to a change in gain or pattern and is good enough for unlicensed indoor or outdoor applications.

CHAPTER 4

LIQUID METAL-CONTROLLED DOPPLER RADAR

This chapter discusses the design and operation of a Doppler radar under different operating conditions and the intended monitoring for the first radar signal. The research work is implemented in the form of a control over the transmitter and receiver antennas, as well as the PD, using an MIT-CCDR-based Doppler radar in this study. The control of the main lobe, i.e., the scanning direction of the radar, is accomplished using LM. Such a control was intended to provide a more stable method than conventional electrical reconfiguration methods. Those two identical antennas enable simultaneous operation at 2.45 GHz and 5.8 GHz with a combined PD, which also includes LM-assisted frequency switching for the DB Doppler radar.

From the antenna design process, the exploration of enhancing the gain and FBR values of a single-element Vivaldi antenna led to an attempt to change these parameters with a change in cavity size. This subsequent experiment has now numerically and experimentally shown that, with back-to-back positioning of two Vivaldi antennas, the direction of the main lobe of one of the antennas can be controlled by shutting the cavity of just one of the antennas. All the gained findings are validated effective at both 2.45 GHz and 5.8 GHz. A T-junction PD with switching capabilities at these two frequencies was designed for operation at both frequencies. All the components were combined with the radar, and various measurements were made with the radar. The results in this chapter have been published in the article (Karatay and Yaman, 2024a).

4.1. Single Band Vivaldi Antenna

In this section, the design, fabrication, and measurement processes of the SB Vivaldi antenna are elaborately explained. The incorporation of the beam-switching feature into the structure using LM is also detailed in this section. This feature enables the antenna to dynamically adjust its beam direction, providing enhanced flexibility for applications requiring directional control.

4.1.1. Single Band Vivaldi Antenna Design

This subsection is devoted to the design of a Vivaldi antenna to construct an LM-controlled Doppler radar. For this purpose, a single-element Vivaldi antenna at 2.45 GHz was designed in the first step. The dielectric layer of the antenna consists of an FR-4 substrate with a thickness of 1.5 mm, a dielectric constant of 4.3, and a loss tangent of 0.025. The dimensions of the designed Vivaldi antenna are detailed in Figure 4.1-(a) and 4.1-(b) in millimeters. Literature offers several approaches for calculating initial values for parametric sweep (Perdana et al., 2017; Navarro-Mendez et al., 2015; Wang et al., 2013). Following meticulous optimization, the individual element's overall size was determined to be 102.6×60.8 mm^2. Given the intention to use two Vivaldi antennas back-to-back, mitigating the back-lobe level of the elements becomes crucial. Slots were strategically incorporated into the sides of the metal surface of the antenna to achieve this, totaling twelve slots (six on each side). The dimensions of these slots are presented in Figure 4.1-(c).

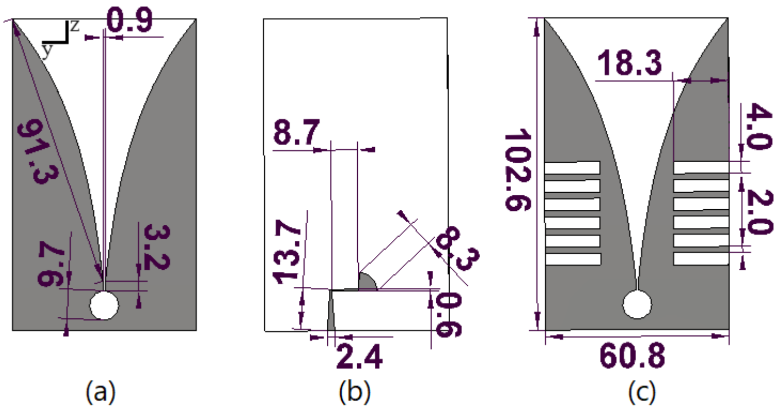

Figure 4.1. Model of the single element Vivaldi antenna (the dimensions are given in mm) (a) Ground plane of the original Vivaldi (b) Feed line (c) Modified Vivaldi

In Figure 4.2, simulated far-field patterns of the original and modified versions of the antenna are shown on two different planes. In Figure 4.2-(a), ϕ angle is fixed to 90 degrees, and θ angle is rotated. In Figure 4.2-(b), ϕ angle is fixed to 0 degrees. For both planes, the slots added to the antenna improve the antenna's gain and the FBR. While the antenna's maximum gain was 3.58 dBi without slots, this value increased to 7.01 dBi with the proposed modification. In addition, while the FBR was $\sim$ 4.4 dB in the original antenna, it increased to $\sim$ 18 dB thanks to the modification made by adding slots. In Figure 4.2-(a), the half-power beam width decreases from $\sim$ 120 degrees to $\sim$ 60 degrees, while in Figure 4.2-(b) the change is from $\sim$ 120 degrees to $\sim$ 110 degrees.

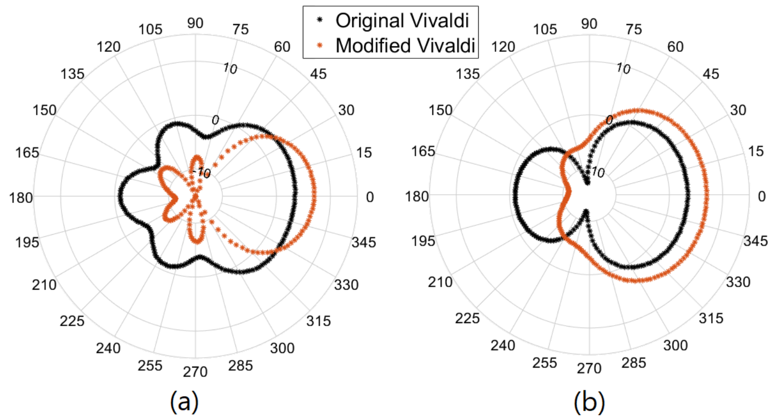

Figure 4.2. Simulated far-field patterns of the antennas at 2.45 GHz (a) $\phi = 90°$ (b) $\phi = 0°$

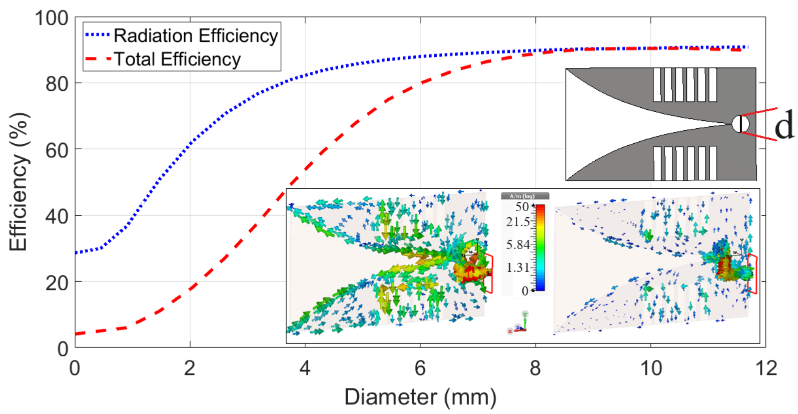

Figure 4.3. Efficiency variations of the Vivaldi antenna at 2.45 GHz w.r.t. the cavity diameter. The surface currents correspond to $d = 9.7$ mm and $d = 0$ mm, respectively: ©2023 IEEE (Karatay and Yaman, 2024a)

The cavity of the Vivaldi antenna, having a diameter of 9.7 mm, significantly impacts its radiation efficiency. According to simulation results, the radiation efficiency for this component reaches 90.3% at 2.45 GHz. If completely filled with metal, efficiency drops to 28.6%, as given in Figure 4.3. In this case, the total efficiency value drops to as low as 4.2%. In such a situation, on the other hand, if both the radiation efficiency and total efficiency are affected, it should be noted that there would be higher losses and impedance mismatch. Surface currents for the $d = 9.7$ mm and $d = 0$ mm cases are visualized in the lower right corner. In this situation, the loss of surface currents is rendered insignificant, rendering the antenna non-operational. These results will further serve as the working principle for the following back-to-back Vivaldi antenna, where the antenna's main lobe can be determined using this method.

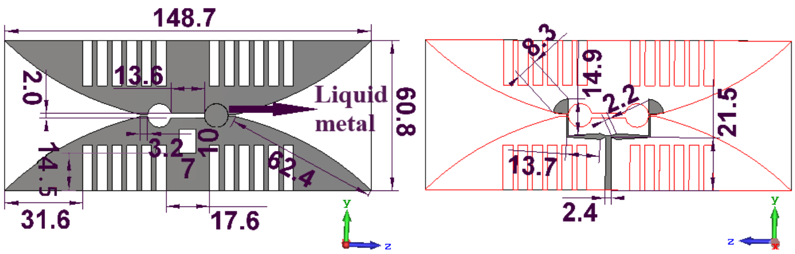

Figure 4.4. SB back-to-back Vivaldi antenna dimensions in mm: ©2023 IEEE (Karatay and Yaman, 2024a)

The antennas were combined and fed from a single port to form a back-to-back Vivaldi antenna. At first, the reorganization of the antenna size was prompted by an examination. Some parametric studies were conducted to reduce size, balancing trade-offs through optimization. A balance between a compact structure and maintaining the gain above 5 dBi was attained throughout the optimizing process while keeping FBR values acceptable. Detailed particulars on the structure and dimensions of the antenna are shown in Figure 4.4. The input impedance was adjusted on the feed line to obtain 50 Ω. After positioning two antennas back-to-back, a fluidic line was introduced between the cavities of the antenna. The primary purpose of this fluidic line is to facilitate the flow of liquid gallium between the cavities. Filling the left cavity will direct the main lobe towards +z, while filling the right cavity will direct it towards -z. A smooth flow line for gallium is maintained between the cavities by the central line. If one of the two cavities of the antenna is filled, the operating frequency is precisely 2.45 GHz. In the case where both cavities are empty simultaneously, the operating frequency decreases. Therefore, two different states for the antenna are set up: State-1 will radiate the main lobe towards +z, while State-2 will towards -z.

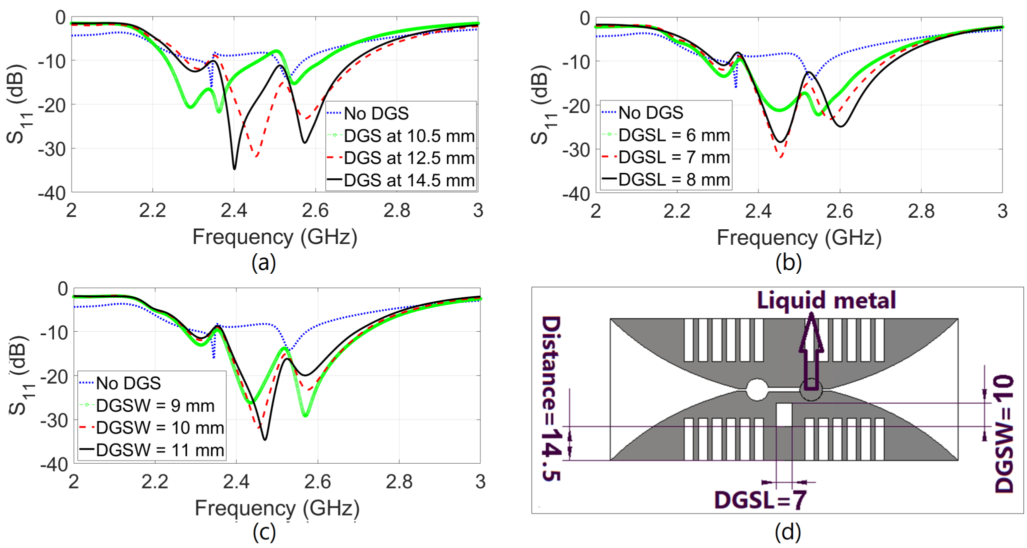

Figure 4.5. Parametric sweep on the DGS (a) Distance (b) DGSL (c) DGSW (d) Parametric sweep geometry (in mm)

We introduced a DGS in the ground plane of the feed line to achieve the desired impedance matching. The position where this defect will be placed on the line, whose optimum size was determined as 7×10 mm^2 with a detailed parametric sweep, is also critical. The simulation results run by changing the position of the defect when one of the cavities was filled with gallium is given in Figure 4.5-(a). It is seen that the reflection coefficient at the operating frequency varies as the location of the defect changes. The optimum value was reached with a gap of 14.5 mm between the lower end of the defect and the lower edge of the antenna. In Figure 4.5-(b) and 4.5-(c), the effects of length and width were observed by varying the corresponding parameters of the DGS. Both parameters shift the operating frequency and affect the reflection coefficient of the respective mode of the antenna. In these two simulations, the distance was kept constant at 14.5 mm. The antenna geometry on which the simulations are run and the changed parameters can be seen in Figure 4.5-(d). Note that the thickness of the LM filling the cavity was assumed to be 35 μm, like the copper of the microstrip antenna. However, since the gallium thickness in the fabricated antenna would be more than 35 μm, the effect of this was also checked in the simulation. No significant change was observed in either the scattering parameters or the gain values with the increased thickness up to 550 μm.

In the last step of the simulation part, a liquid holder, which is seen in Figure 4.6-(a), was attached to the antenna. The changes in the operating frequency and gain of the antenna were examined. The height of the holder having a dielectric constant of 3.2 was chosen as 3 mm and the thickness as 1 mm. Holder's presence appears to have a rather small effect on the operating frequency, $\sim$ 2 MHz; see Figure 4.6-(b). Figure 4.6-(c) and 4.6-(d) show the radiation patterns of State-1 and State-2, respectively, obtained by LM displacement. The maximum directivity is oriented in the direction of the cavity that is not filled with gallium. The operating frequency in both states is 2.45 GHz.

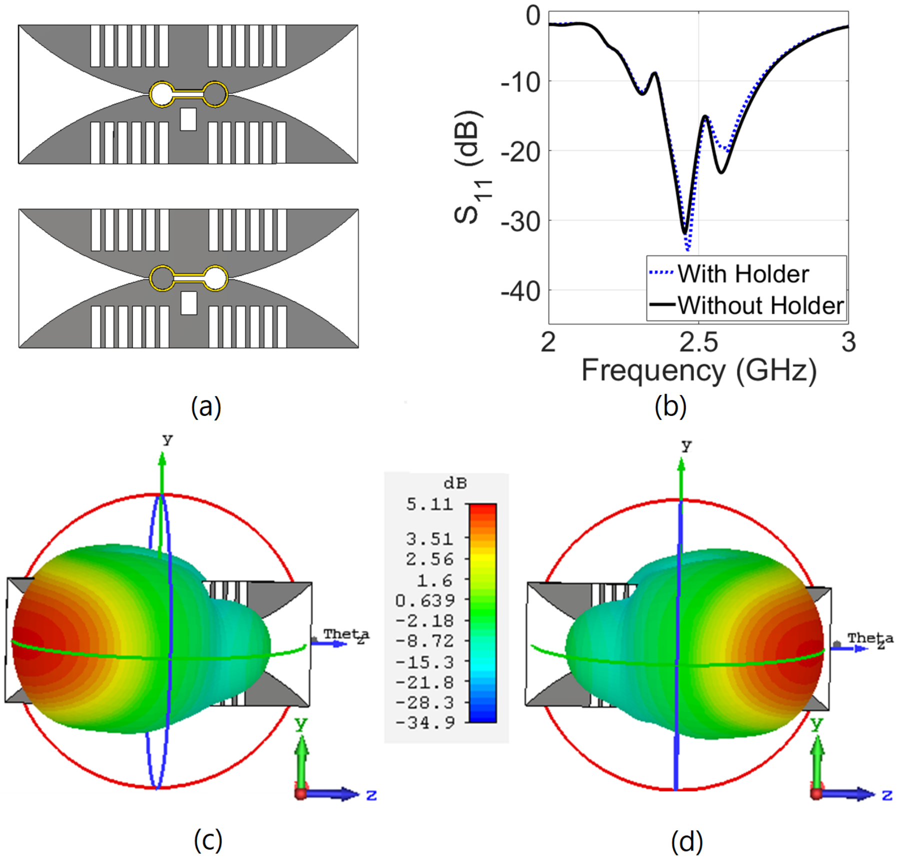

Figure 4.6. Simulation results of the SB Vivaldi antenna with a liquid holder (a) Antenna geometry in State-2 and State-1, respectively (b) Effect of the holder on S_{11} (c) Radiation pattern on State-2 at 2.45 GHz with the holder (d) Radiation pattern on State-1 at 2.45 GHz with the holder

4.1.2. Single Band Vivaldi Antenna Results

In this subsection, we delve into the measurement results of the produced antenna and make comparisons with the simulations. After finalizing the fabrication of the proposed antenna by using the FR-4 substrate, gain and pattern measurements were conducted in an anechoic chamber using a signal generator and a spectrum analyzer.

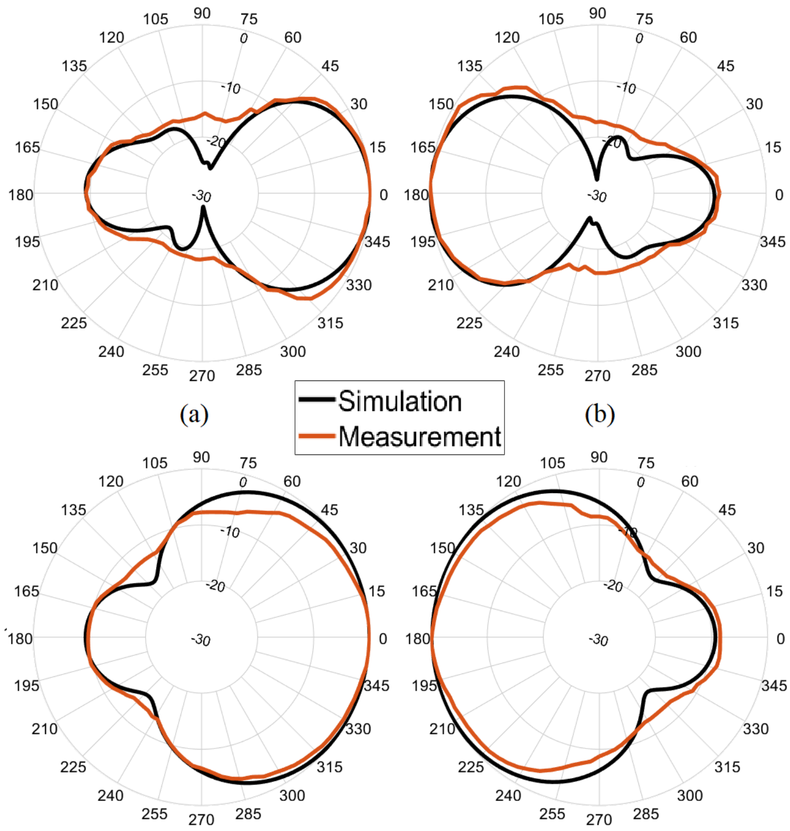

Figure 4.7. Normalized far-field graphs of the SB Vivaldi antenna at 2.45 GHz (a) State-1 $\phi = 90°$ (b) State-2 $\phi = 90°$ (c) State-1 $\phi = 0°$ (d) State-2 $\phi = 0°$: ©2023 IEEE (Karatay and Yaman, 2024a)

We manufactured the liquid holder with the help of a 3D printer. The far-field plots can be seen in Figure 4.7. The simulation yielded a maximum gain of 5.11 dBi, while the measured gain stood at 4.76 dBi. Due to the mirror symmetry, the simulated FBR for both states is equal and corresponds to 9.2 dB. The measured FBR values, 10.1 dB for State-1 and 9 dB for State-2, indicate a good agreement between the measurements and simulations. We employed a thin tape, characterized by a low dielectric constant and a thickness of 100 μm, in order to ensure that gallium does not leak when the antenna is positioned sideways during the anechoic chamber measurements.

Modifications to the fabricated antenna were intended to improve maximum gain and FBR. For this purpose, cones with a greater radius of 9.16 cm and a smaller radius of 3.88 cm were attached to both sides of the antenna, and the planar Vivaldi antenna was turned into a Vivaldi-fed horn structure. The dielectric cones were covered with conductive tape and had a focusing feature. After this process, the operating frequency of the antenna remained at approximately 2.45 GHz; see Figure 4.9, while we found the maximum gain value to be 10.9 dBi in the simulation, and the FBR was $\sim$ 15 dB. The gain values were measured in the anechoic chamber as 9.9 dBi and 9.6 dBi for State-1 and State-2, respectively. The FBR values were 14.5 dB and 15.4 dB for the same cases. This process has shown us that even if the antenna has a bulky structure, it is easily possible to rotate the antenna's main lobe 180 degrees thanks to the LM displacement.

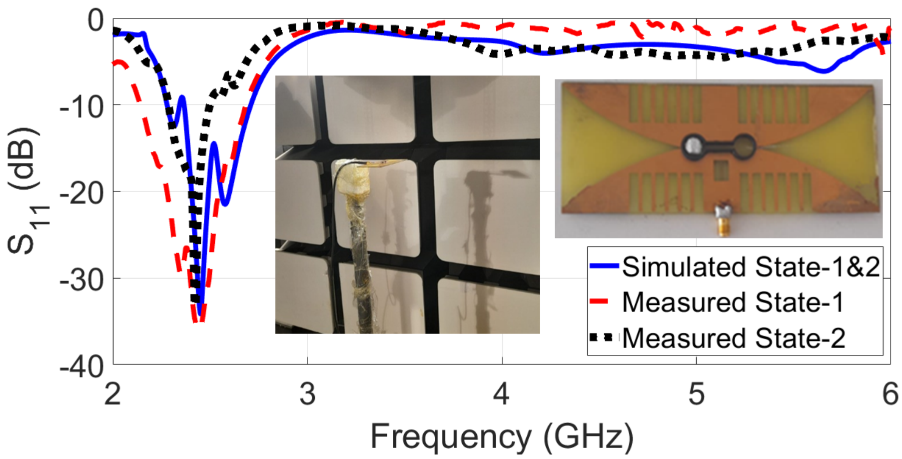

Figure 4.8. Simulated and measured S-parameters of the SB back-to-back Vivaldi antenna with various states: ©2023 IEEE (Karatay and Yaman, 2024a)

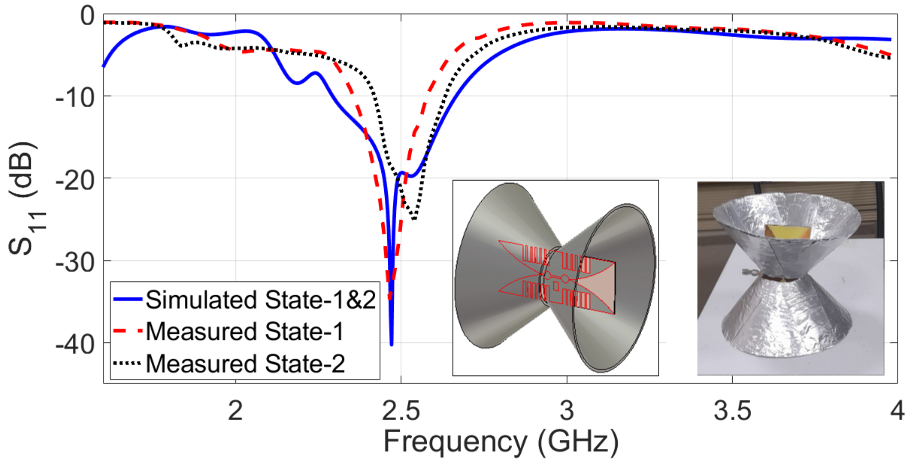

Figure 4.9. Simulated and measured S-parameters of the SB Vivaldi-fed horn antenna

4.2. Dual-Band Vivaldi Antenna

In the previous section, we discussed the design, fabrication, and measurement processes of an SB-Vivaldi antenna array operating in the 2.45 GHz frequency band. In this section, we introduced some modifications to the structure of the antenna, allowing it to operate both at 2.45 GHz and at 5.8 GHz. While the main target is still getting the reflection coefficients down to the required levels at both frequencies, there is another more critical point: the antenna must offer sufficient gain for a Doppler radar application, and the proposed beam-switching feature is to be applicable at both frequencies.

4.2.1. Dual-Band Vivaldi Antenna Design

The minor modifications applied to both the dimensions and configuration of the antenna did not lead to inefficacies with its implementation at both 2.45 GHz and 5.8 GHz. The FR-4 substrate of 1.5 mm thickness was used, corresponding to the preceding design's use.

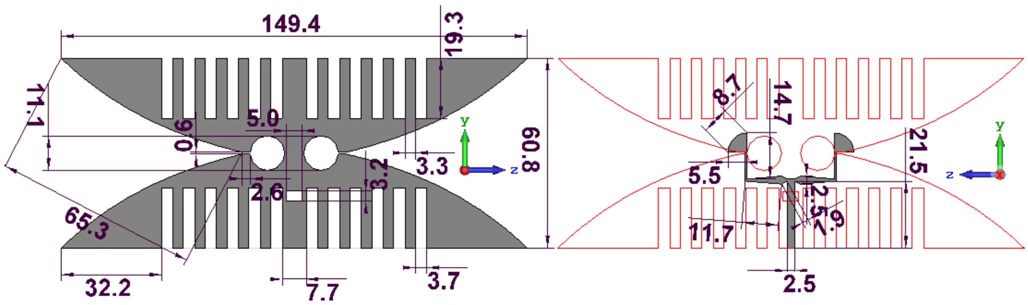

Figure 4.10. DB Vivaldi antenna dimensions in mm: ©2023 IEEE (Karatay and Yaman, 2024a)

As given in Figure 4.10, the dimensions of the DGS structure were reduced, and the dimensions of the slots were increased, allowing the antenna to extend its single operating frequency from 2.45 GHz to include 5.8 GHz within the simulation range. Figure 4.11 shows that the cavity of the antenna is filled in the manner shown to achieve the radiation patterns. In this manner, CST simulations were conducted at both frequencies for State-1 by exclusively filling the cavity with LM, as depicted in Figure 4.11-(a). At 2.45 GHz, the state-changing feature is observed when the slot line is not filled with LM.

However, the main lobe directions deviate from the prescribed directions, hence poor back lobe suppression at 5.8 GHz. In this configuration, as shown in Figure 4.11-(b), LM is introduced into the slot line, and the simulations are repeated. At 5.8 GHz, the desired radiation direction and a satisfactory FBR level are established in this configuration.

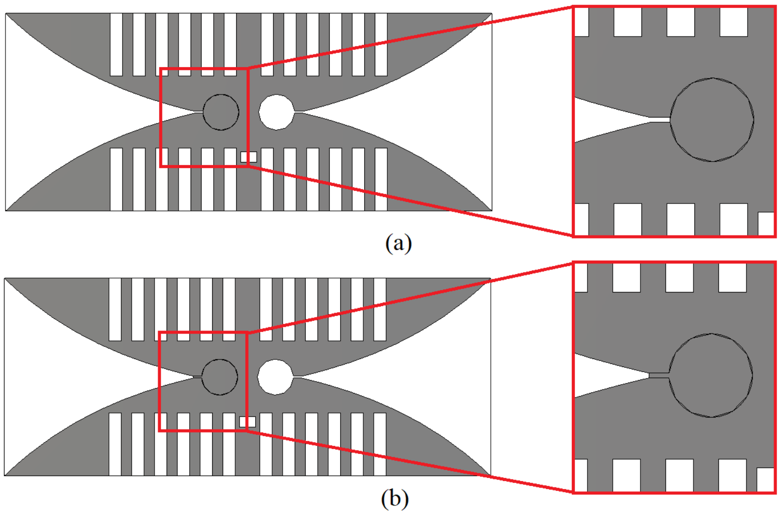

Figure 4.11. Simulation scenarios of LM-assisted beam-switching at both 2.45 GHz and 5.8 GHz for DB Vivaldi antenna. State-1 when (a) LM was exclusively filled in the cavity (b) both the cavity and slot line were filled with LM: ©2023 IEEE (Karatay and Yaman, 2024a)

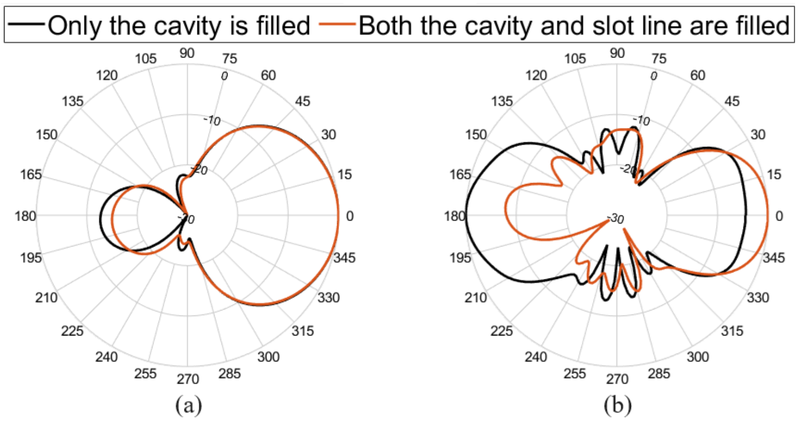

Figure 4.12. Effect of filling the slot line on the far-field plot at State-1 when $\phi = 90°$ (a) 2.45 GHz (b) 5.8 GHz: ©2023 IEEE (Karatay and Yaman, 2024a)

In Figure 4.12, only one state (State-1) and a single plane ($\phi = 90°$) are displayed, resulting in four graphs for the two different frequencies due to the simulation results for State-2, having mirror symmetry with State-1.

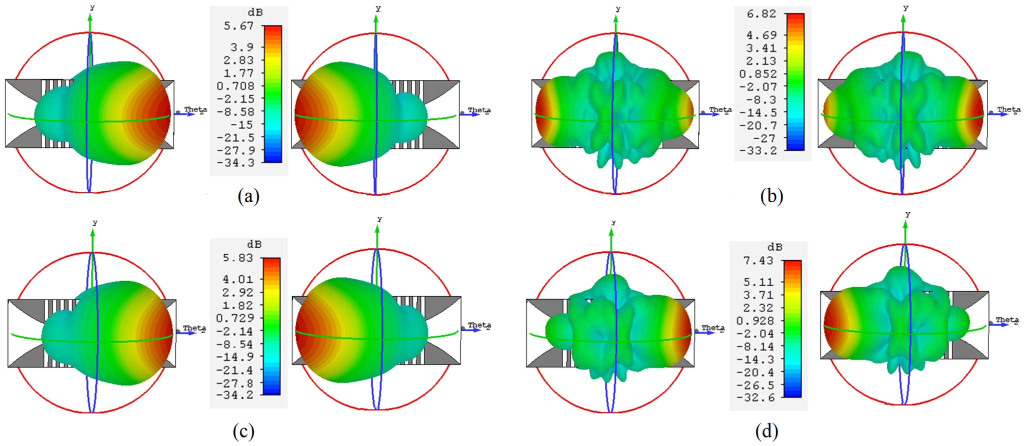

Figure 4.13. Various states of the LM displacement-enabled DB Vivaldi antenna (The patterns on the left represent State-1, while the patterns on the right represent State-2.) Radiation pattern at (a) 2.45 GHz when only the cavity has LM (b) at 5.8 GHz when only the cavity has LM (c) at 2.45 GHz when both the cavity and slot line are filled (d) at 5.8 GHz when both the cavity and slot line are filled

For better clarity in observing its behavior along other axes, 3D radiation pattern results for these two scenarios are also presented. Figure 4.13-(a) and 4.13-(b) portray the radiation pattern results for 2.45 GHz and 5.8 GHz, respectively, for this scenario. On the left side, State-1 is shown, with State-2 on the right side. This state is free of any problem at 2.45 GHz. However, in the scenario under consideration, at 5.8 GHz, the main lobe directions have been reoriented in the antithetical direction to the prescribed directions, leading to a highly inadequate suppression of back lobes. The slot line in this configuration, with a slight enhancement in the magnitude of the main lobe, observed at 2.45 GHz, shows an improvement with respect to back lobe suppression, as depicted in Figure 4.13-(c). Figure 4.13-(d) becomes obvious as far as 5.8 GHz is concerned.

Understanding and defining tolerances to overcome possible problems or critical assumptions that could be raised in the production process affecting the experimental outcomes is the most important fact. It is essential to clarify the effect of variations of the dielectric constant on S_{11} due to the variability of the dielectric constant of the FR-4 substrate by the manufacturer-to-manufacturer, as well as its dependence on temperature and frequency. As shown in Figure 4.14, the impact of the dielectric constant on S_{11} is illustrated by showing increments of 0.1 in the x-axis and going from 4.1 to 4.5. Such a change in the dielectric constant affects the operating frequency at about 2.45 GHz by approximately 80 MHz and at around 5.8 GHz by around 250 MHz.

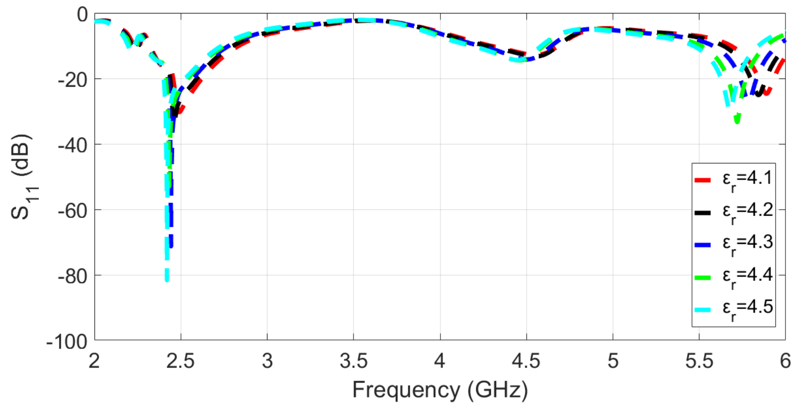

Figure 4.14. Effect of the dielectric constant of the substrate on S_{11} of DB Vivaldi antenna

Another exploration of this part pertains to the dimensions of the region referred to as the slot line, as shown in Figure 4.11. With the relevant region having a thickness of 0.62 mm and a length of 2.6 mm, even micrometric deviations that may be produced during manufacturing become quite significant due to proportional changes in the dimensions. In this sense, attention must be given to determining tolerances for these two parameters. As shown in Figure 4.15, the change in S_{11} cannot be said when the width of the slot line moves from 0.52 mm to 0.92 mm. It can be found that no change occurs at the operating frequency, but variations occur in the reflection coefficient at the working frequency. However, in all the scenarios, reflection coefficient values remain below -20 dB for both frequencies.

Lastly, it has been studied how long the slot line length would affect the same parameter; see Figure 4.16. It is important to note that the region referred to as the slot line is directly connected to the cavity of the Vivaldi and must be filled with LM. All the simulated investigations were done in the State-1 scenario, where only the left cavity and the corresponding slot line were filled with LM, and their results were obtained. Due to mirror symmetry, the simulation results will be the same in State-2, too.

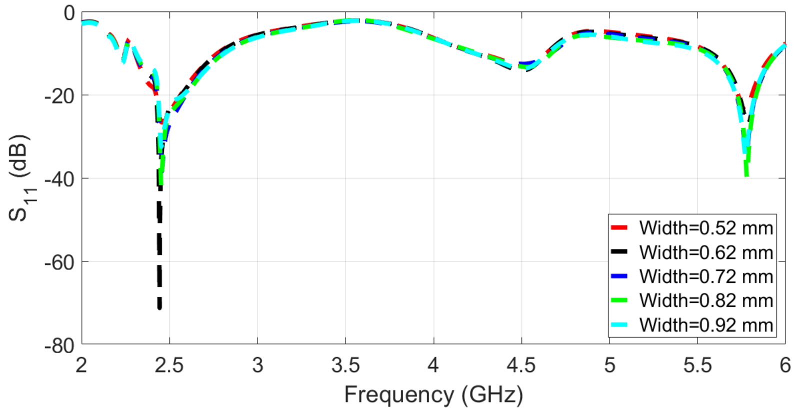

Figure 4.15. Effect of the slot line width on S_{11} of DB Vivaldi antenna

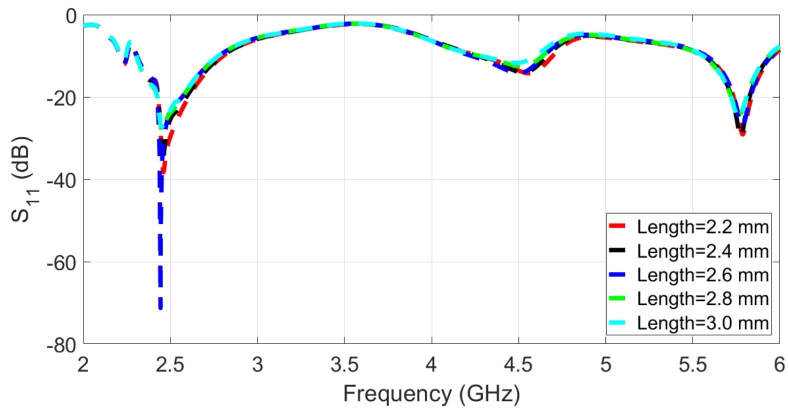

Figure 4.16. Effect of the slot line length on S_{11} of DB Vivaldi antenna

4.2.2. Dual-Band Vivaldi Antenna Results

A transmitter (Tx) and a receiver (Rx), designed for Doppler radar applications, underwent production and subsequent fundamental measurements. Both measured and simulated results reveal that the antennas exhibit suitably low reflection coefficients at both frequencies, as shown in Figure 4.17. The lower subfigure of Figure 4.17 shows the Rx ground surface when the antenna is in State-2, featuring mounts designed to prevent gallium leakage. The simulated maximum gain at 2.45 GHz is 5.83 dBi, with measured realized gains of 5 and 5.2 dBi for Tx and Rx, respectively. At 5.8 GHz, the simulated and measured realized gains for Tx and Rx are 7.43, 6.7, and 6.9 dBi.

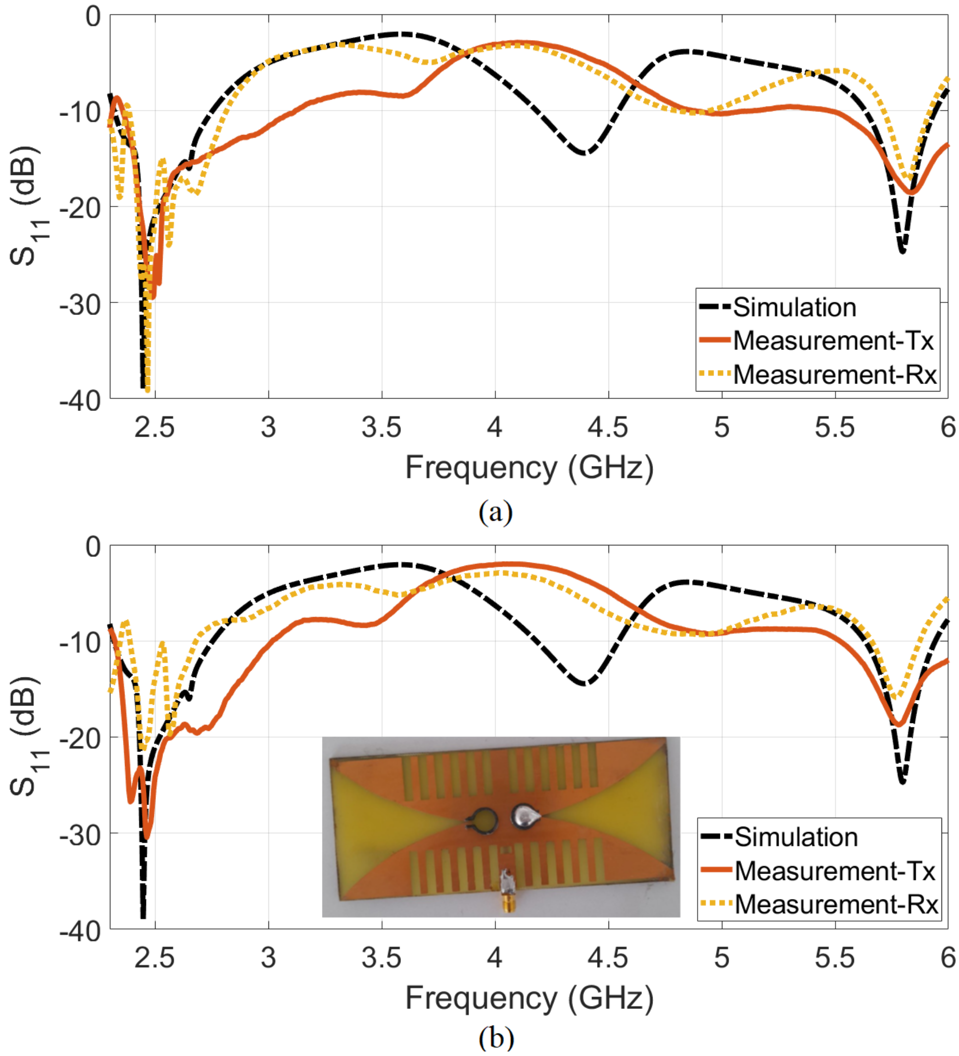

Figure 4.17. S-parameters of the DB Vivaldi antennas (a) State-1 (b) State-2: ©2023 IEEE (Karatay and Yaman, 2024a)

The FBR at 2.45 GHz in CST-MWS for both states is 15 dB. Practical measurements of the maximum FBRs are around 12 dB for State-1 of Tx, about 11 dB for State-2 of Tx, around 12 dB for State-1 of Rx, and approximately 13 dB for State-2 of Rx. The pattern measurement is precisely confirmed by this close alignment in Figure 4.18. Although there is a slight reduction in these values at 5.8 GHz, the FBR for both states of the antennas remains consistently above 8 dB in both simulated and measured scenarios, as seen in Figure 4.19, thereby confirming the suitability of such antennas for the intended application.

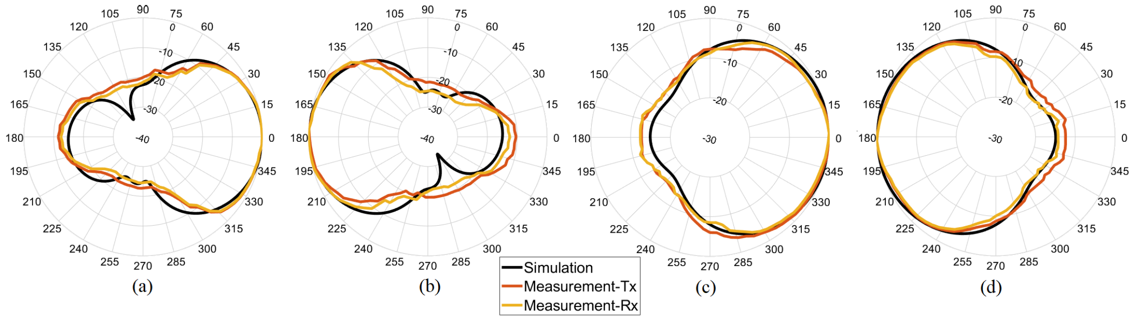

Figure 4.18. At 2.45 GHz: Normalized far-field graphs of the DB Vivaldi antennas (a) State-1 - $\phi = 90°$ (b) State-2 - $\phi = 90°$ (c) State-1 - $\phi = 0°$ (d) State-2 - $\phi = 0°$: ©2023 IEEE (Karatay and Yaman, 2024a)

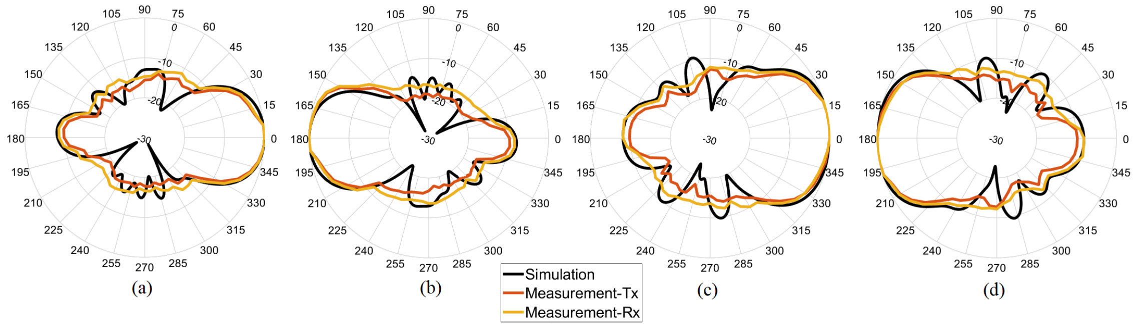

Figure 4.19. At 5.8 GHz: Normalized far-field graphs of the DB Vivaldi antennas (a) State-1 - $\phi = 90°$ (b) State-2 - $\phi = 90°$ (c) State-1 - $\phi = 0°$ (d) State-2 - $\phi = 0°$: ©2023 IEEE (Karatay and Yaman, 2024a)

4.2.3. Comparison

This section presents a comparison between the proposed antenna structure and various pattern-reconfigurable antennas selected from existing literature. Fundamentally, the chosen counterparts from the literature rely on the electrical way for reconfiguration. This, therefore, makes it easier to compare the advantages and disadvantages of the LM-based method with those of electrical methods. Table 4.1 gives a comparative view of the existing pattern-reconfigurable antennas in the literature. The proposed antenna exhibits a smaller electrical size at a lower frequency compared to those of its counterparts. The values in each of the gain and FBR rows are presented at two frequencies: the first corresponding to 2.45 GHz, and the second, 5.8 GHz. The seamless and cost-effective integration in the proposed configuration is indeed a significant strength. Moreover, as a result of self-sufficiency without electrical connections, there is less risk of interference-induced pattern degradation. In contrast to configurations relying on PIN diodes and a discontinuous TL, the proposed strategy is more efficient with its continuous surface current. Besides, while a reconfigurable, malfunctioning structure based on discontinuous TLs and the need for periodic maintenance for electromechanical or optical reconfiguration techniques may be a long-term and robust solution, the LM displacement-based beam switching approach provides a more cost-effective and user-friendly option.

Table 4.1. Comparison of various pattern reconfigurable antennas: ©2023 IEEE (Karatay and Yaman, 2024a)

	This work	(Fan et al.,2019)	(Jin et al.,2018)	(Wu et al.,2018)
Method	LM	Graphene	Diode	Graphene
Size ($\lambda^2{}_{2.45}$)	1.2×0.5	3.2×1.4	0.6×0.6	3×0.4
Gain (dBi)	5.2 / 6.9	3.8	4.1	3.1
FBR (dB)	13 / 9.5	~ 8	~ 8	~ 10
Complexity	Low	Moderate	Moderate	High
Bias	✗	✗	✓	✗

4.3. Liquid Metal-Assisted T-Junction Power Divider

In an MIT-CCDR configuration, one of the critical components in radar is the PD, and the PD's operating frequency must be in accord with other radar components. In the current configuration, half of the power is directed to the transmitter antenna, while the other half is supplied to the mixer as a local oscillator. Since the antennas are designed to operate in DB configurations, and the radar is intermittently operated at both 2.45 GHz and 5.8 GHz, it is crucial for the PD to function seamlessly at both frequencies. In this case, the design, fabrication, and measurements of a PD capable of switching frequencies between these two frequencies will be presented in this section.

4.3.1. Power Divider Design

A PD with a T-junction configuration has been designed using FR-4 material. The input port of the PD has been adjusted to possess a $50\ \Omega$ impedance, and it is equally split into two output ports with a 1:1 ratio. The impedance of the divider matches the characteristic impedance of the input line (Z_0 in Figure 4.20). Thus, the value of Z_1 should be $100\ \Omega$ as given:

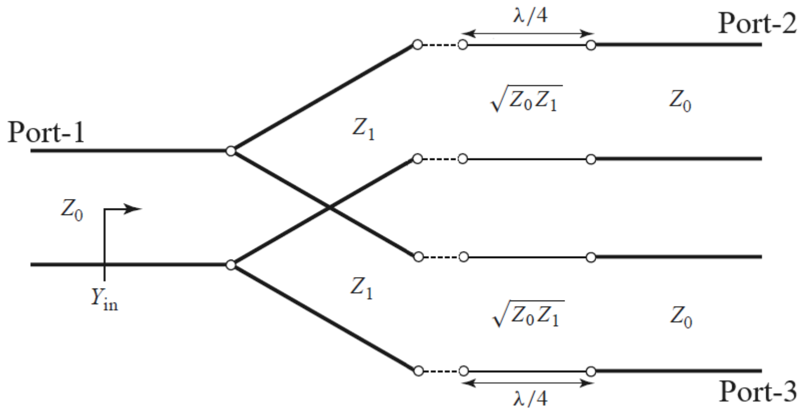

Figure 4.20. TL equivalent of the T-Junction PD: ©2023 IEEE (Karatay and Yaman, 2024a)

$$Y_{in} = \frac{1}{Z_0} = \frac{1}{Z_1} + \frac{1}{Z_1} \tag{4.1}$$

In order to terminate the output ports with $50\ \Omega$ impedance, a quarter wave (QW) transformer must be inserted. The impedance of the QW transformer is approximately $70\ \Omega$, and the related equation is given below:

$$Z_{qw} = \sqrt{Z_1 Z_0} \tag{4.2}$$

The PD exhibits a frequency-selective characteristic by which the transformer length is set to a quarter of the wavelength. Leveraging this feature provides opportunities for transitions between 2.45 GHz and 5.8 GHz. Alteration of the transformer's length is done to allow for flexibility in switching frequency, thus resulting in a reduction in operating frequency when increasing the length of the transformer and vice versa. The intention here is to ensure the PD with the ability to switch between the other variable frequencies. Two states, namely State-A and State-B, have been defined herein, and the schematic representation is shown in Figure 4.21 illustrating the areas for LM filling. By filling spaces A and B, the structure is optimized for operation at 2.45 GHz and 5.8 GHz, respectively. LM filling in region A brings the QW transformer line into alignment with the effective wavelength of 2.45 GHz, while LM filling in region B results in the alignment of the same line with a quarter of the effective wavelength at 5.8 GHz.

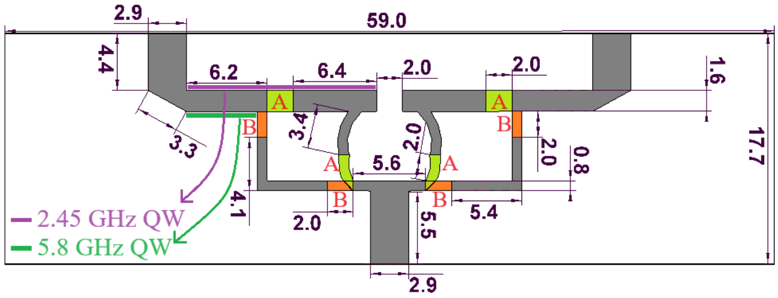

Figure 4.21. The LM-based PD dimensions in mm: ©2023 IEEE (Karatay and Yaman, 2024a)

4.3.2. Power Divider Results

The PD was subsequently fabricated for deployment in the MIT-CCDR configuration and investigated to monitor reflection and transmission. State-A and State-B refer to the PD states corresponding to 2.45 GHz and 5.8 GHz, respectively. As shown in Figure 4.22, S_{11} has a significant reduction in both simulation and measurement at about 2.45 GHz in State-A. At the same time, in State-B, the same plot has its minimum point around 5.8 GHz. That indicates the frequency-switching capability of the LM-assisted PD, a key advantage in the potential of the radar to mitigate noise at frequencies beyond the operational range of the radar.

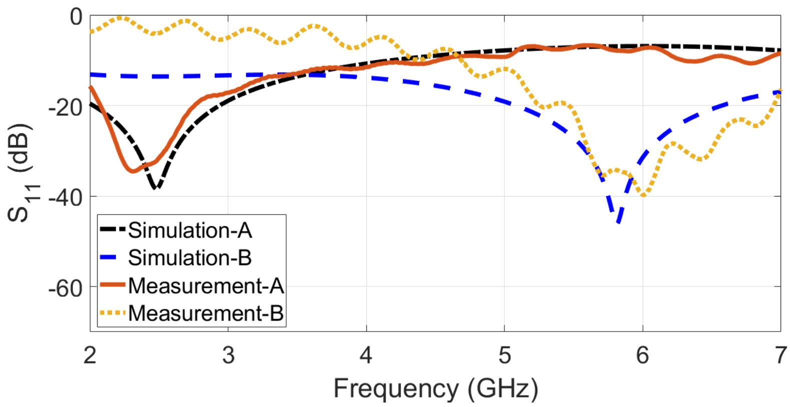

Figure 4.22. S_{11} of the PD: ©2023 IEEE (Karatay and Yaman, 2024a)

Figure 4.23 shows the power ratios transmitted to the second and third ports. In State-A, the transmission value increases at the frequency of 2.45 GHz, and in State-B, there are higher transmission values at 5.8 GHz. On the bottom side of Figure 4.23, a photo of the PD with the corresponding port numbers is given. It illustrates how, in State-B, polyurethane has been utilized for the liquid channel.

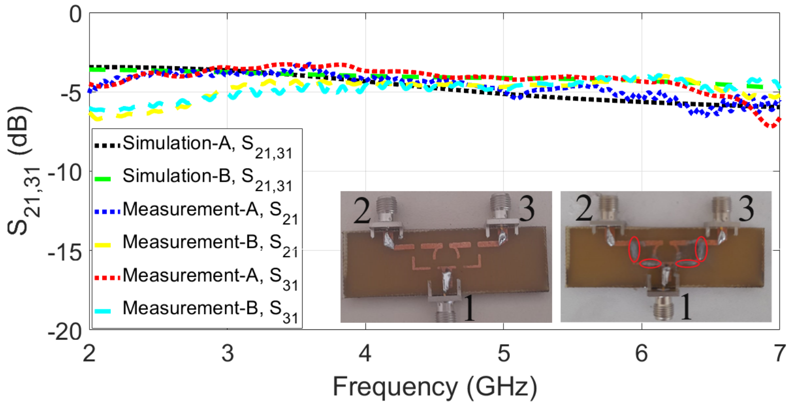

Figure 4.23. S_{21} and S_{31} of the PD: ©2023 IEEE (Karatay and Yaman, 2024a)

4.4. Doppler Radar Results

After manufacturing the components and incorporating switchable features, the produced structures were integrated into an operational Doppler radar system featuring continuous wave operation.

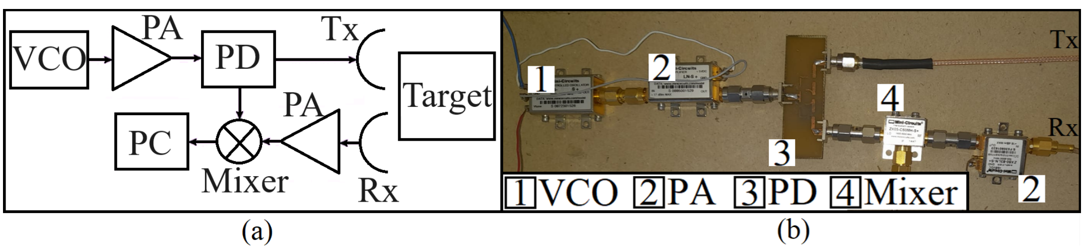

Figure 4.24. Block diagram and the photo of the MIT-CCDR configuration (VCO: Voltage-controlled oscillator, PA: Power Amplifier, PD: Power divider) (a) Scheme (b) Photo: ©2023 IEEE (Karatay and Yaman, 2024a)

Figure 4.24 demonstrates a block diagram and a photo of the configuration, illustrating the reconfigurable Rx, Tx, and PD structures using LM. In this configuration, the input frequency is easily adjusted using the VCO. Radar functionality in either 2.45 GHz or 5.8 GHz for this configuration is enabled by the enablement of the radar for the PD to transition between State-A and State-B. Velocity measurements were taken in each state. Figure 4.24-(a) shows that with the antennas in State-1, the radar detects the right side. On the other side, when transitioning to State-2, the radar identifies the left side. A visual representation of syringe-assisted state change with the antennas integrated into the radar is presented in Figure 4.25.

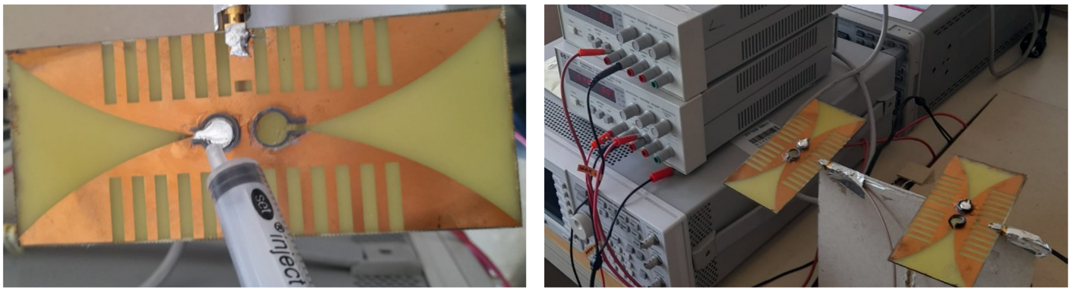

(a) (b)

Figure 4.25. Photos of the proposed radar (a) Reconfiguration of the antennas with LM displacement (b) Antennas integrated to the radar system: ©2023 IEEE (Karatay and Yaman, 2024a)

Within a specific measurement scenario depicted in Figure 4.26, the target continuously moves at the given position while the antenna states are dynamically adjusted using a syringe. Consecutive movements were performed in each scenario, and the measurements were systematically accomplished. The person started motion from a distance, then slowly accelerated towards the radar and stopped at the radar. Briefly waiting, then moving with acceleration and deceleration. The moving person performed identical movements at around the same speeds in all four measurement setups. Following observation with State-1, as observable in Figure 4.26-(a) and Figure 4.26-(c), where the radar successfully detects the moving person within its footprint at around 2.45 GHz, radar orientation in this state rotates by 180 degrees from its State-1 configuration. Hence, no movement signal in the current radar state of interest is connected with the target of interest. It agrees precisely with what was intended to be achieved. State-2 enables differentiation between two moving objects within the radar's range but in separate sectors in scenarios with periodic changes in radar states. In fact, this configuration is such that there are possibilities to differentiate between two moving objects when some are close enough to the radar through this adaptive configuration. Second, when multiple moving objects exist in its range, this allows the radar to differentiate the speed of these moving objects. Additionally, this band is equipped with a frequency-switching capability, which allows for smooth transitions while in use, thus warding off any potential interference threats to the current band being used.

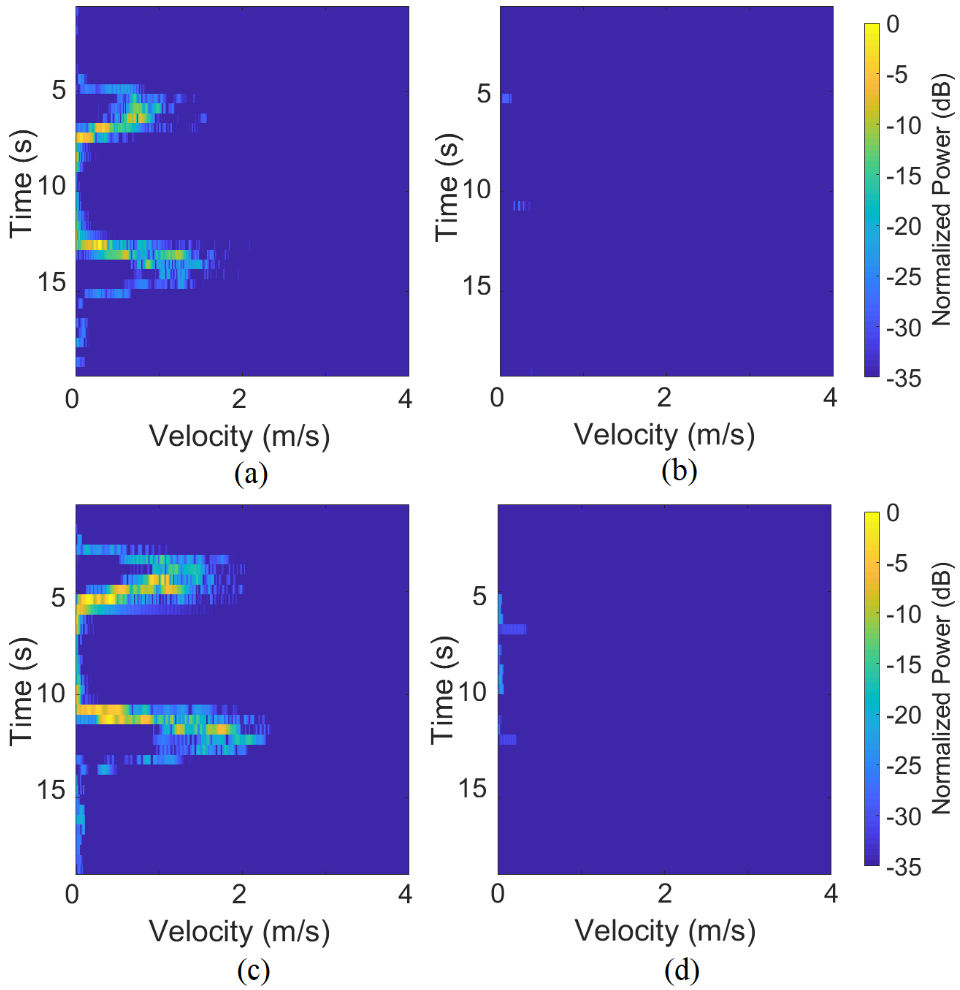

Figure 4.26. Velocity measurement of a walking person (a) State-A1 (b) State-A2 (c) State-B1 (d) State-B2: ©2023 IEEE (Karatay and Yaman, 2024a)

In Figure 4.27-(a) and Figure 4.27-(c), the radar sources were set in State-1, while an aluminum ball attached to a pendulum lies within the area, according to the arrangement as shown in Figure 4.24. Though the swinging ball may not exhibit uniform motion, both seem to be aligned. In contrast, in Figure 4.27-(b) and 4.27-(d), the radar beam is aimed at an area without the presence of any moving object; thus, there is no motion detection, much like is shown in Figure 4.26-(b) and 4.26-(d). However, the object on the right side of the radar keeps moving. Suppose the moving object is close enough. In that case, this backward detection is slightly more pronounced in the measurements taken at the higher frequency due to the lower FBR value of the DB Vivaldi antenna at 5.8 GHz compared to 2.45 GHz. When the pendulum swings in one direction, the walking man simultaneously moves in the opposite direction, given in Figure 4.28. The noise originating from the moving person was absent at all power levels due to the metallic nature of the pendulum, causing Doppler shifts across multiple frequencies simultaneously. On the other hand, in Figure 4.28-(b) and 4.28-(d), it was possible to quantify the velocity of the moving person approaching the radar. However, this was a result of the measured FBR values. Therefore, movements of the pendulum lingering in the back lobe, even at a low power level, were observed as noise in these measurements.

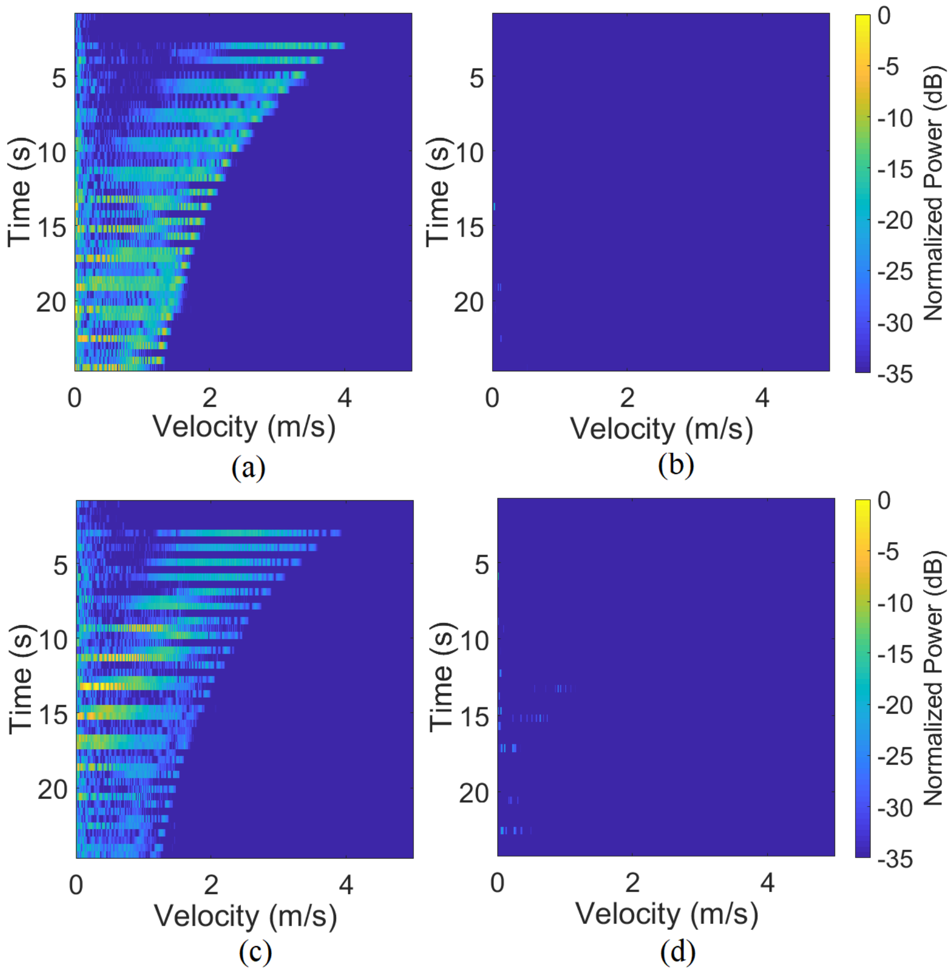

Figure 4.27. Velocity measurement of a pendulum (a) State-A1 (b) State-A2 (c) State-B1 (d) State-B2

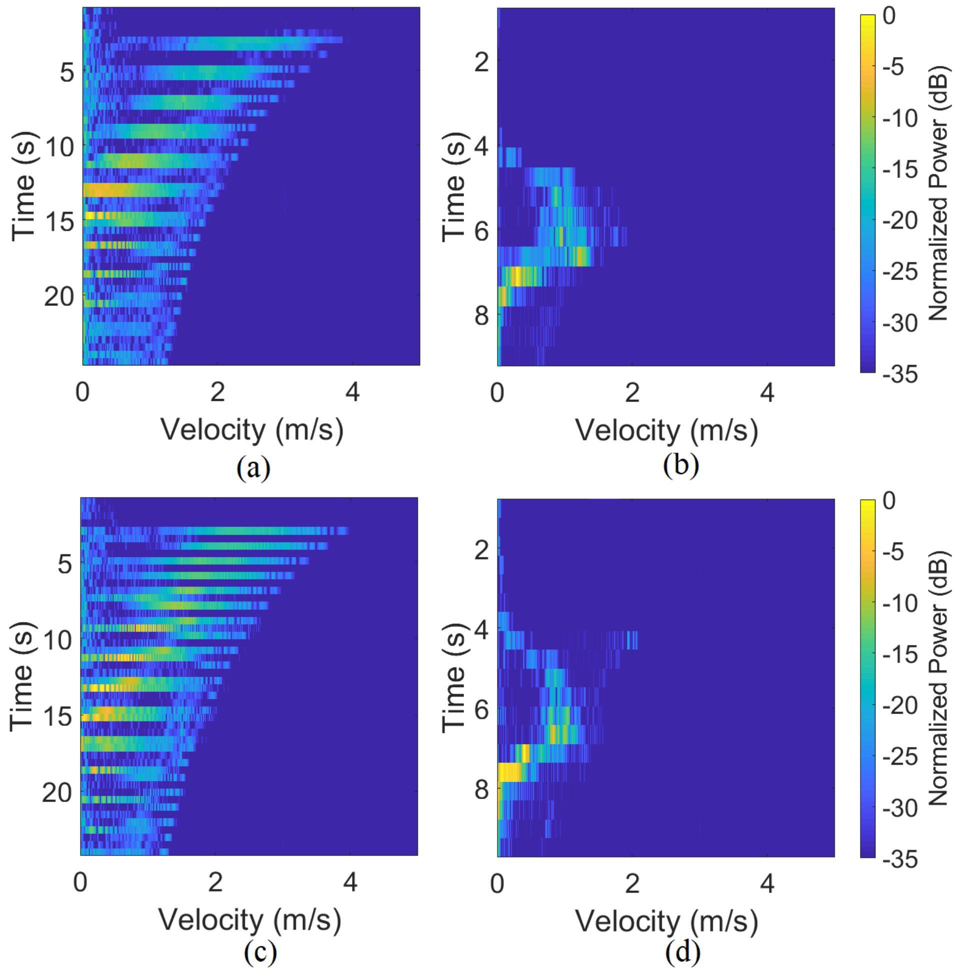

Figure 4.28. Velocity measurement of a pendulum and a walking person (a) State-A1 (b) State-A2 (c) State-B1 (d) State-B2: ©2023 IEEE (Karatay and Yaman, 2024a)

For visualization purposes, the experimental schematic of Figure 4.28 is shown in Figure 4.29. When the antennas are in State-1, since the electromagnetic power on the right side is much higher than on the left side, only the movement of the pendulum is observed at both frequencies, while the movement of the moving person cannot be observed. On the other hand, if the antennas switch to State-2, the main lobe direction is concentrated on the left side, and in this case, the main movement detected belongs to the moving person. In the measurement in Figure 4.27, the person on the left side is not present at all; only the pendulum on the right side swings during every four states. In this case, the antennas detect movement when they are in State-1 and do not detect any movement when they switch to State-2. In the experimental setup of Figure 4.26, the left side where the moving person in Figure 4.29 is located is left empty, and the moving person is on the right side where the pendulum is located in the same figure.

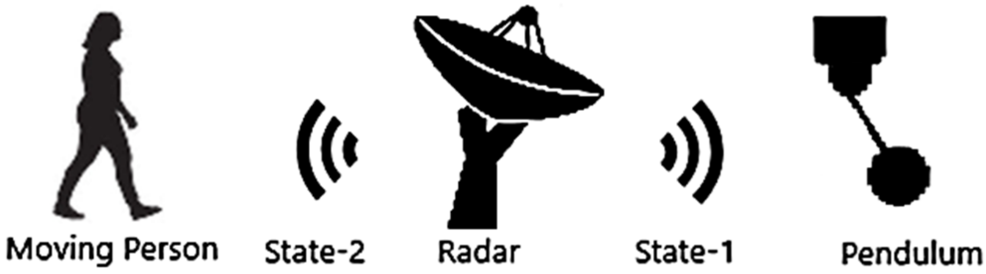

Figure 4.29. Schematic of the Doppler radar measurements

4.4.1. Comparison

In this subsection, a comparative analysis is made between the proposed Doppler radar and the selected MIT-CCDR-based structures in the literature. Parameters subject to comparison encompass operating frequencies, antenna types, radar footprint, noise immunity, pattern reconfiguration capability, frequency-switching capability, and the ability to detect multiple movements. Table 4.2 provides a comparison of the performance of the proposed radar system with various MIT-CCDR-based studies documented in the literature. Several studies have been conducted over the years to develop and improve the operational functionalities of the MIT-CCDR system. The MIT-CCDR design has thus far seen almost all the MIT-CCDR-based radars proposed in the literature as SB configuration; in this thesis, it has been shifted to a DB-capable system. The very remarkable milestone of this study is the feature of noise immunity enhancement through the displacement of LM, thereby ensuring improved immunity to noise. In contrast, the microstrip antenna structures of this configuration are used exclusively to reduce its weight, resulting in it being of enhanced practicality. Although prior studies in the literature have explored the incorporation of beam-switching capability into this configuration, our study marks a great achievement by realizing this capability through the LM-assisted technique. This novel approach mitigates the drawbacks associated with conventional electrical reconfiguration methods, especially when confronted with the challenge of detecting multiple moving targets.

Table 4.2. Comparison of various MIT-CCDR-based Doppler radars (CC: Coffee Can, MM: Metamaterial): ©2023 IEEE (Karatay and Yaman, 2024a)

	Proposed	(Charvat et al., 2012)	(Yılmaz and Yaman, 2019)
Freq. (GHz)	2.45 / 5.8	2.4	5.8
Type	MS	CC	MS+MM
Footprint (deg.)	120 / 60	75	60
Noise immun.	High	Low	Moderate
Beam-switching	✓	✗	✗
Freq. Switching	✓	✗	✗
Multi target	✓	✗	✗

4.5. Discussions

The presented radar competes with existing reconfiguration methods in conventional Doppler radar systems to improve many parameters in operational systems. First, a novel LM-based approach is used to reduce some of the existing challenges to traditional electrical, optical, and physical modifications. The results of the beam switching method are demonstrated first for an SB Vivaldi antenna, focusing on adaptability to a DB configuration and paving the way for usability across two different frequency bands. The study particularly emphasizes the advantages brought about by the LM structure against the discrete PIN diodes and highlights the continuous nature of LM as a critical feature in improving radiation efficiency. The continuous structure of LM allows for continuous shifting in the radar's angle by 180 degrees through a slight repositioning, which is a feat that would pose significant challenges with electrical methods. Integration of an LM-controlled PD for frequency switching in a radar system improves its practicality and robustness. Real-time changes of Doppler radar parameters, e.g., changing the main lobe direction and the frequency of operation of the divider, are achieved without any electrical or optical additions. While the manual dripping process has been used to demonstrate the effectiveness of the proposed technique, it is noted that it can be automated using liquid pumps in future studies. However, automatization with liquid pumps faces problems demanding careful control to avoid oscillations in the antenna and other components throughout measurements.

One possible limitation of this research is the manual dripping process and the high viscosity of gallium. Moreover, automating the process with liquid pumps would not only enhance efficiency but also address the issue of maintaining system stability. Future studies could be focused on developing and applying an automated system for the careful management of various pump options and meticulous monitoring to avoid oscillations or disturbances. Despite this limitation, the system demonstrates the ability to measure moving entities like walking people and pendulums with an equal measure of readability at both frequency bands. Besides, the system displays an ability to detect multiple target events without interfering with the movement in the blocked sector. In conclusion, the presented study opens new paths for further research and refinement, especially in the automation of the proposed technique and optimization of the viscosity of LM.

CHAPTER 5

SEPARATED MODE CAVITIES

In the previous chapter, a radar operating at 2.45 GHz and 5.8 GHz was presented. It is desired to convert the LM-controlled radar into a water-controlled form, but dielectric permittivity values must first be measured precisely. The new purpose is to develop a novel DB dielectric permittivity method for reconfiguring the proposed radar. First, the initial focus must be on designing a cavity operating at these two frequencies without any intermediate modes. This design aims to enhance measurement precision as it operates solely at these two frequencies. In this chapter, the results of studying the design of such a cavity with the first mode at 2.45 GHz and the second mode at 5.8 GHz are presented. The maximum achievable ratio of conventional rectangular and cylindrical cavities within the first two modes was analytically calculated using Lagrange multipliers. Further, analytical results were validated on whether the second mode can be placed at 5.8 GHz while the first mode is at 2.45 GHz. Numerical methods confirmed the above analytical results. Hence, the next attempt was to explore ways of exceeding this limit, and in the end, the design of a cavity with the first two modes located at 2.45 GHz and 5.8 GHz was eventually completed. In the article (Karatay and Yaman, 2024b), the results described above were published.

5.1. Analytical Calculations for Mode Separation Limits

This section analyzes the maximum ratio between the initial two modes of the conventional rectangular and cylindrical cavities. The subsection on rectangular cavities is then followed by an analysis of cylindrical cavities.

5.1.1. Analytical Calculations for Rectangular Cavities

The resonant frequency of any mode of a rectangular cavity can be calculated as:

$$f_{mnp} = \frac{c}{2\pi\sqrt{\varepsilon_r \mu_r}} \sqrt{\left(\frac{m\pi}{a}\right)^2 + \left(\frac{n\pi}{b}\right)^2 + \left(\frac{p\pi}{d}\right)^2} \tag{5.1}$$

where $b \leq a \leq d$. The dominant mode of a rectangular cavity is the TE_{101} mode since at least two of the integer values m, n, and p must be non-zero. When the cavity is hollow ($\varepsilon_r, \mu_r = 1$), the resonant frequency of the TE_{101} mode can be expressed as follows.

$$f_{101} = \frac{c}{2}\sqrt{\left(\frac{1}{a}\right)^2 + \left(\frac{1}{d}\right)^2} \tag{5.2}$$

The possible second modes in a rectangular cavity are TE_{011} or TE_{102} whose resonant frequencies can be calculated as:

$$f_{011} = \frac{c}{2}\sqrt{\left(\frac{1}{b}\right)^2 + \left(\frac{1}{d}\right)^2} \tag{5.3}$$

$$f_{102} = \frac{c}{2}\sqrt{\left(\frac{1}{a}\right)^2 + \left(\frac{2}{d}\right)^2} \tag{5.4}$$

We will determine the maximum ratio between the resonant frequency of the second mode and that of the first mode.

$$max\left\{\frac{min\{f_{011},\ f_{102}\}}{f_{101}}\right\},\ b \leq\ a \leq d \tag{5.5}$$

It is imperative to ascertain whether the second mode corresponds to TE_{011} or TE_{102}. The determination is based on identifying the mode with the lower frequency, denoted as f_{011} and f_{102}. Consequently, our analysis must encompass scenarios where either f_{011} or f_{102} is smaller than the other.

$$f_{011} \lesseqgtr f_{102} \tag{5.6}$$

$$\left(\frac{1}{b}\right)^2 + \left(\frac{1}{d}\right)^2 \lesseqgtr \left(\frac{1}{a}\right)^2 + \left(\frac{2}{d}\right)^2 \tag{5.7}$$

$$\frac{1}{b^2} - \frac{1}{a^2} - \frac{3}{d^2} \lesseqgtr 0 \tag{5.8}$$

If $\frac{1}{b^2} - \frac{1}{a^2} - \frac{3}{d^2}$ is less than or equal to zero, the second mode is TE_{011}, otherwise the second mode is TE_{102}.

5.1.1.1. Case-I

If $\frac{1}{b^2} - \frac{1}{a^2} - \frac{3}{d^2} \geq 0$, the second mode is TE_{102}. Our objective is to minimize $\left(\frac{f_{101}}{f_{102}}\right)^2$ under the constraints $\frac{1}{b^2} - \frac{1}{a^2} - \frac{3}{d^2} \geq 0$, $b - a \leq 0$, $a - d \leq 0$, $a, b, d > 0$. Square the multiplicative inverse of the function, as minimizing that yields the same result as maximizing the original function. Squaring the function helps eliminate the square root expression and simplifies the derivatives. Introducing three non-negative slack variables, denoted as s_1^2, s_2^2, and s_3^2, accommodates the constraints imposed by three inequality conditions.

$$Minimize\ g(\vec{r}) = \frac{\left(\frac{1}{a}\right)^2 + \left(\frac{1}{d}\right)^2}{\left(\frac{1}{a}\right)^2 + \left(\frac{2}{d}\right)^2} \tag{5.9}$$

$$Subject\ to\ h_1(\vec{r}, s_1) = \frac{1}{b^2} - \frac{1}{a^2} - \frac{3}{d^2} - s_1^2 = 0 \tag{5.10}$$

$$h_2(\vec{r}, s_2) = b - a + s_2^2 = 0 \tag{5.11}$$

$$h_3(\vec{r}, s_3) = a - d + s_3^2 = 0 \tag{5.12}$$

where $\vec{r} = [a\ b\ d]^T$. The Lagrangian function can be written as follows:

$$L(\vec{r}, \vec{\lambda}) = g(\vec{r}) - \lambda_1 h_1(\vec{r}, s_1) - \lambda_2 h_2(\vec{r}, s_2) - \lambda_3 h_3(\vec{r}, s_3) \tag{5.13}$$

where $\vec{\lambda} = [\lambda_1\ \lambda_2\ \lambda_3]^T$ is the Lagrange multiplier vector and $\nabla_{\vec{r},\vec{\lambda}} L = 0$.

$$\frac{\partial L}{\partial a} = \frac{-6ad^2}{(4a^2 + d^2)^2} - \frac{2\lambda_1 - \lambda_2 a^3 + \lambda_3 a^3}{a^3} = 0 \tag{5.14}$$

$$\frac{\partial L}{\partial b} = \frac{2\lambda_1 - \lambda_2 b^3}{b^3} = 0 \tag{5.15}$$

$$\frac{\partial L}{\partial d} = \frac{6a^2d}{(4a^2+d^2)^2} - \frac{6\lambda_1 - \lambda_3 d^3}{d^3} = 0 \tag{5.16}$$

$$\frac{\partial L}{\partial \lambda_1} = -\frac{1}{b^2} + \frac{1}{a^2} + \frac{3}{d^2} + s_1^2 = 0 \tag{5.17}$$

$$\frac{\partial L}{\partial \lambda_2} = -b + a - s_2^2 = 0 \tag{5.18}$$

$$\frac{\partial L}{\partial \lambda_3} = -a + d - s_3^2 = 0 \tag{5.19}$$

We can achieve the optimal solution by satisfying the complementary slackness condition (Winston et al., 2003). Complementary slackness is a basic principle in mathematical optimization, providing a way to validate the optimality of solutions in optimization problems (Hu and Kahng, 2016; Ebrahimnejad and Nasseri, 2009); Huang et al., 2015; Zhang and Dai, 2022). This principle states that if a constraint in a solution holds with equality, then the corresponding slack variable must be zero. Conversely, if the slack variable is non-zero, then its associated Lagrange multiplier must be zero. That way, the relation between the slack variables and Lagrange multipliers, as dictated by complementary slackness, allows establishing a mechanism for verifying the optimality of the solution (Huang et al., 2015; Zhang and Dai, 2022). Each inequality constraint of the problem presents two possible cases. Each inequality constraint, with three in the problem, gives 2^3 distinct conditions, so it is necessary to look at them all.

1. $s_1 = 0$, $s_2 = 0$, $s_3 = 0$, $\lambda_1 \neq 0$, $\lambda_2 \neq 0$, $\lambda_3 \neq 0$
   Equations 5.18 and 5.19 imply $a = b = d$. However, Equation 5.17 is not satisfied as q equals zero, and d must be greater than zero.

2. $s_1 \neq 0$, $s_2 \neq 0$, $s_3 \neq 0$, $\lambda_1 = 0$, $\lambda_2 = 0$, $\lambda_3 = 0$
   Equations 5.14 and 5.16 are not satisfied.

3. $s_1 \neq 0$, $s_2 = 0$, $s_3 = 0$, $\lambda_1 = 0$, $\lambda_2 \neq 0$, $\lambda_3 \neq 0$
   Equation 5.15 is not met.

4. $s_1 = 0$, $s_2 \neq 0$, $s_3 = 0$, $\lambda_1 \neq 0$, $\lambda_2 = 0$, $\lambda_3 \neq 0$
   Equation 5.15 is not met.

5. $s_1 = 0$, $s_2 = 0$, $s_3 \neq 0$, $\lambda_1 \neq 0$, $\lambda_2 \neq 0$, $\lambda_3 = 0$
   Equation 5.18 results in $a = b$. However, Equation 5.17 is not satisfied as $s_1 = 0$ and $d > 0$.

6. $s_1 = 0, s_2 \neq 0, s_3 \neq 0, \lambda_1 \neq 0, \lambda_2 = 0, \lambda_3 = 0$
   Equation 5.15 is not satisfied.

7. $s_1 \neq 0, s_2 = 0, s_3 \neq 0, \lambda_1 = 0, \lambda_2 \neq 0, \lambda_3 = 0$
   Equation 5.15 is not satisfied.

8. $s_1 \neq 0, s_2 \neq 0, s_3 = 0, \lambda_1 = 0, \lambda_2 = 0, \lambda_3 \neq 0$
   Solving Equation 5.19 yields $a = d$, and by applying Equation 5.17, we derive $b < (a/2)$. All remaining equations, including Equation 5.14 and 5.16 with the identical λ_3 value, are satisfiable under these circumstances. Consequently, the optimal solution for this scenario is characterized by $a = d > 2b$.

Choosing any value that fulfills the requirement $a = d > 2b$ for the function f_{102}/f_{101} yields a resulting value of $\sqrt{5/2}$.

5.1.1.2. Case-II

TE_{011} is the second mode, if the condition $\frac{1}{b^2} - \frac{1}{a^2} - \frac{3}{d^2} \leq 0$ holds. We also consider the equality condition in this scenario, wherein if $\frac{1}{b^2} - \frac{1}{a^2} - \frac{3}{d^2}$ equals zero, the second modes emerge as degenerate modes. The objective is to minimize $\left(\frac{f_{101}}{f_{011}}\right)^2$ under the constraints of $\frac{1}{b^2} - \frac{1}{a^2} - \frac{3}{d^2} \leq 0$, $b - a \leq 0$, $a - d \leq 0$ and $a, b, d > 0$.

$$Min.\ g(\vec{r}) = \frac{\left(\frac{1}{a}\right)^2 + \left(\frac{1}{d}\right)^2}{\left(\frac{1}{b}\right)^2 + \left(\frac{1}{d}\right)^2} \tag{5.20}$$

$$Subject\ to\ h_1(\vec{r}, s_1) = \frac{1}{b^2} - \frac{1}{a^2} - \frac{3}{d^2} + s_1^2 = 0 \tag{5.21}$$

$$h_2(\vec{r}, s_2) = b - a + s_2^2 = 0 \tag{5.22}$$

$$h_3(\vec{r}, s_3) = a - d + s_3^2 = 0 \tag{5.23}$$

$$\frac{\partial L}{\partial a} = \frac{-2}{a^3\left(\left(\frac{1}{b}\right)^2 + \left(\frac{1}{d}\right)^2\right)} - \frac{2\lambda_1 - \lambda_2 a^3 + \lambda_3 a^3}{a^3} = 0 \tag{5.24}$$

$$\frac{\partial L}{\partial b} = \frac{2bd^2\left(a^2 + d^2\right)}{a^2\left(b^2 + d^2\right)^2} + \frac{2\lambda_1 - \lambda_2 b^3}{b^3} = 0 \tag{5.25}$$

$$\frac{\partial L}{\partial d} = \frac{2b^2 d\left(b^2 - a^2\right)}{a^2\left(b^2 + d^2\right)^2} - \frac{6\lambda_1 - \lambda_3 d^3}{d^3} = 0 \tag{5.26}$$

$$\frac{\partial L}{\partial \lambda_1} = -\frac{1}{b^2} + \frac{1}{a^2} + \frac{3}{d^2} - s_1^2 = 0 \tag{5.27}$$

$$\frac{\partial L}{\partial \lambda_2} = -b + a - s_2^2 = 0 \tag{5.28}$$

$$\frac{\partial L}{\partial \lambda_3} = -a + d - s_3^2 = 0 \tag{5.29}$$

The following conditions will emerge:

1. $s_1 = 0,\ s_2 = 0,\ s_3 = 0,\ \lambda_1 \neq 0,\ \lambda_2 \neq 0,\ \lambda_3 \neq 0$
   From Equations 5.28 and 5.29, it follows that $a = b = d$. However, Equation 5.27 is not satisfied, since $q = 0$ and $d > 0$.

2. $s_1 \neq 0,\ s_2 \neq 0,\ s_3 \neq 0,\ \lambda_1 = 0,\ \lambda_2 = 0,\ \lambda_3 = 0$
   Neither Equations 5.24 nor 5.25 are satisfied. Note that $a \neq b$ from Equation 5.28, so also Equation 5.26 is not met in this case.

3. $s_1 \neq 0,\ s_2 = 0,\ s_3 = 0,\ \lambda_1 = 0,\ \lambda_2 \neq 0,\ \lambda_3 \neq 0$
   From Equations 5.28 and 5.29, it follows that $a = b = d$. However, Equation 5.26 is not satisfied since the first term and λ_1 are zero but $\lambda_3 \neq 0$.

4. $s_1 = 0,\ s_2 \neq 0,\ s_3 = 0,\ \lambda_1 \neq 0,\ \lambda_2 = 0,\ \lambda_3 \neq 0$
   Derived from Equations 5.27 and 5.29, it is evident that $a = d = 2b$. By isolating λ_1 in Equation 5.25 and representing a and d in relation to b, the value of λ_1 can be determined as $-(8b^2)/25$. In this configuration, λ_3 satisfies Equations 5.24 and 5.26 concurrently.

5. $s_1 = 0,\ s_2 = 0,\ s_3 \neq 0,\ \lambda_1 \neq 0,\ \lambda_2 \neq 0,\ \lambda_3 = 0$
   Equation 5.28 yields $a = b$. However, Equation 5.27 is not satisfied as $\lambda_1 \neq 0$.

6. $s_1 = 0,\ s_2 \neq 0,\ s_3 \neq 0,\ \lambda_1 \neq 0,\ \lambda_2 = 0,\ \lambda_3 = 0$
   Due to the values of λ_2 and λ_3 being zero, λ_1 must independently satisfy Equations 5.24, 5.25, and 5.26. From Equation 5.27, $(1/b^2) = (1/a^2) + (3/d^2)$. When substituted into Equations 5.24, 5.25 and 5.26, λ_1 is required to take distinct values for each equation, making this case incapable of yielding a feasible solution in the present scenario.

7. $s_1 \neq 0,\ s_2 = 0,\ s_3 \neq 0,\ \lambda_1 = 0,\ \lambda_2 \neq 0,\ \lambda_3 = 0$
   In accordance with Equations 5.28 and 5.29, it is asserted that $a = b < d$. The condition $a = b$ leads to the fulfillment of Equation 5.26. With $\lambda_1 = \lambda_3 = 0$, the value of λ_2 is required to meet both Equation 5.24 and Equation 5.25. A viable solution arises when λ_2 assumes the value of $(2d^2)/(a^3 + ad^2)$ under these conditions. Therefore, this scenario stands as an additional potential feasible solution.

8. $s_1 \neq 0,\ s_2 \neq 0,\ s_3 = 0,\ \lambda_1 = 0,\ \lambda_2 = 0,\ \lambda_3 \neq 0$
   Equation 5.25 is not met as $\lambda_1 = \lambda_2 = 0$ and $a, b, d > 0$.

Scenarios 4 and 7 satisfy all the equations above, with one representing the minimum point and the other the maximum point. Substituting the obtained values into the function f_{011}/f_{101}, we get a value in scenario 4 of $\sqrt{5/2} \approx 1.581$, in line with that given in Case-I. On the other hand, the frequency of the second mode in a rectangular cavity will not exceed approximately 1.581 times that of the dominant mode, so the sought maximum value corresponds to scenario 4. This establishes the limit for the distinguishability of the first two modes in a rectangular cavity.

5.1.2. Analytical Calculations for Cylindrical Cavities

The resonant frequency of a cylindrical empty cavity can be determined by using the following formula. In this context, r and l represent the radius and height of the cylindrical cavity, respectively.

$$f_{nmp} = \frac{c}{2\pi}\sqrt{\left(\frac{\chi_{nm}}{r}\right)^2 + \left(\frac{p\pi}{l}\right)^2} \tag{5.30}$$

The first mode of a cylindrical cavity can be either TE_{111} or TM_{010}, depending on the ratio of the cavity's diameter to its height. In the case where TE_{111} is the dominant mode, potential second modes include TE_{112} or TM_{010}. In the other scenario, possible second modes are TE_{111} or TM_{110}. The resonant frequencies for the TE_{111}, TM_{010}, TE_{112}, and TM_{110} modes can be computed using the following expressions.

$$f_{TE111} = \frac{c}{2\pi}\sqrt{\left(\frac{1.841}{r}\right)^2 + \left(\frac{\pi}{l}\right)^2} \tag{5.31}$$

$$f_{TM010} = \frac{2.405c}{2\pi r} \tag{5.32}$$

$$f_{TE112} = \frac{c}{2\pi}\sqrt{\left(\frac{1.841}{r}\right)^2 + \left(\frac{2\pi}{l}\right)^2} \tag{5.33}$$

$$f_{TM110} = \frac{3.832c}{2\pi r} \tag{5.34}$$

First, we need to find whether the dominant mode is TE_{111} or TM_{010}.

$$f_{TE111} \lesseqgtr f_{TM010} \tag{5.35}$$

$$\left(\frac{1.841}{r}\right)^2 + \left(\frac{\pi}{l}\right)^2 \lesseqgtr \left(\frac{2.405}{r}\right)^2 \tag{5.36}$$

$$\frac{-2.395}{r^2} + \frac{\pi^2}{l^2} \lesseqgtr 0 \tag{5.37}$$

Table 5.1. Values of χ_{nm} for TE and TM Modes of a Cylindrical Structure

n	$\chi_{n1}^{(TE)}$	$\chi_{n2}^{(TE)}$	$\chi_{n1}^{(TM)}$	$\chi_{n2}^{(TM)}$
0	3.832	7.016	2.405	5.520
1	1.841	5.331	3.832	7.016
2	3.054	6.706	5.135	8.417

The condition specified in Equation 5.37 determines the mode of a cylindrical cavity: TM_{010} if the expression is negative, and TE_{111} is dominant. The relative proportion of the height to the radius of the cavity determines this hierarchy in the cylindrical cavity. For TE_{111} to be dominant, the height of the cavity has to be large; that gives TE_{111} dominance. If the height is significantly reduced, the dominant mode of the cavity turns into TM_{010} mode. TE_{210} mode is not seen in a cylindrical cavity. On the other hand, it does not count even if the value of $\chi_{21}^{(TE)}$ in Table 5.1 is much smaller than $\chi_{11}^{(TM)}$, TE_{211} does not participate in the probabilities of the second mode. TM_{010} and TM_{110} is the only possible scenario from which the value, as mentioned earlier, of 3.832 falls out. This is possible only if the cavity's height is relatively small, thereby leaving out the TE_{211} mode as the second mode. This is because, due to the squared root of Equation 5.30, an inadequate cavity height increases the second term, making it unachievable for the TE_{211} mode to be the second mode.

The analysis assumes four different scenarios, which arise from two dominant mode cases and two corresponding second mode cases for each dominant mode. These scenarios are denoted with capital letters for the dominant modes and Roman numerals for the second modes, in consonance with that used for rectangular cavities.

5.1.2.1. Case-A

The dominant mode is TM_{010} if $\frac{-2.395}{r^2} + \frac{\pi^2}{l^2} \geq 0$.

$$max \left\{ \frac{min\{f_{TE111},\ f_{TM110}\}}{f_{TM010}} \right\} \tag{5.38}$$

First, we need to determine whether the second mode is TE_{111} or TM_{110}.

$$f_{TM110} \lesseqgtr f_{TE111} \tag{5.39}$$

$$\left(\frac{3.832}{r}\right)^2 \lesseqgtr \left(\frac{1.841}{r}\right)^2 + \left(\frac{\pi}{l}\right)^2 \tag{5.40}$$

$$\frac{11.295}{r^2} - \frac{\pi^2}{l^2} \lesseqgtr 0 \tag{5.41}$$

The second mode in Case A is TE_{111} if the expression in Equation 5.41 is greater than or equal to zero. Otherwise, it is TM_{110}.

5.1.2.2. Case-A-I

If $\frac{-2.395}{r^2} + \frac{\pi^2}{l^2} \geq 0$ and $\frac{11.295}{r^2} - \frac{\pi^2}{l^2} \geq 0$, the dominant mode is TM_{010} and the second mode is TE_{111}. Since there are two inequality constraints in this case, two slack variables, s_1^2 and s_2^2, will be sufficient.

$$Minimize\ g(\vec{\phi}) = \frac{\left(\frac{2.405}{r}\right)^2}{\left(\frac{1.841}{r}\right)^2 + \left(\frac{\pi}{l}\right)^2} \tag{5.42}$$

$$Subject\ to\ h_1(\vec{\phi}, s_1) = \frac{-2.395}{r^2} + \frac{\pi^2}{l^2} - q^2 = 0 \tag{5.43}$$

$$h_2(\vec{\phi}, s_2) = \frac{11.295}{r^2} - \frac{\pi^2}{l^2} - s^2 = 0 \tag{5.44}$$

where $\vec{\phi} = [r\ l]^T$ and $r,\ l > 0$.

$$L(\vec{\phi}, \vec{\lambda}) = g(\vec{\phi}) - \lambda_1 h_1(\vec{\phi}, s_1) - \lambda_2 h_2(\vec{\phi}, s_2) \tag{5.45}$$

The gradient of the Lagrange function must be zero.

$$\frac{\partial L}{\partial r} = \frac{-9.94 l^2 r}{(l^2 + 2.912 r^2)^2} - \frac{4.79\lambda_1 - 22.59\lambda_2}{r^3} = 0 \tag{5.46}$$

$$\frac{\partial L}{\partial l} = \frac{9.94 l r^2}{(l^2 + 2.912 r^2)^2} + \frac{2\pi^2 (\lambda_1 - \lambda_2)}{l^3} = 0 \tag{5.47}$$

$$\frac{\partial L}{\partial \lambda_1} = \frac{2.395}{r^2} - \frac{\pi^2}{l^2} + s_1^2 = 0 \tag{5.48}$$

$$\frac{\partial L}{\partial \lambda_2} = \frac{-11.295}{r^2} + \frac{\pi^2}{l^2} + s_2^2 = 0 \tag{5.49}$$

In this case, for two inequality constraints, four distinct subcases must be examined.

1. $s_1 = 0,\ s_2 = 0,\ \lambda_1 \neq 0,\ \lambda_2 \neq 0$
   Since $q = 0$ and $s = 0$, the value of r^2 obtained from Equations 5.48 and 5.49 are not the same, thus indicating that this condition is not met.

2. $s_1 \neq 0,\ s_2 \neq 0,\ \lambda_1 = 0,\ \lambda_2 = 0$
   The criteria set forth in Equations 5.46 and 5.47 are not satisfied as $\lambda_1 = 0$, $\lambda_2 = 0$, and both r and l are greater than zero.

3. $s_1 \neq 0,\ s_2 = 0,\ \lambda_1 = 0,\ \lambda_2 \neq 0$
   r is approximately equal to $1.07l$ from 5.49. Upon incorporating this result into Equations 5.46 and 5.47, all equations are met.

4. $s_1 = 0,\ s_2 \neq 0,\ \lambda_1 \neq 0,\ \lambda_2 = 0$
   The value of r is approximately $0.4926l$ from 5.48. With substitution of this value into Equations 5.46 and 5.47, all equations are satisfied.

Substituting the values derived from conditions 3 and 4 into the function f_{TE111}/f_{TM010} reveals that the ratio between these two values can vary from a minimum of 1 (as dictated by condition 4) to a maximum of approximately 1.593 (as dictated by condition 3). Consequently, the optimal solution for this case aligns with condition 3.

5.1.2.3. Case-A-II

If $\frac{-2.395}{r^2} + \frac{\pi^2}{l^2} \geq 0$ and $\frac{11.295}{r^2} - \frac{\pi^2}{l^2} \leq 0$, the dominant mode is TM_{010} and the second mode is TM_{110}.

$$Max.\ \frac{\frac{3.832c}{2\pi r}}{\frac{2.405c}{2\pi r}} = \frac{3.832}{2.405} \approx 1.593 \tag{5.50}$$

In this instance, the determined ratio remains consistent irrespective of the specific values assigned to r and l, requiring no additional adjustments. The maximum value is found to be approximately 1.593 corresponding with the maximum value identified in the preceding scenario

5.1.2.4. Case-B

If $\frac{-2.395}{r^2} + \frac{\pi^2}{l^2} \leq 0$, the dominant mode is TE_{111}.

$$max \left\{ \frac{min\{f_{TE112},\ f_{TM010}\}}{f_{TE111}} \right\} \tag{5.51}$$

We must determine if the second mode is TE_{112} or TM_{010}.

$$f_{TM010} \lesseqgtr f_{TE112} \tag{5.52}$$

$$\left(\frac{2.405}{r}\right)^2 \lesseqgtr \left(\frac{1.841}{r}\right)^2 + \left(\frac{2\pi}{l}\right)^2 \tag{5.53}$$

$$\frac{2.395}{r^2} - \frac{4\pi^2}{l^2} \lesseqgtr 0 \tag{5.54}$$

If the expression attains a non-negative value, the second mode shall be TE_{112}. Conversely, if the expression is less than zero, the second mode shall be TM_{010}. In the equality scenario, these modes will become degenerate modes; hence, determining which mode to acknowledge as the second mode in the equality scenario is unimportant.

5.1.2.5. Case-B-I

If $\frac{-2.395}{r^2} + \frac{\pi^2}{l^2} \leq 0$ and $\frac{2.395}{r^2} - \frac{4\pi^2}{l^2} \leq 0$, the dominant mode is TE_{111} and the second mode is TM_{010}. We will maximize the function $(f_{TM010}/f_{TE111})^2$ within the constraints below.

$$Maximize\ g(\vec{\phi}) = \frac{\left(\frac{2.405}{r}\right)^2}{\left(\frac{1.841}{r}\right)^2 + \left(\frac{\pi}{l}\right)^2} = \frac{\frac{5.784}{r^2}}{\frac{3.389}{r^2} + \frac{\pi^2}{l^2}} \tag{5.55}$$

$$Subject\ to\ h_1(\vec{\phi}, s_1) = \frac{-2.395}{r^2} + \frac{\pi^2}{l^2} + s_1^2 = 0 \tag{5.56}$$

$$h_2(\vec{\phi}, s_2) = \frac{2.395}{r^2} - \frac{4\pi^2}{l^2} + s_2^2 = 0 \tag{5.57}$$

$$\frac{\partial L}{\partial r} = \frac{-9.94l^2 r}{\left(l^2 + 2.912r^2\right)^2} - \frac{4.79(\lambda_1 - \lambda_2)}{r^3} = 0 \tag{5.58}$$

$$\frac{\partial L}{\partial l} = \frac{9.94lr^2}{\left(l^2 + 2.912r^2\right)^2} + \frac{2\pi^2\left(\lambda_1 - 4\lambda_2\right)}{l^3} = 0 \tag{5.59}$$

$$\frac{\partial L}{\partial \lambda_1} = \frac{2.395}{r^2} - \frac{\pi^2}{l^2} - s_1^2 = 0 \tag{5.60}$$

$$\frac{-2.395}{r^2} + \frac{4\pi^2}{l^2} - s_2^2 = 0 \tag{5.61}$$

Four conditions are listed below.

1. $s_1 = 0,\ s_2 = 0,\ \lambda_1 \neq 0,\ \lambda_2 \neq 0$
   As $s_1 = 0$ and $s_2 = 0$, the value of r^2 calculated from Equations 5.60 and 5.61 do not coincide, signifying that the condition has not been satisfied.

2. $s_1 \neq 0,\ s_2 \neq 0,\ \lambda_1 = 0,\ \lambda_2 = 0$
   The criteria specified in Equations 5.58 and 5.59 are not met as $\lambda_1 = 0,\ \lambda_2 = 0$, and both r and l are greater than zero.

3. $s_1 \neq 0,\ s_2 = 0,\ \lambda_1 = 0,\ \lambda_2 \neq 0$
   From Equation 5.61, $r = 0.2463l$. By substituting into Equations 5.58 and 5.59, all the equations are fulfilled.

4. $s_1 = 0,\ s_2 \neq 0,\ \lambda_1 \neq 0,\ \lambda_2 = 0$
   According to Equation 5.60, r is found to be approximately $0.4926l$. By substituting into Equations 5.58 and 5.59, all the equations are fulfilled.

The maximum value of f_{TM010}/f_{TE111} under these constraints is approximately 1.2 under condition 3. The value found under condition 4 is 1. Nonetheless, the value of 1.20 is less than the identified value of 1.593 in Case A. Consequently, although this value could be a feasible solution within this specific case, it does not specify the global extremum for the entire problem.

5.1.2.6. Case-B-II

The constraints are $\frac{-2.395}{r^2} + \frac{\pi^2}{l^2} \leq 0$ and $\frac{2.395}{r^2} - \frac{4\pi^2}{l^2} \geq 0$ in this case whose first mode is TE_{111} and the second mode is TE_{112}. The first constraint yields $r \leq 0.4926l$, and the second one results in $r \leq 0.2463l$. Satisfying the second constraint ensures the fulfillment of the first constraint as well. Hence, one does not need to include the first one.

$$Max.\ g(\vec{\phi}) = \frac{\left(\frac{1.841}{r}\right)^2 + \left(\frac{2\pi}{l}\right)^2}{\left(\frac{1.841}{r}\right)^2 + \left(\frac{\pi}{l}\right)^2} \tag{5.62}$$

$$Subject\ to\ h_1(\vec{\phi}, s_1) = \frac{2.395}{r^2} - \frac{4\pi^2}{l^2} - s_1^2 = 0 \tag{5.63}$$

$$L(\vec{\phi}, \lambda_1) = g(\vec{\phi}) - \lambda_1 h_1(\vec{\phi}, s_1) \tag{5.64}$$

The partial derivative of the Lagrange function with respect to each variable must be equal to zero.

$$\frac{\partial L}{\partial r} = \frac{17.472 l^2 r}{(l^2 + 2.912 r^2)^2} + \frac{4.79\lambda_1}{r^3} = 0 \tag{5.65}$$

$$\frac{\partial L}{\partial l} = \frac{-17.472 l r^2}{(l^2 + 2.912 r^2)^2} - \frac{8\pi^2\lambda_1}{l^3} = 0 \tag{5.66}$$

$$\frac{\partial L}{\partial \lambda_1} = \frac{-2.395}{r^2} + \frac{4\pi^2}{l^2} + s_1^2 = 0 \tag{5.67}$$

1. $s_1 \neq 0,\ \lambda_1 = 0$
   The criteria set forth in Equation 5.65 and 5.66 are not satisfied as $\lambda_1 = 0$, and both r and l must be greater than zero.

2. $s_1 = 0,\ \lambda_1 \neq 0$
   $\frac{f_{TE112}}{f_{TE111}}$ is 1.20 similar to the previous case under the assumption that $r = 0.2463l$. Although this value represents a local solution for this case, it is not the global maximum.

The analytical investigation demonstrates a conclusive constraint. When examining each of the cases individually, it is established that the frequency of the second mode within a cylindrical cavity is limited to approximately 1.593 times that of the first mode.

5.2. Numerical Verification of Mode Separation Limits

This section hereby attempts to validate the analytical findings through a numerical investigation in a strict way. On the basis of the condition $b \leq a \leq d$ governing the rectangular cavity, the value of b is kept constant at 0.05 m. The subsequent computation of values for a and d takes place under the condition of $a \leq d$ and will go on inductively, starting from 0.05 m. In this process, the resonant frequencies of the TE_{101}, TE_{102}, and TE_{011} modes are computed in the respective loops in a range of $ad \in [0.05, 1]$. The computation at these iterations of frequency values is carried out and orderly stored in the vector, sorted at each step in ascending order. Throughout the iterative calculation process, the value of the ratio of the second frequency to the first is derived. These ratios, intricately drawn out, make their visual representation in Figure 5.1-(a). This figure shows that the region satisfied with the constraint $a \leq d$ achieves the highest value, precisely 1.581. In perfect accordance with the analytical findings, this maximum value occurs when b assumes an appropriate small magnitude, which makes a equal to d. The regions that fail to satisfy the constraint $a \leq d$ are visually outlined as zero on the surface plot.

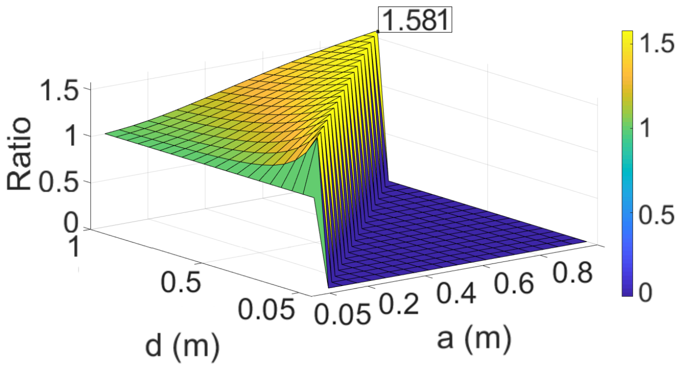

(a)

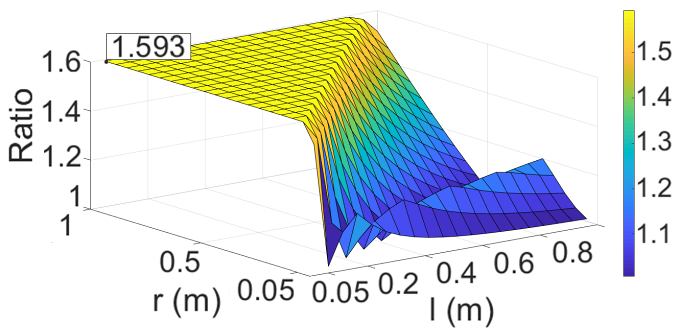

(b)

Figure 5.1. Numerical verification for the resonant frequency ratio of the first two modes of (a) rectangular cavities (b) cylindrical cavities: ©2023 IEEE (Karatay and Yaman, 2024b)

The investigation on the cylindrical cavity was carried out using another approach compared to the rectangular case because of the non-existence of a predetermined hierarchy between parameters r and l. Therefore, the methodical approach employed had to be exploratory since a bounded search was not possible. So, both r and l were systematically varied from 0.05 m to 1 m in each iteration, where the resonant frequencies of TE_{111}, TM_{010}, TE_{112}, TM_{110}, and TE_{211} modes were exactly computed for every pair of values. The resulting ratio of the frequency of the second mode to that of the first, arranged in ascending order, is graphically portrayed in Figure 5.1-(b). The MATLAB code used for this computation sequentially involves the frequencies of the above-stated modes and ensures comprehensive numerical analysis. Hence, with the analytical presentation above, the exclusion of the TE_{211} mode as the first two modes in any circumstance, coupled with the analytical assertion that the value 1.593 remains invariant irrespective of the inclusion of this mode, has been systematically presented. The computational results agree with the analytical results, showing that the ratio of the frequency of the second mode to that of the first is calculated at 1.593. Analytically, possible slight changes from numbers after the decimal point and beyond are considered, owing to rounding in square root and square operations. It finds a local maximum besides the existence of value 1.2 in both Case-B-I and Case-B-II in Figure 5.1-(b). However, it does not represent a global maximum, as carefully deduced from examining each scenario separately. Therefore, as seen from the detailed grid search results, the same global minimum lies at 1, which is a prescribed optimal value for both problems.

5.3. Experimental Validation and Breaking the Limit

In this section, we demonstrate experimental validation and prove that this phenomenon can surpass the restrictions identified in the previous sections for rectangular and cylindrical cavities. Two approaches have been explored: mechanical perturbation with a metallic object carefully placed and another taking advantage of the temperature variations within a dielectric sample. Since the previously known limits are to be surpassed in the first approach, the differential positions of the electric and magnetic field peaks for the relevant modes are appropriately utilized. In the second approach, for the reconfigurable frequency ratio, both the positional data of the electric and magnetic field peaks and the temperature-dependent property of the dielectric constant of water shall be considered. In both approaches, the perfect structure of the rectangular prism and the cylinder should be disturbed.

5.3.1. Metallic Perturbation

Adjusting the resonant frequency of a mode characterized by a particular electric and magnetic field distribution of a cavity is attained by modifying the boundary conditions. Changing either an outward or an inward boundary condition along the cavity's normal surface will alter its resonant frequency, either up or down. The frequency shifts will occur in opposite directions if one region where the boundary modifications are done is located near the electric field peak or magnetic field peak of the relevant mode.

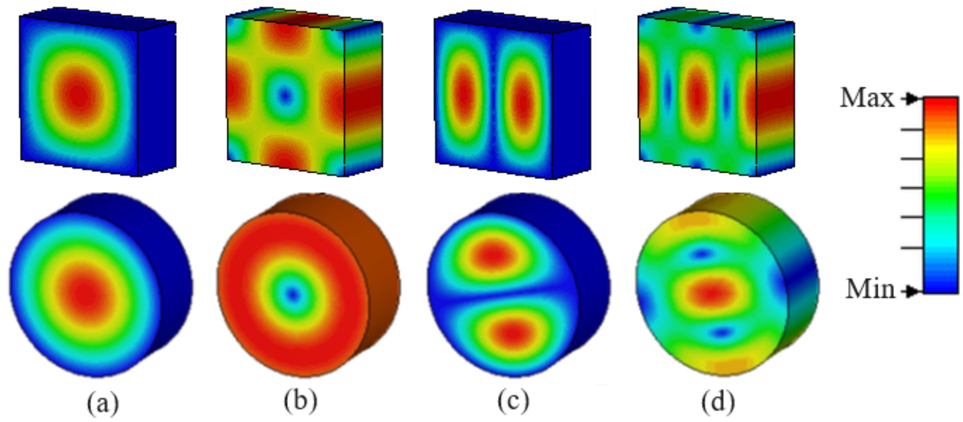

Figure 5.2. Field pattern of the conventional cavities (a) Electric field of the first mode (b) Magnetic field of the first mode (c) Electric field of the second mode (d) Magnetic field of the second mode

$$\frac{\omega_u - \omega_p}{\omega_u} \approx \frac{\Delta W_e - \Delta W_m}{W} \tag{5.68}$$

Here, ω_u and ω_p represent the angular resonant frequency of the unperturbed and that of the perturbed cavity, respectively. ΔW_e represents the change in stored electric energy, ΔW_m denotes the change in stored magnetic energy, and W corresponds to the total stored energy.

In order to induce an inward perturbation in a region characterized by substantial magnetic energy density, the frequency increases; in other cases, if the same perturbation is applied to an area characterized by electric energy density, it reduces the frequency. Similarly, applying an outward perturbation to a region characterized by a high concentration of magnetic energy causes a frequency reduction, while performing the same perturbation in a region governed by electric energy causes an increase in frequency. Note that the first mode's electric field and the second mode's magnetic field peak at the center. On the other hand, both the first mode's magnetic field and the second mode's electric field attain zero as they approach the center of the two conventional cavities; refer to Figure 5.2. Since the condition $a = d \geq 2b$ is valid, the frequency ratio at the limit values can be achieved when adjusting the dimensions of a rectangular cavity to make the first resonant mode frequency of 800 MHz where $a = d = 265$ mm, coincide with $b = 110$ mm. The second mode's frequency will reside near 1.26 GHz, close to the limit computed. The previously described method is also linked to these items, enabling a calculation of the limit relation at which the frequency ratio of both first and second modes in rectangular cavities approaches the lower value. For this, it is to be stressed that the experiment has to be conducted with low coupling and DP experimental setup so that the coupling of antennas least distorts the shape of the rectangular prism, which sustains the ideal rectangular prism assumption. In this case, an inward perturbation applied from the center of the cavity increases the frequency of the first mode and decreases that of the second mode. Hence, the second mode will have an enhanced frequency ratio if an internal perturbation is introduced within the structural body.

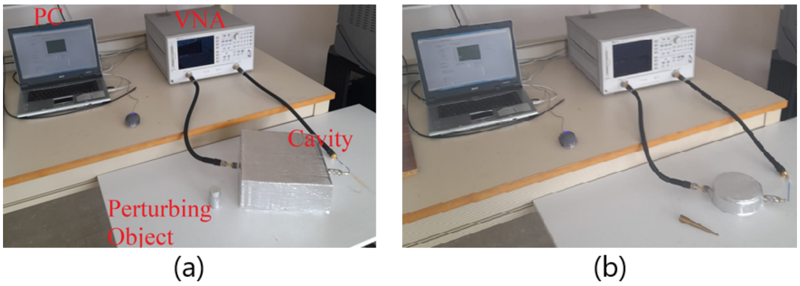

Figure 5.3. Metallic perturbation setup (a) rectangular cavity (b) cylindrical cavity: ©2023 IEEE (Karatay and Yaman, 2024b)

A cylindrical shape is chosen for perturbing the rectangular cavity structure given in Figure 5.3-(a), which has a side length of 35 mm and a height of 45 mm. A similar analysis has also been performed using cylindrical cavities, which have shown that the electric field of the first mode and the magnetic field of the second mode achieve their maximum values at the center of the cavity. On the other hand, the magnetic field of the first mode and the electric field of the second mode have minimum values at the same position. Using this phenomenon, it becomes possible to manipulate the frequency of the first mode downwards and that of the second mode upwards by applying the shape perturbation from the center of the cylindrical cavity. This manipulation enables one to surpass the analytically proven limits, as discussed in the following sections. A cylindrical cavity with a radius of 70 mm and a height of 44 mm was used for measurements with weakly coupled identical couplers; see Figure 5.3-(b). Different modes were manipulated by inserting a conical perturbing object into the top part of the cylindrical cavity. The height of the inserted cone was 26 mm, its top radius was 2 mm, and the bottom radius was 11 mm. The surpassing of these limits can be envisioned in scenarios where the idealized conditions of such geometries are compromised. One can observe in Figure 5.4 that the frequencies of the first two modes of both the rectangular and cylindrical cavities can be separated using the metallic perturbation method so that the surpassability of the analytically proven limit discussed in the previous sections can be made.

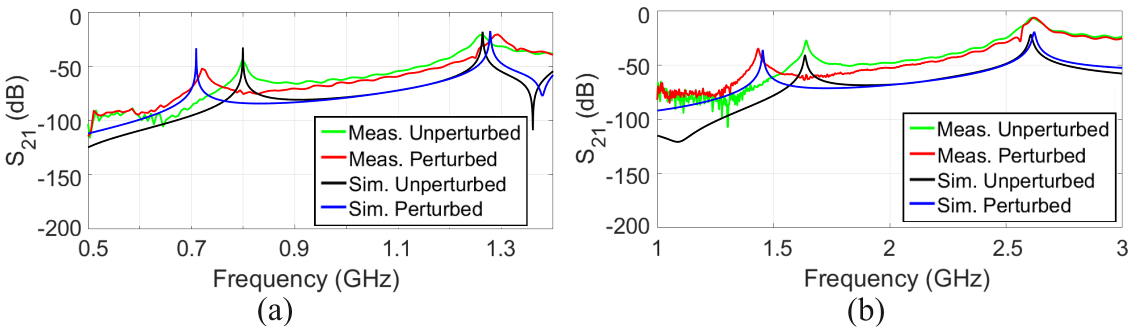

Figure 5.4. Numerical and experimental results of the unperturbed and perturbed (a) rectangular cavity (b) cylindrical cavity: ©2023 IEEE (Karatay and Yaman, 2024b)

A comprehensive investigation was carried out, as indicated in Figure 5.5, to explore potential limitations related to the dimensions of objects that will penetrate inward from the cavity center, where L_p denotes the length of the perturbing object. In order to evaluate the influence of different shapes, a cylindrical object was introduced into the rectangular cavity, and a conical object was placed into the cylindrical cavity. The object sizes were varied in order to observe the resonance frequencies of the first two modes. The length of the perturbing cylinder ranged between 10, 30, and 50 mm, in addition to varying its diameters from 10 to 80 mm in increments of 10 mm. For the case of the conical object in the cylindrical cavity, the top radius was constant, set to 2 mm. The bottom diameter and length varied for the values of 10-30 mm and 10-60 mm, respectively, for the range of sizes of the perturbing object. The perturbing object's size increased as the first mode's frequency decreased in both cavity types. There was an increase in frequency for the second mode, and there was potential for the mode frequencies to be separated if the amplitude of the small diameter perturbation cylinder was relatively high. Nevertheless, once the diameter of the perturbing object exceeded a certain threshold, it disturbed the electric field of the dipole mode, which reduced the frequency.

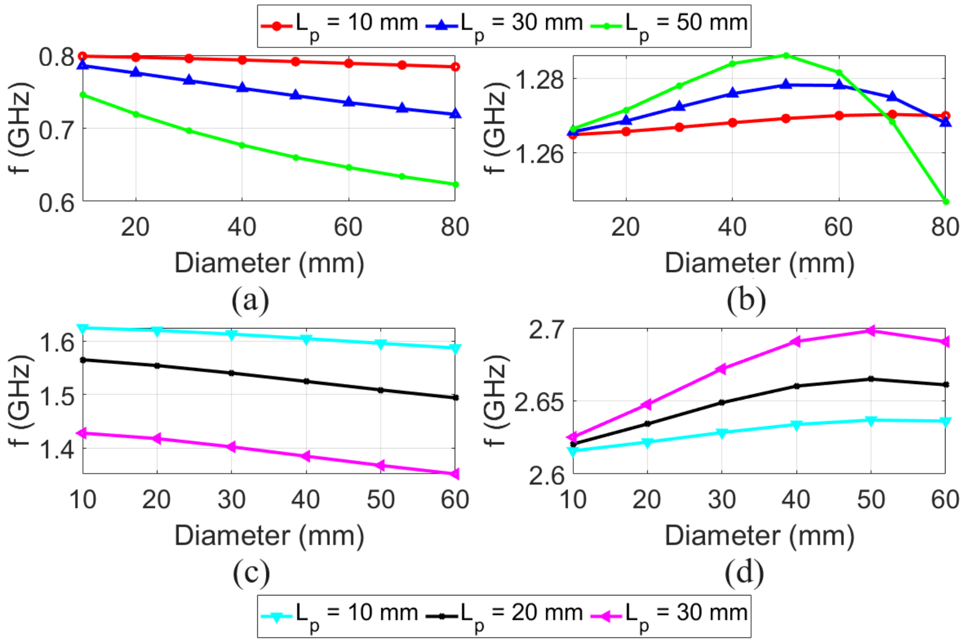

Figure 5.5. Frequency shifts in conventional cavities (a) first mode of the rectangular cavity (b) second mode of the rectangular cavity (c) first mode of the cylindrical cavity (d) second mode of the cylindrical cavity: ©2023 IEEE (Karatay and Yaman, 2024b)

5.3.2. Dielectric Perturbation

Another approach could be to decrease the frequency of the first mode by introducing a dielectric and a non-magnetic material at the peak point of the electric field of the first mode instead of changing the cavity boundaries. This technique may attain a very high reduction in the quality factor compared to the other technique, based on how lossy the dielectric material employed is. However, its reconfigurability is one of its attractive features that can be more beneficial in conferring reconfigurable properties, particularly in samples with liquid compositions, where it can easily be controlled via mixtures or temperature changes. It becomes clear that the cylindrical and rectangular cavities would yield similar outcomes, though, for this subsection, only the cylindrical cavity is examined. While the first mode's electric field peaks at the center of the cavity, the magnetic field vanishes in the same location. Although the magnetic field of the second mode takes a peak at the same point, we need not consider it as the non-magnetic nature of the material employed precludes any magnetic effects.

In addition to the cylindrical cavity considered in the previous subsection, this is also used in the present subsection. A glass tube of 4.82 dielectric constant with an inner radius of 1.8 mm, an outer radius of 2.8 mm, and a height equal to that of the cavity was located at the center. Measurements were made with an empty cavity, a cavity with an empty glass tube, and a cavity with a water-filled glass tube. The glass tube is a cylindrical structure with a closed bottom and an open top for filling. It was attached to the cavity with a thin layer of glue. The emptying cylindrical tube was filled with pure water at 90, 50, and 20 $°C$ using a syringe, and the resonant frequencies of the first two modes were measured using a VNA. All the efforts were made to keep the ratio between the resonant frequencies of the first two modes similar, even when the resonances changed.

Table 5.2 presents measurement results of the first ($f(1)$) and second ($f(2)$) modes' resonant frequencies and the $f(2)/f(1)$ ratio of the empty cavity, cavity with the empty glass tube, and the cavity with the glass tube filled with water. The resonant frequency of the first mode of the cavity being around 1.6 GHz implies that the dielectric constant of water is inversely proportional to the temperature in the region we are operating. Therefore, as expected, the ratio between the first and second modes increases as the water is cooled. In contrast to the shape perturbation approach, this method only affects the mode with a dielectric sample placed in the electric field region; hence, while the frequency of the first mode decreases, that of the second mode remains approximately constant.

Table 5.2. Measured ratio of the first two modes' resonant frequency with varying water temperatures using weakly coupled adapters

	$f(1)$ (GHz)	$f(2)$ (GHz)	Ratio
Empty cavity	1.641	2.611	1.591
Cavity with empty tube	1.630	2.611	1.601
With water $(90\ °C)$	1.493	2.611	1.749
With water $(50\ °C)$	1.462	2.610	1.785
With water $(20\ °C)$	1.437	2.610	1.816

5.4. Separated Mode 3D Printed Cavity

We used the macro for elliptical cavity design in CST-MWS, and the dimensions are given in mm in Figure 5.6-(a). The structure was uniformly scaled in all axes, with a scaling factor of 0.166. To complete the structure, one needs to attach mirror symmetry. The final configuration that includes holes for eight screws, two tuners, and two N-type couplers is presented in Figure 5.6-(b)-(f). The electric field patterns concerning the first two modes are depicted in Figure 5.7. In the context of the applications already discussed earlier, the separation between the frequencies of the first two modes plays a role in avoiding spectrum overlap. This is particularly important in case there are measurements of permeability, permittivity, or any other cavity-based measurement system, as it reduces the risk of crosstalk arising due to frequency shifts and ensures the avoidance of overlap between closely placed modes within the frequency domain.

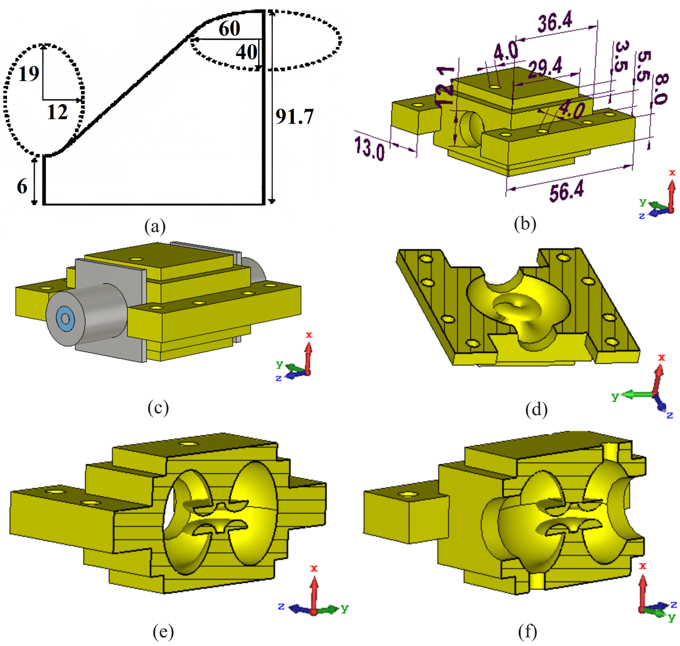

Figure 5.6. Design of the separated mode cavity whose dimensions are in mm (a) elliptical cavity curve of half-cell before scaling of 0.166 (b) final dimensions (c) with the N-type couplers (d) y-z plane (e) x-y plane (f) x-z plane: ©2023 IEEE (Karatay and Yaman, 2024b)

Smith chart view is used to understand the effect of the mode separation on the proposed cavity. For this purpose, rectangular, cylindrical, and proposed cavities were simulated, keeping to the maximum ratio established in previous sections that the first mode was set at 2.45 GHz. For each cavity type, frequency domain solver simulations were conducted in CST-MWS software and incorporated two N-type couplers and two loops. In Figures 5.8-(a) and -(b), rectangular and cylindrical cavities excite a considerable number of modes in the range of 2-6.5 GHz. On the other hand, Figure 5.8-(c) shows the Smith chart representation of the proposed cavity in the range of 2-6.5 GHz, with two slightly under-coupled modes. Compared to the other two cavities, it presents a different pattern in the Smith chart plot, effectively restricting intermodal overlap.

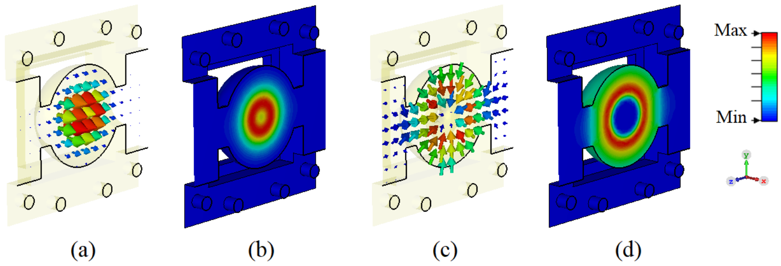

Figure 5.7. Electric field of the cavity (a) vector arrows of the mode-1 (b) contour plot of the mode-1 (c) vector arrows of the mode-2 (d) contour plot of the mode-2: ©2023 IEEE (Karatay and Yaman, 2024b)

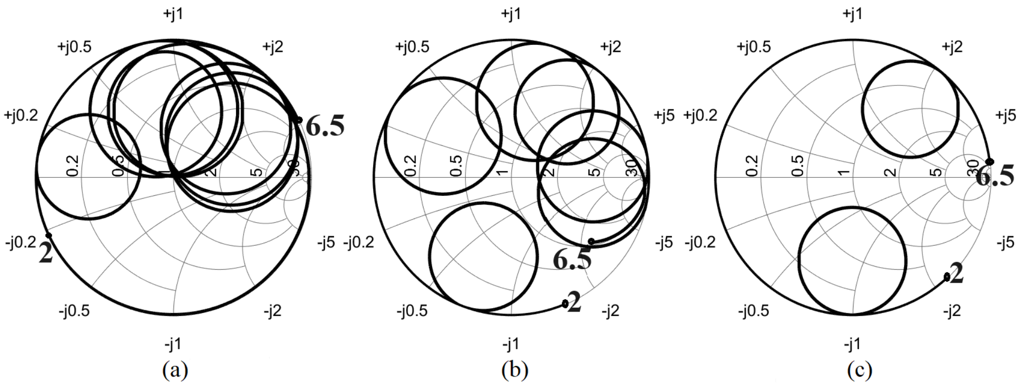

Figure 5.8. Smith chart representation 2-6.5 GHz range (a) rectangular (b) cylindrical (c) proposed: ©2023 IEEE (Karatay and Yaman, 2024b)

The use of Fused Deposition Modeling technology and polylactic acid material resulted in the manufacturing of a two-piece cavity, as indicated by Figure 5.9. The present achievable internal conductivity was achieved by employing the conductive aerosol coating. This gave way to subsequent sealing by utilizing designated screw holes. N-type coupler openings in the cavity allowed for the convenient placement of couplers, each with small loops at both ends, creating a portable configuration for cavity excitation. Plastic tubes having conical configurations with a diameter of 4 mm were inserted into tuner holes on both parts of the cavity. These tubes were filled with LM up to a specified level using approximately two grams of gallium and a syringe. The above procedure addresses potential frequency shifts due to production discrepancies or coating-related factors.

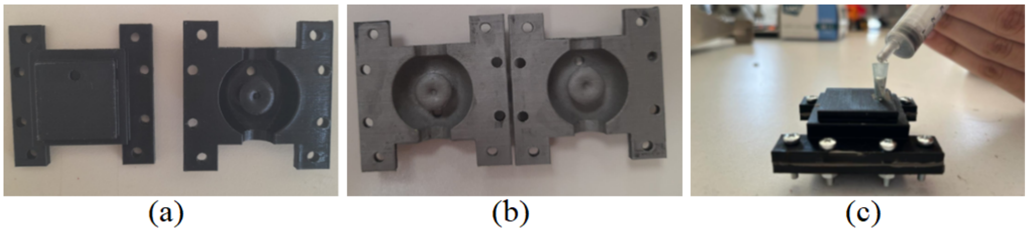

Figure 5.9. 3D printed cavity (a) uncoated pieces (b) coated pieces (c) tuning with LM: ©2023 IEEE (Karatay and Yaman, 2024b)

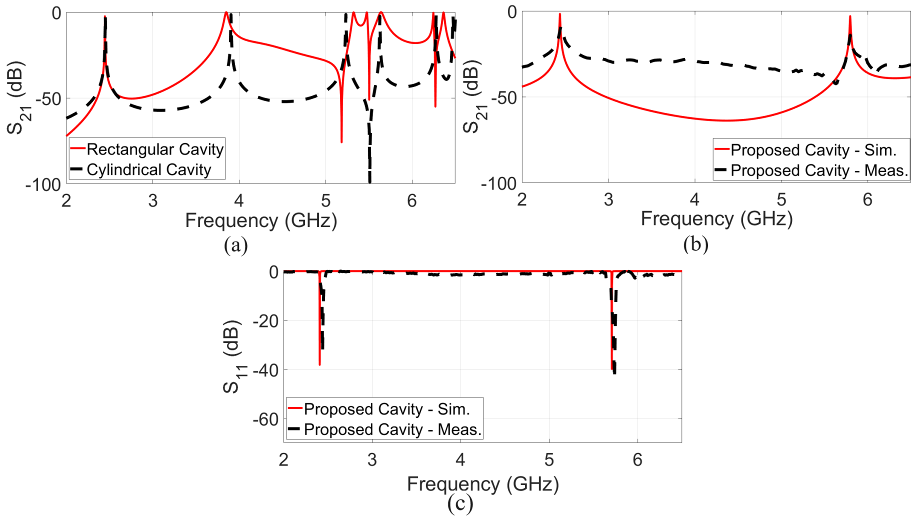

Figure 5.10. Results of (a) simulated S_{21} for conventional cavities (b) S_{21} of the proposed cavity with low β (c) S_{11} of the proposed cavity with high β: ©2023 IEEE (Karatay and Yaman, 2024b)

A detailed and precise computational evaluation has been made to acquire optimal frequency separation on the dimensions of conventional cavities with a dominant frequency at 2.45 GHz. Fig. 5.10-(a) depicts the visually represented outcomes of S_{21} for these structures, excited by dual ports within the simulation environment. Figure 5.10-(b) shows the simulation of the proposed cavity with weak coupling. One is the outcome of the proposed cavity from the simulation, and the other is the measurement of the cavity tuned up to the desired frequencies with the help of the LM tuner. In addition, Figure 5.10-(c) shows the single-port critical coupling results. Though some slight variations in frequency may result from critical coupling measurements, the higher power levels used for measurements yield a more graphically agreed result. These measurements further confirm that the proposed structure has a non-overlapping behavior in the frequency domain.

As seen from Table 5.3, there are differences between the proposed cavity and the rectangular and cylindrical cavities. Since the dominant modes of all three cavities are positioned at 2.45 GHz in the frequency domain, there are restrictions on the second mode of the rectangular and cylindrical cavities. On the other hand, the second mode of the proposed cavity is positioned at 5.8 GHz. Using LM tuners, the frequency of the first mode can be finely tuned between 2.43 and 2.47 GHz, whereas the second mode varies between 5.77 to 5.82 GHz.

The quality factor of the cylindrical and rectangular cavities varies significantly with the volume. In a fair comparison, the settings were adjusted to maintain an equal internal volume. The internal volume of the proposed cavity is close to 10800 mm^3, which means that the cross-sectional dimensions of the rectangular cavity are set to d = a = 86.6 mm to resonate the first mode at 2.45 GHz, with b less than 43.3 mm. For the cylindrical cavity, a radius of 46.8 mm is required, and height was calculated such that previously reported conditions would also be adhered to. The wall conductivity values are accepted in the same way as those of copper. Adjustments to dimensions so that an equivalent internal volume of approximately 10800 mm^3 would mean the quality factor values for the first two modes of the rectangular and cylindrical cavities are much lower than that of the proposed cavity.

Table 5.3. Parameters of the rectangular, cylindrical and the proposed cavities: ©2023 IEEE (Karatay and Yaman, 2024b)

Cavity Shape	Rectangular	Cylindrical	Proposed
Frequency of mode-1 (GHz)	2.45	2.45	2.45
Frequency of mode-2 (GHz)	3.86	3.90	5.8
Ratio	1.58	1.59	2.37
Area	74.8 cm^2	68.8 cm^2	7.3 cm^2
Q of mode-1	1050	1160	3150
Q of mode-2	1310	1460	3750

5.5. Separated Mode Machined Cavity

The conductivity created by coating the cavity produced with a 3D printer needed to be improved for precise dielectric permittivity measurements. Due to the lack of sharp peaks on the VNA screen, the manufacturing of a cavity through machining is applied. However, the curvy design of the cavity in the previous section is unsuitable for machining. Thus, this section presents the new cavity design, its production, and fundamental measurements. The main aim of this novel cavity design is to set the first mode at 2.45 GHz and the second one at 5.8 GHz, having no mode in between these two. This configuration is smartly positioned to reduce the overlapping of modes on the VNA screen and possible problems that may occur with dielectric permittivity measurements due to frequency shifts or peak broadening. Besides that, using the LM probe enables flexible coupling for both cavities with different conductivity values and variations in quality factors induced by different materials under tests (MUTs).

5.5.1. Design Process

The preceding cavity poses such formidable challenges that a new design is accomplished by manufacturing a more feasible procedure that will be conducted by smoothing out the curves. The objective comprises the following: the reshaping of the cavity's structure in order to realign the first mode precisely at 2.45 GHz and the second mode at precisely 5.8 GHz, commencing with a cylindrical cavity of first mode frequency above 2.45 GHz and a second mode frequency below 5.8 GHz. The shape perturbations are applied to the regions, whereby the second mode of electric fields has their peaks. The E-solver of CST-MWS was utilized to achieve the final configuration; see Figure 5.11.

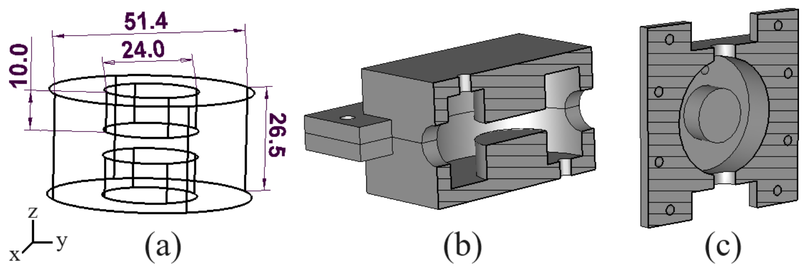

Figure 5.11. Cavity with flattened folds (a) dimensions in mm (b) cross-section (c) half piece: ©2024 IEEE (Karatay and Yaman, 2024c)

As seen in Figure 5.12, the cross-sectional views of the simulated cavity are represented through vector arrows showing the electric field for the first two modes of the simulated cavity with different cross-sectional planes. The resonance at 2.45 GHz corresponds to a TM_{010}-like mode of a cylindrical cavity, where the electric field peaks at the center of the cavity. On the other hand, for the second mode, the electric field's peak magnitude is centered around the inner recess of the cavity. After the cavity design, two distinct materials were used in manufacturing: the dark gray is steel, and the light gray is aluminum, as shown in Figure 5.13. The production involved designing each cavity in two separate pieces carefully aligned and secured through bolts. These pieces consist of a total of eight screw holes, which match each other and are fitted with M4-type screws with a diameter of 4.2 mm. At the points of intersection of the pieces, N-type coupler holes are drilled into the respective pieces to accommodate the couplings required for DP excitation of the cavity. Also, tuner holes with a diameter of 4 mm on both pieces provide the flexibility to insert a frequency tuner to adjust the resonant frequency.

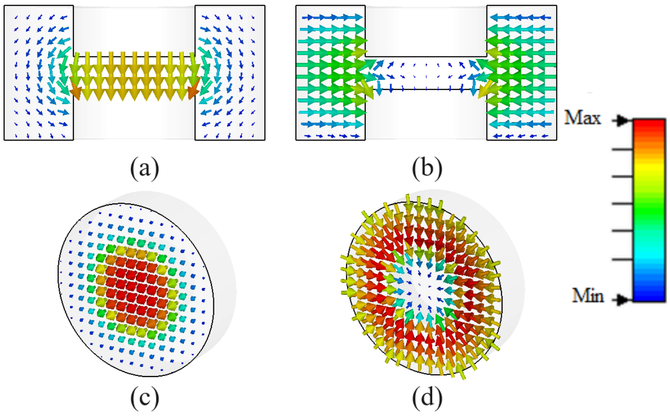

Figure 5.12. Electric field pattern (a) y-z plane mode-1 (b) y-z plane mode-2 (c) x-y plane mode-1 (d) x-y plane mode-2: ©2024 IEEE (Karatay and Yaman, 2024c)

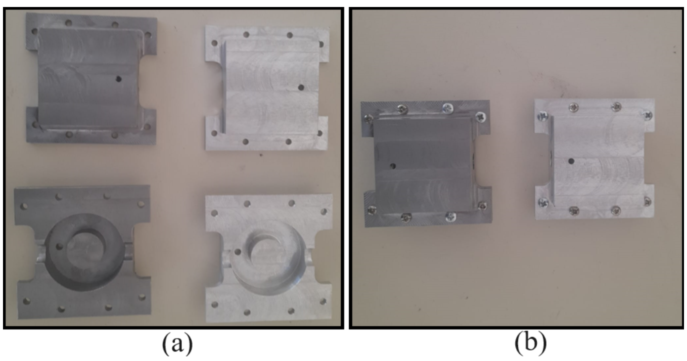

Figure 5.13. Fabricated cavities (a) unassembled (b) assembled: ©2024 IEEE (Karatay and Yaman, 2024c)

5.5.2. Simulations and Measurements

When the conductivity of the cavity changes, or when a MUT is placed inside the cavity, the quality factor will, therefore, change and result in an altered β value. This reconfigurable feature of the coupler probe ensures that we can keep the coupling factor at the required value in terms of any changes within the cavity.

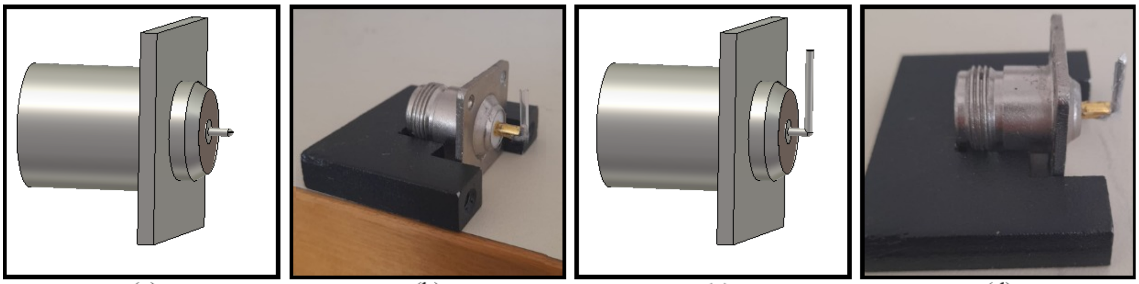

(a) (b) (c) (d)

Figure 5.14. LM-based coupler probe (a) single-mode model (b) single-mode photo (c) dual-mode model (d) dual-mode photo: ©2024 IEEE (Karatay and Yaman, 2024c)

A new technique is based on the use of LM displacement to dynamically adjust the coupling factor of a mode and modify the modes being excited. This new method has two excitation states for the coupler probe: single-mode and dual-mode operations. In the configuration of single-mode operation, a current is applied parallel to the electric field lines of the 5.8 GHz mode while being orthogonal to the electric field vectors of the 2.45 GHz mode, thus effectively preventing the excitation of the latter. This is achieved by keeping the glass tube empty. On the other hand, during dual-mode operation, the glass tube is filled with LM, and a current parallel to the electric field vectors of the 2.45 GHz mode is applied, and this way, both modes can be excited. Photos of the CST-MWS model of the coupler and for both operation states can be seen in Figure 5.14.

Weak coupling measurement results show that, in the single-mode state, only the mode at 5.8 GHz gets excited, whereas, in dual-mode operation, both modes at 2.45 GHz and 5.8 GHz are excited, demonstrating good agreement between simulations and measurements; see Figure 5.15. Using two different metals, the constructed cavities achieved modes at the desired frequencies without a tuner. The unloaded quality factor for the steel cavity was about 310 and 230 for the first two modes, respectively, and approximately 1800 and 1500 for the same modes in the aluminum cavity. The measurements were carried out with weak coupling, so the external quality factor converges to infinity, and the unloaded quality factor closely approximates the loaded quality factor.

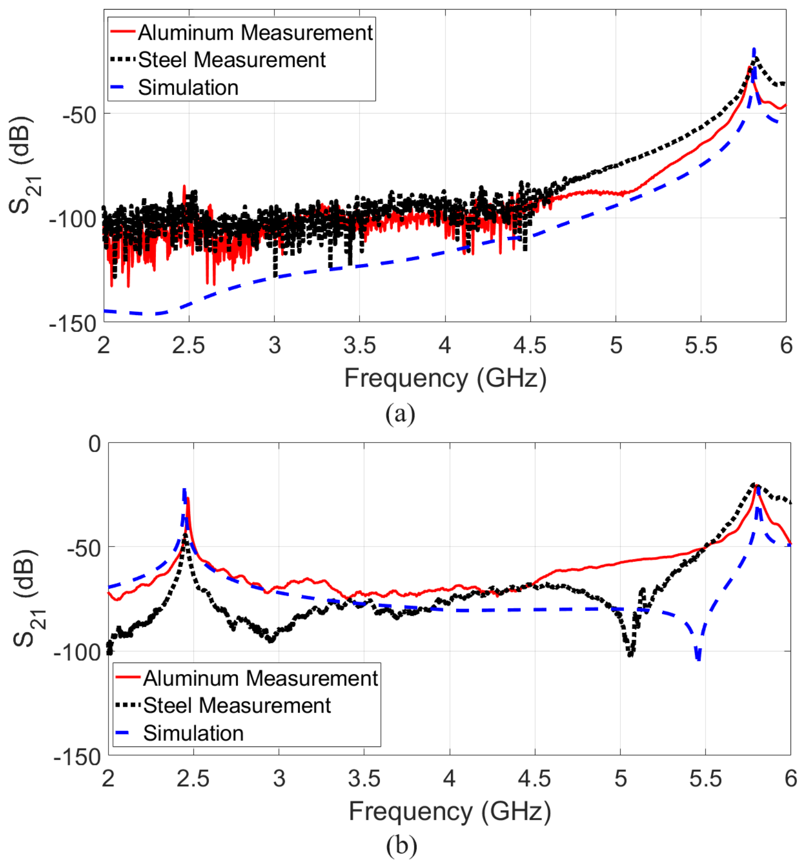

Figure 5.15. Transmission results of the fabricated cavities (a) single-mode operation (b) dual-mode operation: ©2024 IEEE (Karatay and Yaman, 2024c)

The investigation involved taking the probe diameter as 0.6 mm and examining whether the length of gallium or in other words, the length of the L probe (L_g), is dependent on the excitation of different modes. This means that one would look at the reflection graph of the first port, and the fundamental variable being investigated here is whether the L probe's length change leads to the excitation of some other mode. According to the results obtained with the eigenmode solver, it was found that between 2.45 GHz and 5.8 GHz, no mode is supported. Therefore, the L probe's length variation would not create any change. Figure 5.16 shows the effect of the length of the L probe on S_{11}. It has been simulated for three different values: 8 mm, 9 mm, and 10 mm. As per the simulation results, at most, two excited modes were obtained for all three length values within the relevant frequency range. It should be noted that the coupling factor of the first mode increases as the probe length increases, whereas the coupling factor of the second mode decreases.

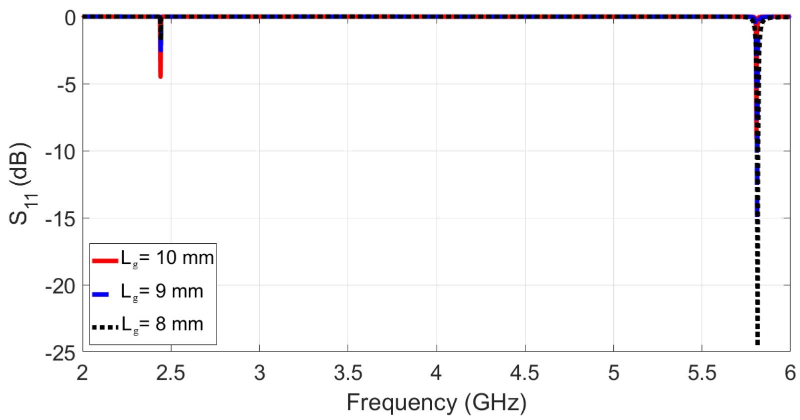

Figure 5.16. Effect of the gallium length when the diameter is fixed to 0.6 mm: ©2024 IEEE (Karatay and Yaman, 2024c)

5.6. Discussions

In this chapter, the cavity design centers on the first two modes located at 2.45 GHz and 5.8 GHz, emphasizing the concept of separated modes. The first analysis was if this design is achievable with a conventional rectangular or cylindrical cavity. The optimization problem becomes an analysis of all possible scenarios regarding the design using Lagrange multipliers and slack variables with an exhaustive examination. The ratios become approximately 1.581 for rectangular cavities and 1.593 for cylindrical cavities, which were checked through the usage of a grid search. Due to the fact that the desired mode placement requires this ratio to be around 2.37, it has been established that such a mode separation is not feasible for these two types of cavities. Such an investigation also provides insights into the complicated relationship between cavity geometry and resonance.

Numerical simulations and experimental demonstrations, on the other hand, help reveal that the limit may actually be violated by a modification of cavity geometries while diverging from that of an ideal rectangular prism or cylindrical structure. In both metallic and dielectric perturbation methods, this has been confirmed from the observation that analytically proven limits can be surpassed by disturbing the perfection of cavity structures. This elucidates, for the first time, the possibility of surpassing this limit through the application of a new cavity design. In this context, simulation studies initially built a curvy cavity, which was fabricated using a 3D printer. However, in the measurement of the dielectric permittivity, the quality factor may require to be high enough, and the quality factor provided by aerosol coating may need to be revised for this operation. To meet requirements, machining was chosen for production, and the design was changed by smoothing out the parts of the curvy cavity suitable for this method.

Another innovative operation on the machined cavity is the use of an LM-made coupler probe to enable control over the coupling factor. It allows for the achievement of both single-mode and dual-mode excitation with the coupling factor within the allowed scope. Although the solidification of the LM at 29 °C does not come with a challenge to this process, it can actually be assured that the stability is secured by the freezing of gallium after the shape change. In this case, the features that bring significant advantages for the dielectric permittivity measurement to be seen in the next chapter and were successfully implemented in the process have been detailed in this chapter.

CHAPTER 6

DIELECTRIC PERMITTIVITY MEASUREMENTS

The next step is to measure dielectric permittivity in an iterative manner via a mixture-based approach. We present a technique to give a less complicated and less time-consuming operation to replace simulations that could run for hours with mixing performed to determine the complex dielectric permittivity of the unknown material in a few minutes. With respect to the analysis of complex dielectric information at various volume fractions, it becomes possible to derive the dielectric permittivity of an unknown material. The results in this chapter have been published in the article (Karatay and Yaman, 2024c).

6.1. Iterative Process

The measurement of dielectric permittivity with microwave cavities is commonly employed since the dielectric permittivity of a material is normally nonlinear against the resonating frequency and Q. On the other hand, the material perturbation equation gives an analytic expression for determining material permittivity, although in some cases with less precision than iterative methods. Iterative methods are versatile since one can apply them to many complicated structures and geometries that cannot be solved in the classical material perturbation equation. In other cases, when the shape of the material or cavity is arbitrary, then the classical material perturbation equation will not suffice. The classical material perturbation equation will call for rearrangements, subjecting all the rearrangements to make them applicable for all shapes, and the challenge posed by such rearrangements is considered significant.

The starting point of this research is the fact that the permittivity values of homogeneous or heterogeneous liquid mixtures can be approximated using various dielectric mixture models. Often, since their main aim is to approximate the permittivity of a mixture, such models have been invented. The most significant part in this respect lies in the degree of compatibility between the reference liquids, considering factors such as their polarizabilities and interaction coefficients. This choice of model can be different based on the characteristics of the liquids involved. These models are idealized and have limited applicability for most mixtures. With decreasing solubility ratios between liquids, there seems to be a necessity for a greater deal of models. Also, all these models have mostly focused on the real part of permittivity and might be called into question regarding the imaginary part.

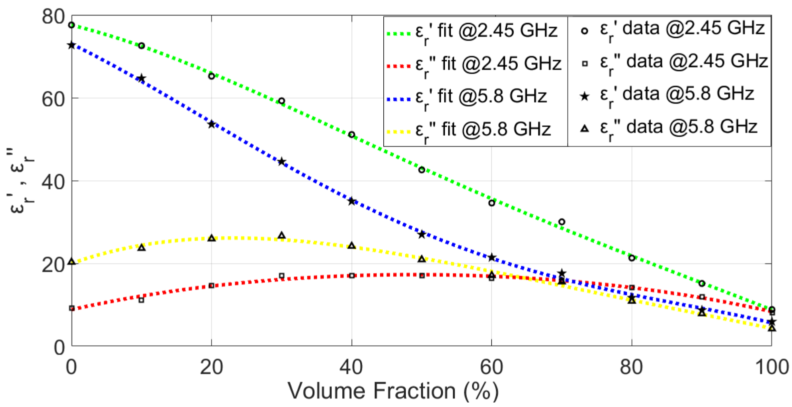

Figure 6.1. Room temperature dielectric properties of ethanol-water mixture at 2.45 GHz and 5.8 GHz: ©2024 IEEE (Karatay and Yaman, 2024c)

One can use measurement results already existing as a reference in an iterative process to determine the permittivity of MUT. In order to illustrate this idea, the dielectric permittivities of ethanol-water mixtures at various volume fractions were used as references at room temperature for frequencies of 2.45 GHz and 5.8 GHz. The fundamental principle is to calculate the permittivity of an unknown substance by relying on existing experimental data related to the ethanol-water mixture found in the literature. Beginning with pure water and moving toward pure ethanol with ten percent increments, the real and imaginary parts of the dielectric permittivity are shown in Figure 6.1 where ε_r is represented as $\varepsilon_r' - j\varepsilon_r''$. The term ε_r' corresponds to the dielectric constant, which is also called the real component. These data points are fitted to 4th-order polynomials to estimate intermediate values. The process is intended to make four distinct iterations, covering both real and imaginary components for both frequencies. In determining the real component of the permittivity, the frequency shift brought about by the MUT is mainly sought to align with that induced by the ethanol-water mixture. In the iteration of the imaginary part, the final value can be determined by aligning the drops in the Q. Using the bisection method, an optimal fraction is independently determined for the real and imaginary components of the permittivity of the MUT. This process is repeated for both 2.45 and 5.8 GHz frequencies. We can now derive the required intermediate steps rapidly without depending on commercial 3D electromagnetic software, as shown in Figure 6.2.

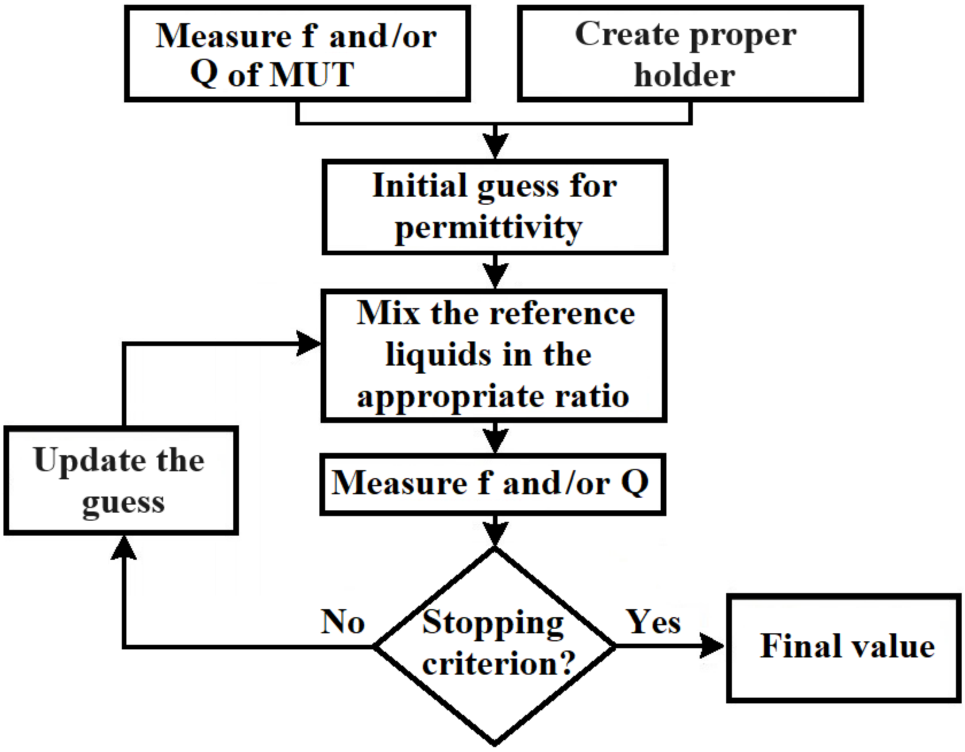

Figure 6.2. Flowchart of the proposed algorithm: ©2024 IEEE (Karatay and Yaman, 2024c)

6.2. Iterative Results

Two samples of a glycerin-water mixture and beef liver were conducted for dielectric permittivity measurements using the proposed algorithm. In order to induct the two samples, namely Sample 1 and Sample 2, into the designed cavity and position them in the peak areas of the electric fields corresponding to the first two modes, see Fig. 6.3. We measured the imaginary part and encountered challenges since they were frequency-dependent. Differences in their real components may, therefore, result in significant disparities in the resonant frequency of the cavity, resulting in divergent quality factor values. Hence, the locations and sizes of the liquids and those of the holders within the resonator are the key parameters that ensure the uniqueness of the imaginary component. This aims to reduce the frequency dependence of the quality factor by minimizing the frequency shift.

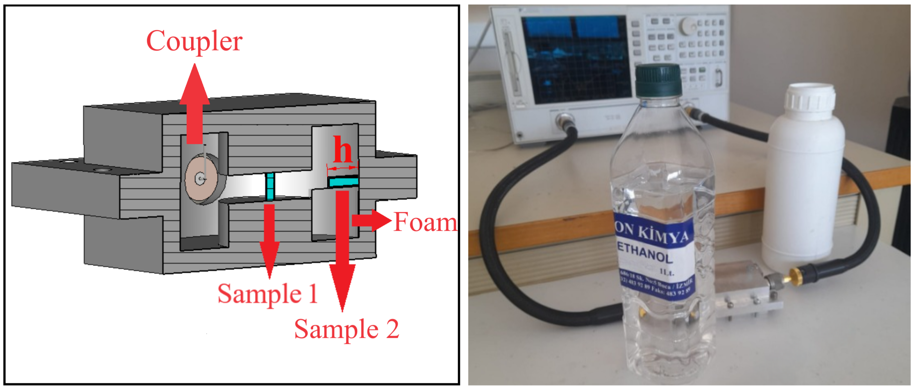

(a) (b)

Figure 6.3. Experimental setup (a) model of the cavity and sample holders (b) liquids used in the iterative process: ©2024 IEEE (Karatay and Yaman, 2024c)

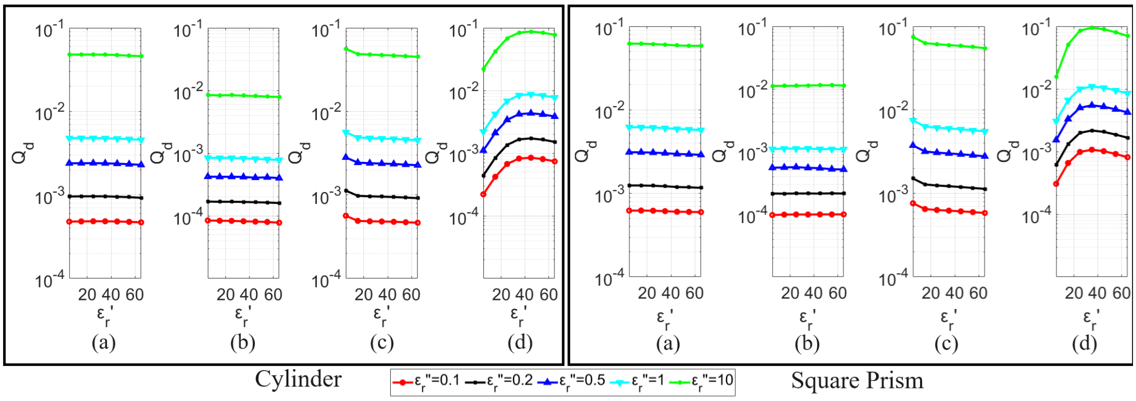

Figure 6.4. Q drop (a) h = 8.7 mm at 2.45 GHz (b) h = 8.7 mm at 5.8 GHz (c) h = 22.6 mm at 2.45 GHz (d) h = 22.6 mm at 5.8 GHz: ©2024 IEEE (Karatay and Yaman, 2024c)

For validation of the applicability of the proposed method for measuring the imaginary part, simulations were carried out with varied permittivity values in order to analyze changes in the quality factor. This was realized by systematically varying the real part of the permittivity sample from 5 to 65 with an imaginary permittivity ranging from 0.1 to 10. Simulations, assuming the value denoted as "h" in Figure 6.3-(a) is both 8.7 mm and 22.6 mm, are then made in order to measure the dependence of the quality factor changes on imaginary permittivity under varying dielectric constants at both frequencies; refer to Figure 6.4. In the case of 8.7 mm, at both frequencies, a linear response was observed. However, when the holder length increased to 22.6 mm, the same ε_r'' could result in different quality factor changes for different ε_r'. To show that sample shape does not have a significant effect on the results, they were simulated using both a cylindrical sample with a diameter of 2 mm and a square prism with an edge length of 2 mm, yielding highly comparable results.

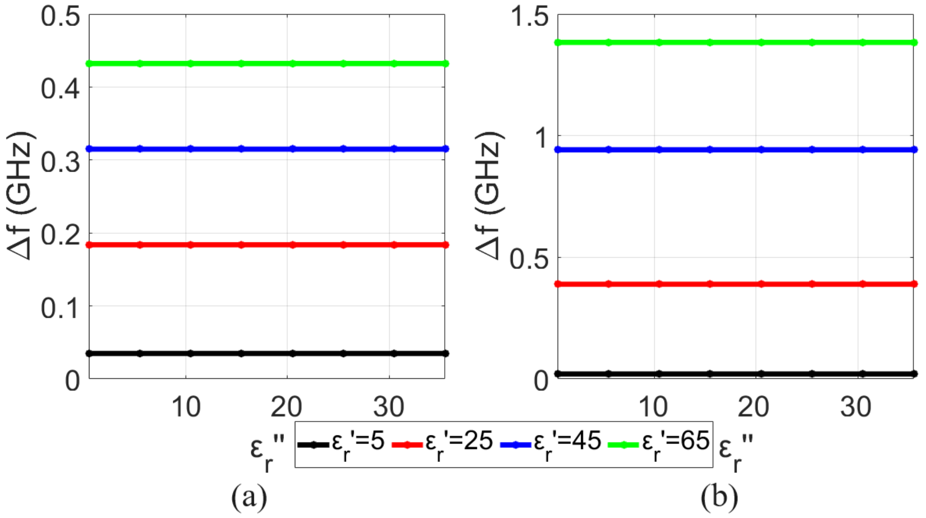

Figure 6.5. Frequency shift (a) mode-1 (b) mode-2

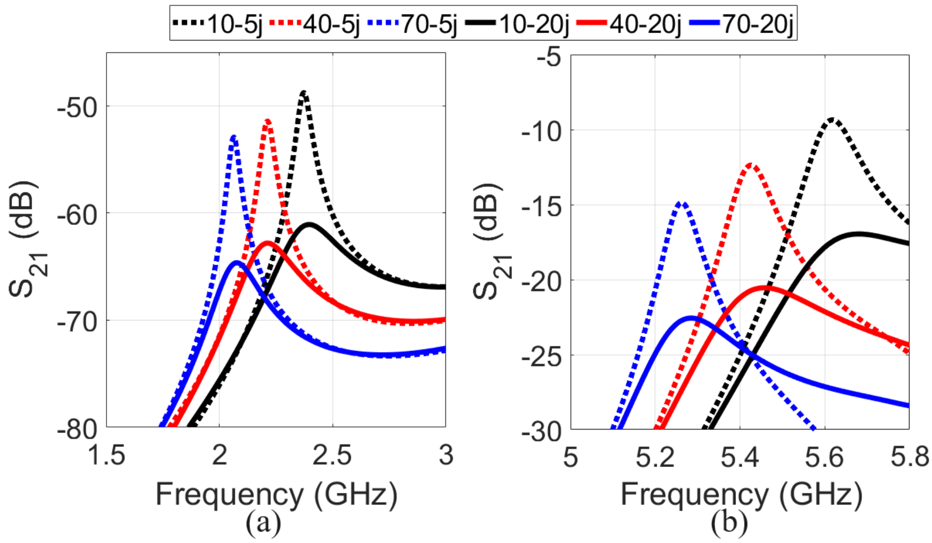

Figure 6.6. S_{21} graph (a) mode-1 (b) mode-2: ©2024 IEEE (Karatay and Yaman, 2024c)

To check if the real part is unique within our working range, simulations are required for frequency shift. Since the imaginary part must not have a large sample size, we opted to simulate only the cylindrical sample by maintaining the same dimensions as before. As the real part of permittivity does not appear to vary over different frequencies, any change of imaginary component does not vary the frequency shift; see Figure 6.5. This assertion is in accordance with our study range. To enhance visual clarity and more explicitly present the results, plots of S_{21} are shown in Figure 6.6 with selected values defining the limits of our working range. These plots result in outcomes that agree with the previous ones. According to these plots, the changes in the real part lead to a shift in the frequency while the imaginary component is constant. If the real part is constant within our working range of 5-25, the imaginary part does not create any frequency shift but only contributes to the broadening of the peaks. As the broadening of a peak implies a change in the quality factor, the change in dielectric constant affects the frequency, while the imaginary component affects the quality factor independently, resulting in distinct outcomes.

6.2.1. Liquid Sample

After inserting the MUT, an 80% glycerin and 20% water mixture, in a square prism holder, we recorded both frequency and quality factor variations in both modes. Following this, the MUT was entirely removed from the cavity, and the iterative matching process was initiated for the frequency shift and quality factor drop at 2.45 GHz and 5.8 GHz. This was achieved using an ethanol-water mixture with various volume fractions. The iterations began with pure water and pure ethanol, and at the further range of frequency shift and quality factor values of the MUT, iterations were further progressed by the bisection method. High Q showed sharper S_{21} peaks, being more accessible to be measured accurately with frequency, as seen in Figure 6.7. Iterating the imaginary part of permittivity in the steel cavity was not possible due to the lower quality factor, but it was quite suitable in the aluminum cavity, where the presence of a lossy sample did not affect this. The depicted results were derived from the dielectric characterization study for a glycerin-water mixture at 2.45 GHz and 5.8 GHz frequencies, as available in the literature (Meaney et al., 2017). The results indicated a minimal error rate, particularly for the real part of permittivity.

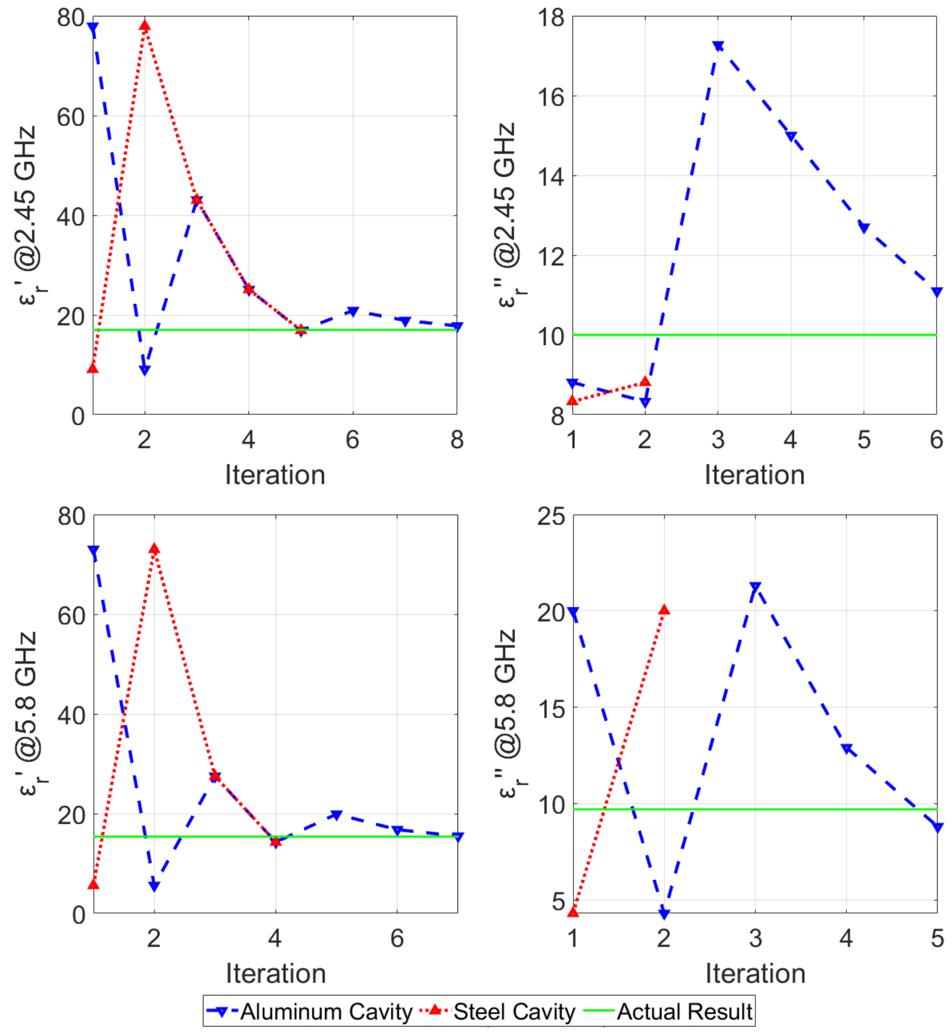

Figure 6.7. Iterative results of 80% glycerin-20% water mixture by referencing ethanol-water mixture: ©2024 IEEE (Karatay and Yaman, 2024c)

6.2.2. Solid Sample

In this measurement, cylindrical holders with a diameter of 2 mm and the lengths previously mentioned were used instead of square prism holders, which implies the applicability of this measurement approach to different holder shapes. We utilized beef liver as MUT. In Figure 6.8-(a), a picture in the top right corner indicates the liver in place within and without the holder. The bottom side of the holder is sealed with silicone. The fact that the actual Q values of the steel cavity are insufficient led to the sole consideration of the aluminum cavity iteration for the liver, which is seen in Figure 6.8 so that at both frequencies, both real and imaginary components fall within the range of the actual values. Permittivity values related to liver can be found in various papers in the literature (Fallahi et al., 2020; Abdilla et al., 2013; Balduino et al., 2019). However, these values can be affected by the water content inside the sample.

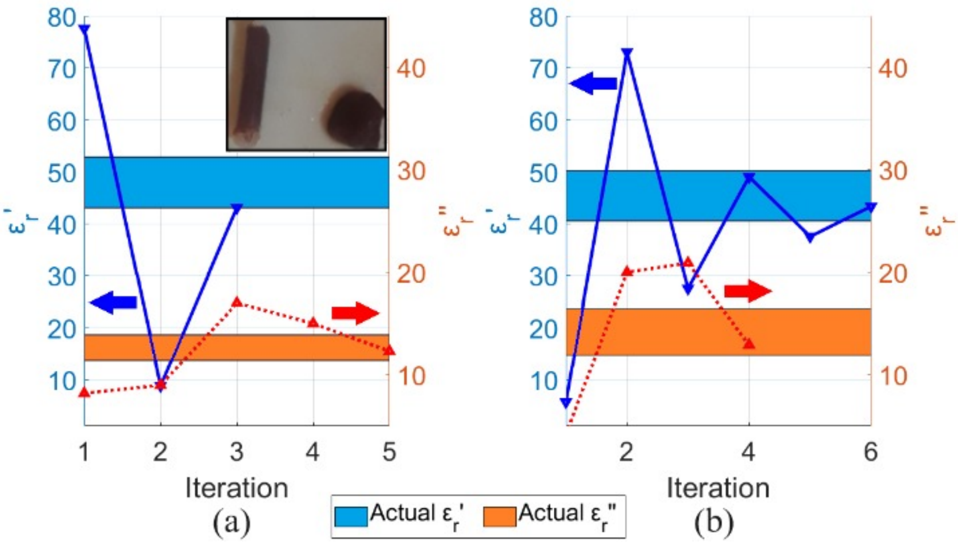

Figure 6.8. Iterative results of ex vivo beef liver in the aluminum cavity (a) 2.45 GHz (b) 5.8 GHz: ©2024 IEEE (Karatay and Yaman, 2024c)

6.3. Discussions

In this approach, the methodology is characterized by its iterative nature since it seeks to generate more realistic results with a foundation provided by established materials, compared to analytical methods with an inherent approximation. However, there are several important aspects that should be considered when carrying out the respective procedural approach. For instance, in this research, water and ethanol were selected as reference materials, and the measurement range was set by the dielectric constants associated with these substances. Still, numerous investigations into the mixture ratio of various materials are available in the existing literature, such as glycerin-water (Meaney et al., 2017) and methanol-water (Smith Jr et al., 1998). In this way, measurements can be performed across a range of dielectric permittivity by means of different mixtures. Although it is not obligatory for the foundational liquid to be water, it often emerges as a prudent choice due to its comparatively high dielectric constant, thereby broadening the scope of the measurement range.

One possible alternative to the abovementioned idea would be creating a look-up table that would relate frequency shift with dielectric constant. Nevertheless, this table will be impracticable because the sizes and shapes of samples tend to change and thus have no actual usefulness. The suggested approach has been tested with two different sample shapes and has had successful outcomes. In addition, quite comparable results may still be obtained even with the same small quantity of a liquid sample occupying only part of the holder. Further, if there is a need to measure a solid sample that does not conform to the holder's shape, then the outer surface of the relevant solid sample can be modeled and generated with a 3D printer. The resulting 3D printed model may then serve as a holder, facilitating the iterative measurement process for the sample solid on which it is based, even with the presence of liquid mixtures.

Apart from these constraints, the primary dimension flexibility for the sample and holder is limited. As the measurement of the real component relies on frequency shifts and changes in the Q are not directly connected to this measurement, a large imaginary permittivity can broaden the peak of the relevant mode, complicating the determination of the resonance point. Premature termination of the iteration in the steel cavity is attributed to measuring the real permittivity value. Conversely, suppose the Q of the hollow cavity is sufficiently large for the continuity of the measurement. In that case, the actual value of the imaginary part becomes less critical within our measurement range. In measurements of imaginary permittivity, complications arise since the quality factor also changes with the frequency. In order to ensure the quality factor change is small, particularly at the frequency shift for the calculation of imaginary permittivity, it is crucial to ensure that the frequency shift is slight and that the quality factor change is dependent on the real permittivity of the dielectric is minimized. Additionally, if the holder is large and has a dielectric constant that is greater than that of air, then this can negatively affect the measurement accuracy. It is of great importance that the holder be kept thin, small, and of a low dielectric constant while minimizing losses for accurate measurements.

Another critical consideration is ensuring that volume fractions or volumes align with those in the reference and taking into account intermolecular forces if involved. This research advances to volume fractions, although literature data is generally available at molar or volume concentrations. It has to be ascertained whether these ratios represent pre-mixture or post-mixture data and adjust the iteration for accuracy since hydrogen bonding interaction in water is potentiated by constant dipole-dipole interaction and robust hydrogen bonding in ethanol facilitated by the oxygen-hydrogen (OH) bond (Jacobsen et al., 2021). While ethanol has a single site as a hydrogen bond donor, water, since it has dual hydrogen atoms bonded to an oxygen atom, can accept and donate multiple hydrogen bonds. The difference in hydrogen bonding potential imbues a special character in the interaction of ethanol with water. For example, at room temperature, 1 mole of water has a volume of 18.07 cm^3, and 1 mole of ethanol has a volume of 58.65 cm^3 (Delgado et al., 2013). With this in mind, the post-mixture partial volumetric value would be 16.60 cm^3 for 1 mole of each substance, giving an ethanol volume fraction of 76.45% (as per pre-mixture data). However, due to intermolecular interactions, the post-mixture partial volumetric values are 16.60 cm^3 and 57.93 cm^3 respectively (Delgado et al., 2013), which also change the ethanol volume concentration to 77.73%. This clearly illustrates the fact that it should be noted when using the values from the reference data in order to obtain the best possible results from any error rate.

Table 6.1. Absolute percentage and root mean square error (RMSE) for the glycerin-water mixture: ©2024 IEEE (Karatay and Yaman, 2024c)

Step	1	2	3	4	5	6	7	8
Error at 2.45 GHz (%)	345	48	146	43	3	19	8	1
Error at 5.8 GHz (%)	374	64	79	7	29	9	1	-
Mode-1 RMSE	0.3672							
Mode-2 RMSE	0.4571							

Six unique measurements were conducted at room temperature for each mode at 2.45 GHz and 5.8 GHz. For each of the first mode measurements, four out of six were terminated at the eighth iteration step, while two measurements ended at the fifth step. In terms of the second mode measurements, only one was finished in the fourth step; the rest were terminated in the seventh step. The termination points of the measurements differ between the two modes, and these are listed in Table 6.1. Due to temperature variation caused by either a change in the environment or electromagnetic influence, the dielectric constant of the sample may be expected to change over time. This would lead to an early termination of the iteration process or an inaccurate result. To provide a measurement environment that would be more dependable, exciting the cavity with weak coupling increases the input power needed to heat the sample. This ensures a more accurate measurement environment. Further deflection in the liquid volume inside the holder, as well as other elements like air bubbles, will pre-cease the iteration or take the investigation astray. However, experimental findings suggest that such events do not cause a noticeable margin of error.

When absolute percentage error analysis was performed for the solid sample, the error rate was found to be relatively low; see Table 6.2. Since the true value of the dielectric constant for the liver depends largely on moisture content, the value provided is a range and not a single result, and the beef liver used in the study was concluded to be very close to the lower true limit of the relevant range according to the results obtained.

Table 6.2. Absolute percentage error for the beef liver: ©2024 IEEE (Karatay and Yaman, 2024c)

Iteration	3	4	5	6
Error at 2.45 GHz (lower boundary) (%)	0.9	×	×	×
Error at 2.45 GHz (higher boundary) (%)	17.0	×	×	×
Error at 5.8 GHz (lower boundary) (%)	32.0	17.0	7.4	6.9
Error at 5.8 GHz (higher boundary) (%)	45.2	2.4	25.2	13.7

Table 6.3. Comparison of various cavity-based permittivity measurement systems: ©2024 IEEE (Karatay and Yaman, 2024c)

	f_1(GHz)	Size (λ^3_{long})	Q	Error (%)
(Kik, 2016)	3.3	0.088	3800	6
(Santra and Limaye, 2005)	2.85	0.609	NA	10
(Özkal and Yaman, 2023)	1.5	0.210	60	1.3
(Kilic et al., 2012)	2.55	0.064	NA	5.2
(Karatay et al., 2023)	2.46	0.198	233	6.7
Proposed	2.45	0.027	1800	1.1
	3D Tool	ε'' Meas.	High ε'	Arb. Shape
(Kik, 2016)	✗	✓	✗	✗
(Santra and Limaye, 2005)	✓	✓	✓	✓
(Özkal and Yaman, 2023)	✓	✗	✓	✓
(Kilic et al., 2012)	✗	✓	✗	✗
(Karatay et al., 2023)	✗	✓	✗	✗
Proposed	✗	✓	✓	✓

Although the proposed approach has limitations, it significantly outperforms many similar approaches in the literature. Table 6.3 compares various cavity-based permittivity measurement methods, focusing solely on cavity-based methods. Although the resonant cavity method is typically applied for single-frequency measurements, it can be broadened to many frequencies when simultaneous excitation of various modes takes place. In order to achieve very high accuracy in the measurements, both the first and the second modes were located at 2.45 GHz and 5.8 GHz, respectively. This would be a set of specific boundary conditions to ensure that other modes exist at no other place, thus being in conformity with very stringent conditions in the measurement of the permittivity. The small dimensions used in the proposed cavity structure do not cause any substantial drop in the quality factor, as had been previously demonstrated by the existing literature. The iterative approach in the proposed method is free from the limitations inherent to high dielectric constants and the determination of complex permittivity in arbitrary-shaped structures. Moreover, through an experimental iteration method, the proposed method significantly accelerates the process, and with an error rate much lower than those seen in analytical counterparts and comparative to iterative counterparts, this opens up new pathways for highly accurate, expedited measurements of complex permittivity.

CHAPTER 7

WATER-CONTROLLED DOPPLER RADAR

While controlling the Doppler radar with LM provides a practical and robust solution compared to electronic reconfiguration methods, the viscosity of gallium and its alloys is considerably higher than those of fluid materials like water. This makes their control using liquid pumps quite challenging. Moreover, the accessibility of gallium and its alloys is much lower than that of water-based materials, and these materials are more expensive. For these reasons, simple modifications have been made to the radar antennas controlled by gallium. The antennas were transformed into a form that can be controlled with saline water. In this chapter, the DB beam-switching option is obtained by filling the cavities of Rx and Tx antennas with water-based mixtures, and the results of this feature for use in Doppler radar are presented.

7.1. Design Process

No modification was introduced to the fundamental dimensions of the LM-controlled DB Vivaldi antenna discussed in Chapter 4; directly, these antennas were applied, and mechanical changes were implemented on them; see Figures 7.1 and 7.2. The design process includes drilling holes in the cavities of the antennas, with each cavitation having a drill. The feed line at the back of the antenna passes through the exact boundary of the cavity. It is imperative not to damage it while drilling since it has a thickness of around 0.6 mm. Suppose the line disconnects, and no electrical contact is established. In that case, repairing this line with auxiliary conductive materials like very fine solder or conducting paint is possible. This is similar to the LM-controlled Vivaldi antenna, and the condition where the left cavity is filled is defined as State-1, and the condition where the right cavity is filled is called State-2, which are simulated. In the simulations conducted, saline water was used, a material defined in the CST-MWS software's library, with a dielectric constant of 74 and a conductivity value of 3.53 S/m.

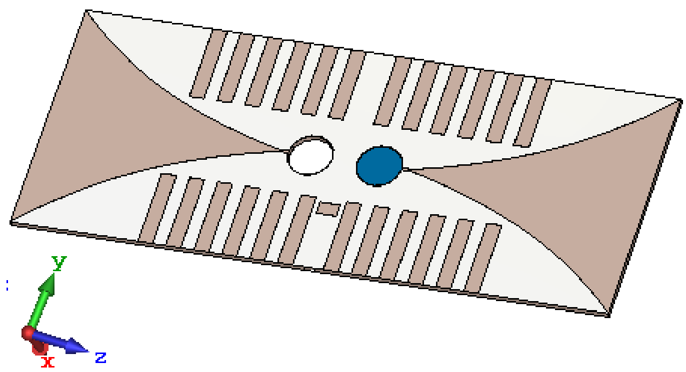

Figure 7.1. Structure of the water-controlled DB Vivaldi antennas in State-2

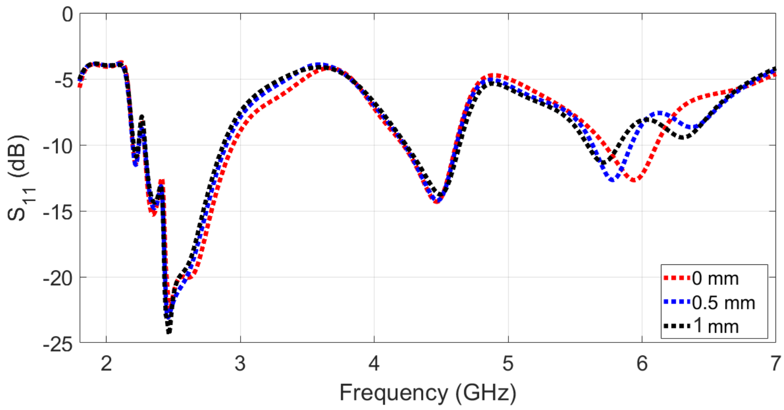

Figure 7.2. Effect of the excess of water on S_{11} of DB Vivaldi antenna

Scenarios involving the precise filling of the cavity with saline water surpassing the boundary by 0.5 mm and 1 mm are simulated. The simulation would aim to observe possible variations in cases where, upon placing a cylindrical holder within the defined region, we would not be able to fill the water completely up to the boundary or in cases where there would be a possibility to surpass the boundary. The simulations started with checking whether the S_{11} parameter would be affected at 2.45 GHz; there was not any significant effect. However, a shift in the mode around 5.8 GHz was observed, depending on the height, reaching the optimal value at a thickness of 0.5 mm at the 5.8 GHz frequency. In an actual experimental environment, due to the holder effect and deviations in the dielectric constant, this value might not have significant meaning. However, it is beneficial in indicating the possibility of optimizing S_{11} around 5.8 GHz by changing height.

The influence on the pattern is higher than that of saline water on the S-parameters. With gallium, one should also be able to obtain the beam-switching feature. In this regard, the effects of the same simulation scenarios on the far-field plots at 2.45 GHz and 5.8 GHz have been examined. Since there was no element disrupting symmetry, only the results of State-2 were examined by assuming the mirror symmetry of State-1. For this purpose, the cavity on the right side of the antenna was filled with saline water. As a result of filling the cavity on the right side with saline water, it has been observed that, like LM, the maximum directivity was concentrated on the other side, and increasing saline water height does not cause a significant change in this trend. Figure 7.3 shows simulations conducted for scenarios where the saline water height exceeds the substrate height by 0 mm, 0.5 mm, and 1 mm. In this case, it is noted that as the height increases, the direction of the main lobe remains the same, but the back-lobe suppression value improves. The difference between FBR at 0 mm and 0.5 mm is significant. Throughout the measurements, a holder will be needed to keep the water inside the cavity, and this holder will have an effect since the dielectric constant of the holder will differ from that of the liquid. However, since the holder used has very thin walls and is approximately 1 cm in diameter, this effect can be neglected.

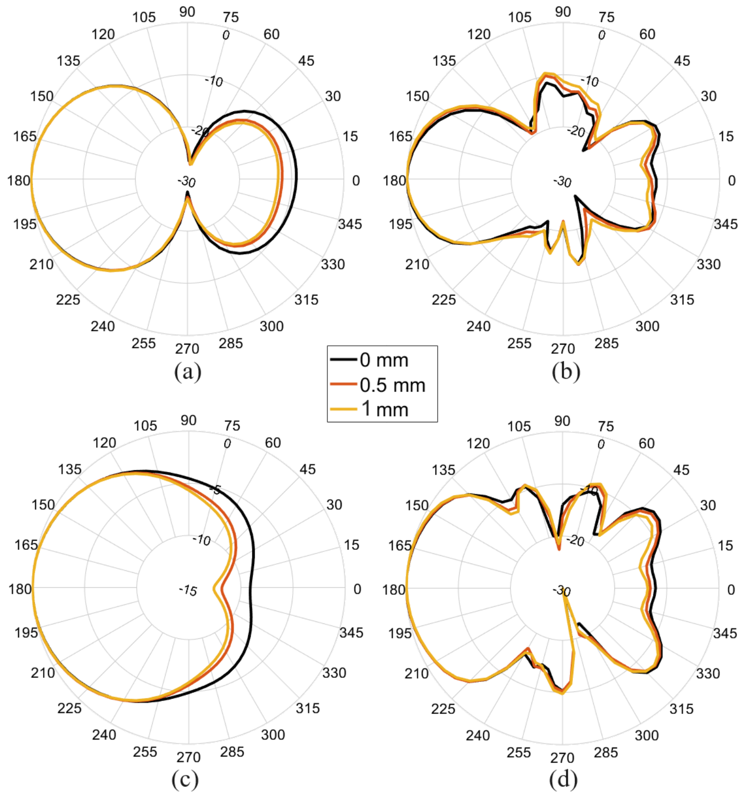

Figure 7.3. Effect of the excess of water on normalized far-field graphs of the DB Vivaldi antennas at State-2 (a) $\phi = 90°$ at 2.45 GHz (b) $\phi = 90°$ at 5.8 GHz (c) $\phi = 0°$ at 2.45 GHz (d) $\phi = 0°$ at 5.8 GHz

7.2. Results

Prior to conducting any experiments, the permittivity value of the material to be employed must be included in the experiment. Using the saline water solution as a reference and determining the intermediate values with the curve-fitting method is reasonable in this case. For instance, the permittivity value of an unknown volume fraction saline water solution can be established at frequencies of 2.45 GHz and 5.8 GHz for ranges of volume fractions starting at 0% to 10% (Cheng et al., 2014; Kumar, 1979). Next, the bisection method explained in the previous chapter can be used.

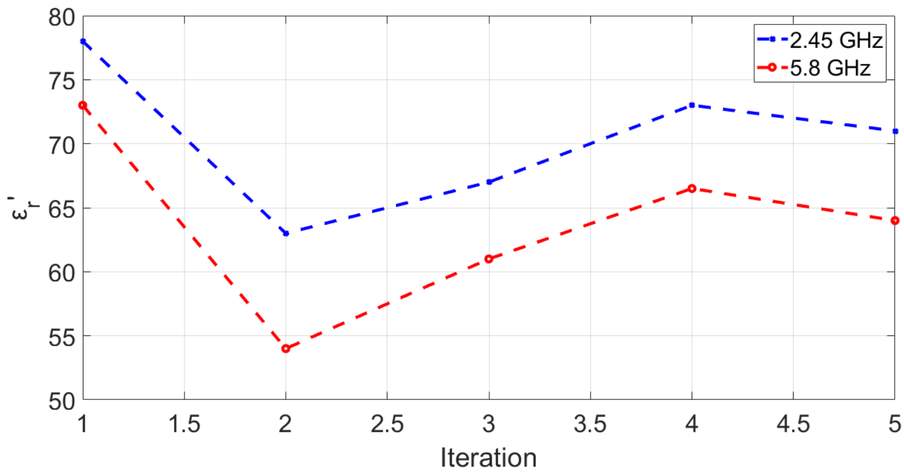

Figure 7.4. Iteration of the dielectric constant of saline water at 2.45 GHz and 5.8 GHz

The fraction of the so-called unknown saline water solution's volume fraction is approximately 3.5%. From the beginning value of 0% to 10% in steps of 5%, then to 2.5%, followed by 3.75%, the dielectric constant at 2.45 GHz has been estimated to about 71, while at 5.8 GHz, the dielectric constant is about 64. The resonant frequency reached in the fifth iteration matches that obtained from the unknown material with the constraint of the VNA sampling point. Therefore, the iteration can be stopped at the fifth step. With the determination of the dielectric constant of the saline water solution, the drilling process of the cavity regions of the Vivaldi antennas for the placement of the respective material has also been carried out.

After drilling the cavities of the respective Vivaldi antennas designated as Tx and Rx, fitted with a pipette of approximately 1 cm in diameter and fixed with adhesive to the antenna, in a manner ensuring that water was allowed to ingress and egress only from the top of each antenna by sealing the bottom, ensuring an environment very much like the simulated conditions. The salinity level of the water used was 3.5%, which reflects the average salinity level in oceans, and hence, the measurement shows its potential applicability using the provided reconfiguration method in maritime settings. Water was filled up to a height of 1.5 mm for the experiment. When no difference in operating frequency is expected between State-1 and State-2, a 180-degree rotation in the pattern is desired. VNA measurements revealed two operating frequencies in the range of 2-6.5 GHz based on the Tx antenna results for both State-1 and State-2; see Fig. 7.5.

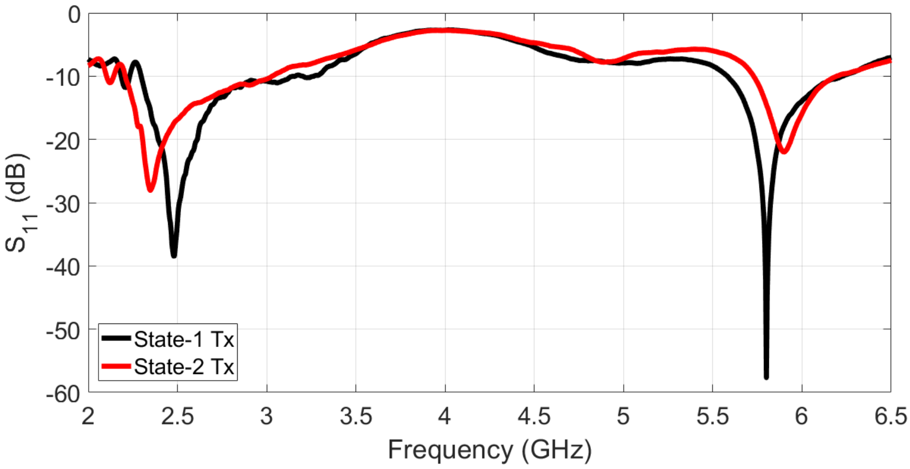

Figure 7.5. Measured S_{11} of the water-controlled Tx Vivaldi antenna

The Tx antenna yields S_{11} values of -19 dB and -31 dB at 2.45 GHz, while at 5.8 GHz, it provides -57 dB and -15 dB values. It follows from the results where all values are less than -10 dB that it can be confidently stated that the Tx antenna keeps an acceptable impedance match in both states and at both frequencies. The S_{11} measurements for the Rx antenna are given in Fig. 7.6. It is evident that while an impedance match is visible around 4.7 GHz in State-1 in these plots, the antenna works in both states for both 2.45 GHz and 5.8 GHz frequencies. At 2.45 GHz, Rx provides S_{11} values of -17 dB and -30 dB for State-1 and State-2, respectively, while at 5.8 GHz, it has values of -15 dB and -20 dB. The antennas, which have a value of S_{11} of -15 dB even in the worst case, are sufficiently suitable for short-range Doppler radar applications.

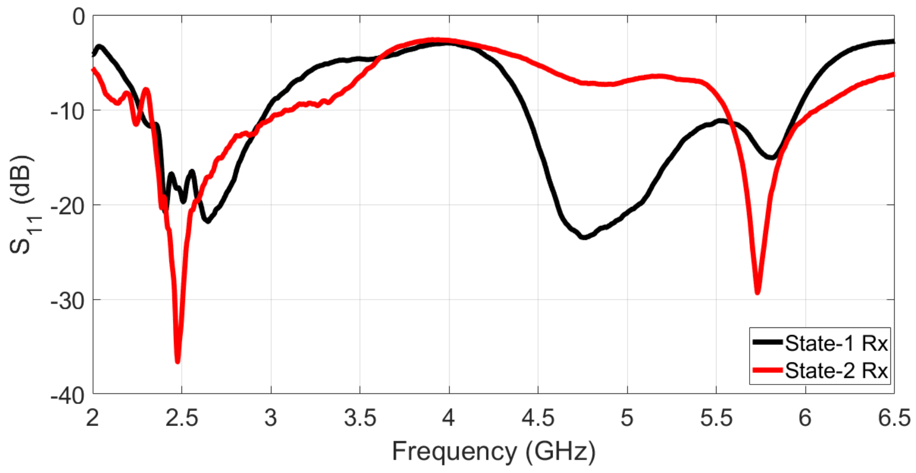

Figure 7.6. Measured S_{11} of the water-controlled Rx Vivaldi antenna

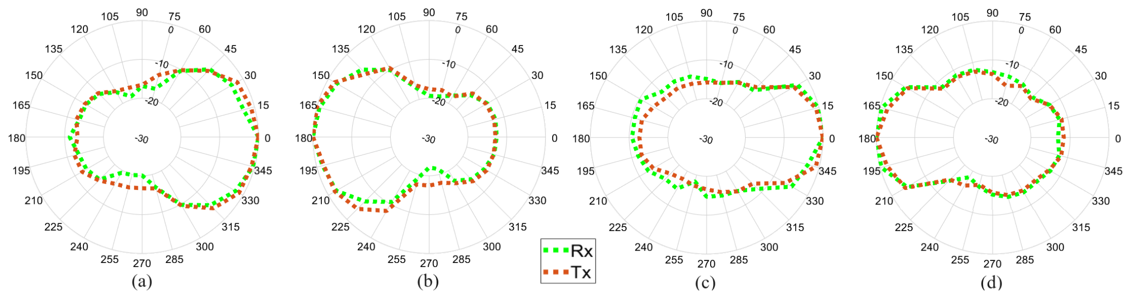

Figure 7.7. Normalized far-field measurement results of the water controlled Vivaldi antennas at $\phi = 90°$ (a) State-1 at 2.45 GHz (b) State-2 at 2.45 GHz (c) State-1 at 5.8 GHz (d) State-2 at 5.8 GHz

The primary role of the proposed structure is that it performs the capability of beam switching at both operating frequencies and can be controlled with a much more readily available material than LM-controlled structures. The top of the antenna structures was left open for water flow since when holding them inside the holder, unlike gallium, is more complex; the antenna was only held in the horizontal position for pattern measurements and hence only generated far-field patterns at $\phi = 90°$. The measurement results in Fig. 7.7 confirmed that with the Rx and Tx antennas in State-1, the maximum directivity is oriented towards $0°$ at 2.45 GHz and 5.8 GHz. Similarly, with the State-2 of the antennas, there is a maximum directivity to $180°$ at both frequencies that match its primary function. These graphs, composed of eight measurements, including two antennas, two states, and two frequencies, demonstrate that the FBR value remains above 10 dB, representing the aspired performance.

In the final step, the saline water-controlled antennas were integrated into the Doppler radar system, and test measurements were taken. Similar to previous chapters, we carried out measurements for each state and frequency to test the suitability of the proposed design for multi-target detection, confirming the applicability of the proposed reconfiguration for the Doppler radar system. Unlike the previous configuration, this reconfiguration method also allows using a liquid pump due to the low viscosity of water. In Figure 7.8, a pendulum continuously moves to the right of the radar, while measurements are taken by changing the antennas' states and the radar's operating frequency. When the antennas are in State-1, the moving pendulum is detected as it remains within the main lobe of the antennas. However, when the antennas transition to State-2, the pendulum movement remains in the back lobe, providing approximately 26 dB suppression at 2.45 GHz and about 22 dB at 5.8 GHz due to the total FBR value.

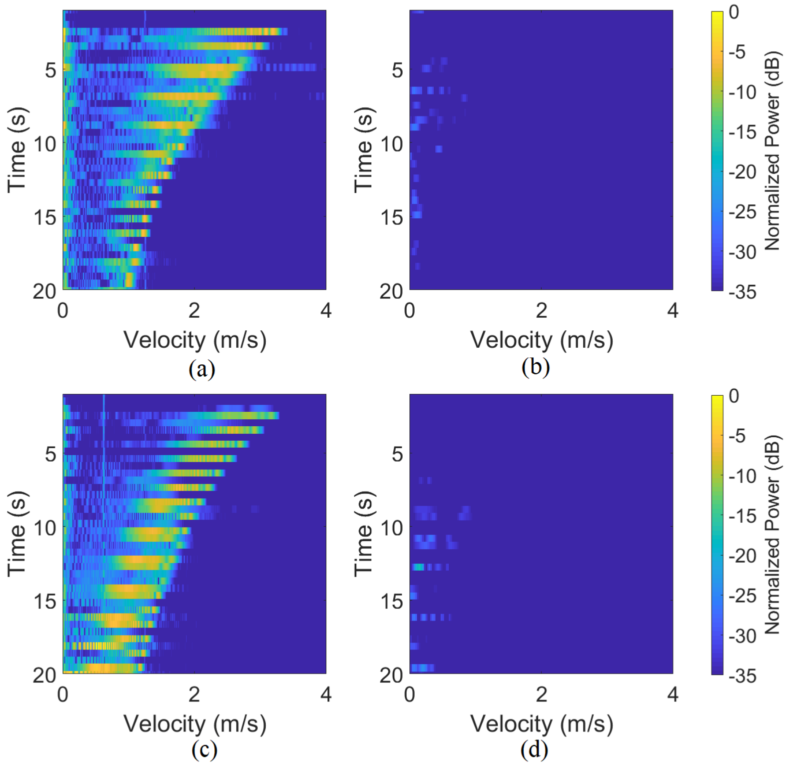

Figure 7.8. Velocity measurement of a pendulum (a) State-1 at 2.45 GHz (b) State-2 at 2.45 GHz (c) State-1 at 5.8 GHz (d) State-2 at 5.8 GHz

Unlike LM radar, automated liquid displacement can carry out the relevant measurement process instead of manual dripping. As mentioned above, the holes opened in the cavity areas of the antennas create the required space for water flow. The relevant holes are seen in Figure 7.9-(a). In order to control the movement of saline water, four water pumps were included in the system for two cavities of Tx and Rx, and their photographs are shown in Figure 7.9-(b). In order to hold saline water, water pots about half a centimeter high and the same diameter as that of the cavities were added to the rear parts of the antennas; see Figure 7.9-(c). These pots were obtained by gluing a plastic straw to the antenna and closing its end. Water pumps can be controlled with a DC of 3-6 volts, allowing forward and reverse movement. In this way, it can be controlled with the help of a device that can provide timed DC voltage, such as Arduino. A certain amount of saline water in the straws attached to the end of the water pumps, and the cavity pot of the antenna can fill and empty the relevant pot by going back and forth. The viewing angle of the radar can be determined depending on which cavity of the antenna is occupied; see Figure 7.9-(d).

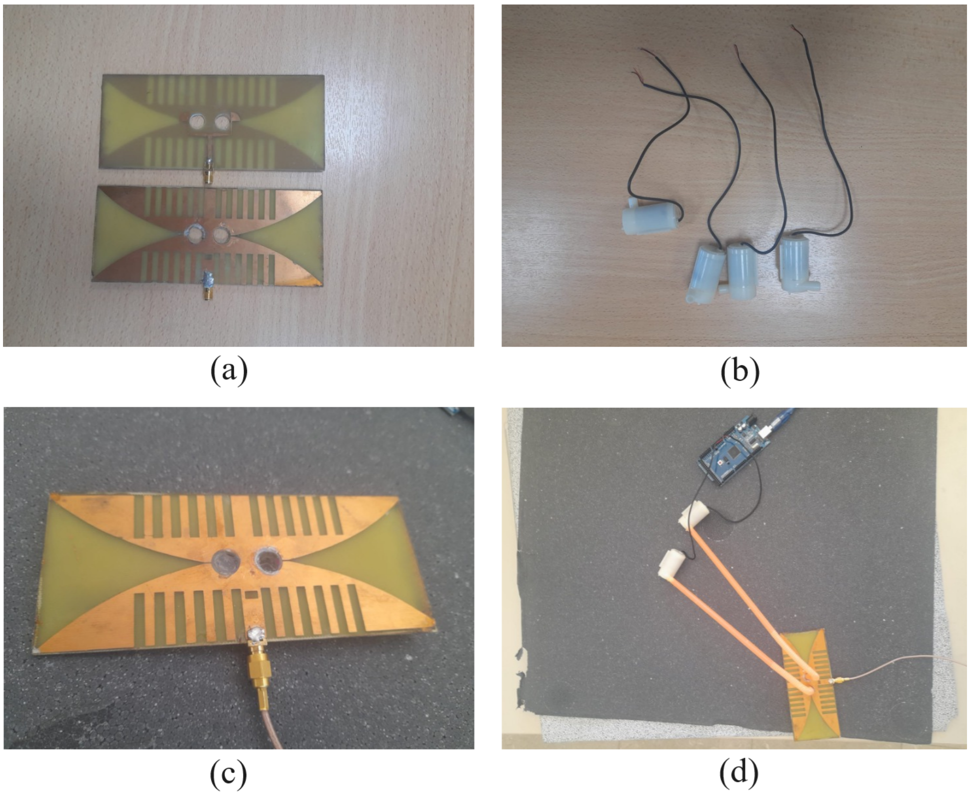

(a) (b) (c) (d)

Figure 7.9. Photos of the saline water-reconfigurable system (a) Drilled antennas (b) Water pumps (c) Antenna at State-1 (d) Saline water-based reconfiguration system

7.3. Discussions

In this chapter, we present the drilling of the Vivaldi antennas' cavities and the pipettes' placement with the same diameter in the corresponding areas. The corresponding region was filled with saline water to enable beam switching. Unlike LM-controlled antennas, the material used in this chapter is water-based, readily available, inexpensive, and eco-friendly. Additionally, due to the lower viscosity compared to the gallium and gallium-based alloys, it is possible to displace the liquid material with a pump and achieve automated behavior.

While saline water is not commonly preferred for reconfiguration in the literature due to its high losses at microwave frequencies, in our proposed design, its function is to prevent resonance and create an impedance mismatch. Therefore, we redirect the power toward the unfilled direction. In other words, the lossy feature of the saline water does not negatively affect the antenna performance. It even contributes positively, allowing us to keep the FBR level above 10 dB. It provides a solution to the reluctance to use inexpensive, eco-friendly, readily available, and easily controllable materials that are typically avoided due to their inherent losses. With the proposed design, we conduct a demonstration to address the abovementioned concerns.

The demonstrated suitability of the proposed antenna for a Doppler radar is an essential indicator of its potential for maritime applications. For instance, physically rotating radar antennas on ships may require powerful motors, and adjusting beam direction through electrical reconfiguration could pose maintenance and spare parts costs. However, utilizing readily available seawater directly as the primary material for reconfiguration presents a promising solution to such challenges as the problems associated with the maritime environment's moisture and the risk of electronic component exposure to water.

CHAPTER 8

CONCLUSIONS AND FUTURE DIRECTIONS

This thesis presents a comprehensive investigation of the application of liquid-assisted microwave components, aiming to overcome the challenges associated with traditional reconfiguration methods. These challenges in electrical methods include distortion of the antenna radiation pattern, high power consumption, maintenance and spare parts costs, durability concerns, and low efficiency due to the discrete nature of PIN diodes. On the other hand, although most of these problems can be solved thanks to optical methods, applying these techniques is considered inconvenient for a low-budget radar application. For this reason, the primary aim of this thesis is to increase the performance of Doppler radar systems by proposing a Doppler radar that works with the liquid-based reconfiguration method. Although liquid-based reconfiguration methods have been featured in the literature before, for the first time in this thesis, we have surpassed the proof-of-concept stage by controlling the operation of a fully functional radar system with a liquid-based approach.

First of all, independent frequency reconfiguration is achieved by applying LM assistance for a novel DP antenna, with the first port operating at 7 GHz and the second at 6.6 GHz. The antenna, which has more than 20 dB isolation, offers significant advantages for communication systems, especially with the 6 GHz band being suitable for unlicensed use. The electrical size of the antenna is significantly smaller than those in the literature. Hence, the simulation and production process is more convenient than SIW structures. The new feature, facilitated by LM, which allows independent reconfiguration of the operating frequency of each port, performs very well with minimal impact on gain and radiation pattern.

Following this, a DB Doppler radar system was created. This radar's key features include Vivaldi antennas using LM control, operating at 2.45 GHz and 5.8 GHz, and an integrated PD designed for LM displacement to enable frequency switching between designated bands. We demonstrate the adaptability of the proposed beam switching method to both SB and DB Vivaldi antennas and highlight the versatility in different frequency bands. Also, integrating an LM-controlled PD provides practicality to the system and allows real-time adjustments without additional attachments. Despite the speed limitations of the dripping method and the high viscosity of the utilized LM, the proposed system provides a basis for future research in automation and viscosity optimization by providing accurate velocity measurements and multiple target detection.

Further, converting the LM-controlled Doppler radar into a water-controlled form is aimed. For this, it is necessary to develop a cavity-based DB dielectric permittivity measurement setup since the dielectric material's properties must be characterized. For this purpose, it is necessary to place the first two modes of a conventional cavity at the operating frequencies of the radar. However, the application of Lagrange multipliers has shown its impossibility. From the ratios of the first two modes' resonant frequencies, which are approximately 1.581 for rectangular cavities and 1.593 for cylindrical cavities, it was determined that such a mode separation is not possible for these two types of cavities since the desired mode placement requires a ratio of approximately 2.37. Numerical simulations and experimental demonstrations reveal ways to exceed established limit values by introducing distortions into the cavity geometry by deviating from idealized rectangular prism or cylindrical structures. Additionally, an LM-made coupler probe was innovatively used to control the coupling factor, enabling both unimodal and bimodal excitation with stability provided by gallium solidification at 29 °C. For testing purposes, dielectric characterization of materials such as glycerin-water mixture and beef liver was carried out using cavities produced by machining, representing one of the proposed cavity types. Results obtained with an iterative method based on liquid mixing exceeded the capabilities of conventional cavity perturbation methods, providing close enough measurements for randomly shaped and high permittivity samples. Although the proposed method is limited by the dielectric properties of the reference materials used, it gives much faster results than other iterative methods as it does not require simulation at every step as long as the material to be measured remains in this range.

Finally, the transformation of the LM-controlled Doppler radar into the water-controlled Doppler radar was carried out. For this purpose, holes were drilled in the cavities of the LM-controlled Vivaldi antennas, allowing water-based material to be placed in these regions. Due to the lower viscosity of water compared to gallium, autonomous control of this structure with a water pump can be achieved at a relatively low cost. The fact that materials such as salt water can be used for this process with innovative designs despite their high losses is an important indicator of the potential of such reconfiguration methods, especially in marine applications.

This thesis signifies not only a substantial contribution to addressing existing challenges in reconfigurable networks but also presents pioneering solutions that illuminate the path for future advancements in the field of liquid-based microwave components. The integration of these innovations holds great promise in reshaping microwave systems by offering flexibility, adaptability, and efficiency in the ever-evolving field of communications and radar systems. In future studies, emphasis can be placed on creating a structure that locks onto the target in the case of moving entity detection or exploring methods beyond multi-target detection, such as classification using various neural network algorithms.

REFERENCES

Abdilla, L., C. Sammut, and L. Z. Mangion (2013). Dielectric properties of muscle and liver from 500 mhz–40 ghz. *Electromagnetic Biology and Medicine 32*(2), 244–252.

Abu Bakar, H., R. Abd Rahim, P. J. Soh, and P. Akkaraekthalin (2021). Liquid-based reconfigurable antenna technology: Recent developments, challenges and future. *Sensors 21*(3), 827.

Al-Yasir, Y. I. A., N. Ojaroudi Parchin, R. A. Abd-Alhameed, A. M. Abdulkhaleq, and J. M. Noras (2019). Recent progress in the design of 4g/5g reconfigurable filters. *Electronics 8*(1), 1–17.

Alqurashi, K. Y., J. R. Kelly, Z. Wang, C. Crean, R. Mittra, M. Khalily, and Y. Gao (2020). Liquid metal bandwidth-reconfigurable antenna. *IEEE Antennas and Wireless Propagation Letters 19*(1), 218–222.

Arbelaez, A., I. Goode, J. Gomez-Cruz, C. Escobedo, and C. E. Saavedra (2020). Liquid metal reconfigurable patch antenna for linear, rh, and lh circular polarization with frequency tuning. *Canadian Journal of Electrical and Computer Engineering 43*(4), 218–223.

Balanis, C. A. (2016). *Antenna Theory: Analysis and Design*. John Wiley & Sons.

Balduino, R., B. McDermott, E. Porter, M. A. Elahi, A. Shahzad, M. O'Halloran, and M. Cavagnaro (2019). Feasibility of water content-based dielectric characterisation of biological tissues using mixture models. *IEEE Transactions on Dielectrics and Electrical Insulation 26*(1), 187–193.

Barrera, J. D. and G. H. Huff (2014). A fluidic loading mechanism in a polarization reconfigurable antenna with a comparison to solid state approaches. *IEEE Transactions on Antennas and Propagation 62*(8), 4008–4014.

Barter, M., S. Partridge, D. R. Slocombe, and A. Porch (2018). Temperature correction using degenerate modes for cylindrical cavity perturbation measurements. *IEEE Transactions on Microwave Theory and Techniques 67*(2), 800–805.

Bennett, E. L., C. Song, Y. Huang, and J. Xiao (2019). Measured relative complex permittivities for multiple series of ionic liquids. *Journal of Molecular Liquids 294*, 111571.

Bharambe, V., D. P. Parekh, C. Ladd, K. Moussa, M. D. Dickey, and J. J. Adams (2018). Liquid-metal-filled 3-d antenna array structure with an integrated feeding network. *IEEE Antennas and Wireless Propagation Letters 17*(5), 739–742.

Bozdag, G. (2014). Novel microstrip antennas for multiband wideband applications. M.Sc. thesis, Izmir Institute of Technology (Turkey).

Carroll, J., G. Paparisto, and D. Vye (2016). The "coffee-can" radar redesigned as an inexpensive RF PCB [application notes]. *IEEE Microwave Magazine 17*(10), 62–74.

Chang, K., Y. Yeh, and J. Lue (2012). Measurement of the dielectric constants of zinc metallic nanoparticles at various frequencies. *Measurement 45*(4), 808–813.

Charvat, G. L., A. J. Fenn, and B. T. Perry (2012). The MIT IAP radar course: Build a small radar system capable of sensing range, Doppler, and synthetic aperture (SAR) imaging. In *2012 IEEE Radar Conference*, pp. 0138–0144. IEEE.

Chen, C.-H., J. Whalen, and D. Peroulis (2007). Non-toxic liquid-metal 2-100 ghz mems switch. In *2007 IEEE/MTT-S International Microwave Symposium*, pp. 363–366. IEEE.

Chen, Z. N. (2016). *Handbook of Antenna Technologies*. Singapore: Springer.

Cheng, E., M. Fareq, A. Shahriman, M. Afendi, Z. Zulkarnay, S. Khor, Z. Liyana, M. Nashrul Fazli, W. Tan, N. Noorpi, et al. (2014). Development of low cost microwave detection system for salinity and sugar detection. *International Journal of Mechanical & Mechatronics Engineering 14*(5), 59–71.

Christodoulou, C. G., Y. Tawk, S. A. Lane, and S. R. Erwin (2012). Reconfigurable antennas for wireless and space applications. *Proceedings of the IEEE 100*(7), 2250–2261.

Curet, S., O. Rouaud, and L. Boillereaux (2008). Microwave tempering and heating in a single-mode cavity: Numerical and experimental investigations. *Chemical Engineering and Processing: Process Intensification 47*(9-10), 1656–1665.

Delgado, D. R., M. Á. Peña, and F. Martínez (2013). Preferential solvation of acetaminophen in ethanol+water solvent mixtures according to the inverse kirkwood-buff integrals method. *Revista Colombiana de Ciencias QuÃmico-Farmaceuticas 42*(2), 298–314.

Dutta, O., M. Jääskeläinen, and P. Meystre (2006). Single-mode acceleration of matter waves in circular waveguides. *Physical Review A 74*(2), 023609.

Ebrahimnejad, A. and S. Nasseri (2009). Using complementary slackness property to solve linear programming with fuzzy parameters. *Fuzzy Information and Engineering 1*(3), 233–245.

Entesari, K. and A. P. Saghati (2016). Fluidics in microwave components. *IEEE Microwave Magazine 17*(6), 50–75.

Fallahi, H., J. Sebek, and P. Prakash (2020). Broadband dielectric properties of ex vivo bovine liver tissue characterized at ablative temperatures. *IEEE Transactions on Biomedical Engineering 68*(1), 90–98.

Fan, C., B. Wu, Y. Hu, Y. Zhao, and T. Su (2019). Millimeter-wave pattern reconfigurable vivaldi antenna using tunable resistor based on graphene. *IEEE Transactions on antennas and propagation 68*(6), 4939–4943.

Federal Communications Commission (FCC) (2020). FCC Opens 6 GHz Band to Wi-Fi and Other Unlicensed Uses. https://www.fcc.gov/document/fcc-opens-6-ghz-band-wi-fi-and-other-unlicensed-uses.

Forouzanfar, M. and M. Joodaki (2018). Systematic design of hybrid high power microwave amplifiers using large gate periphery gan hemts. *AEU-International Journal of Electronics and Communications 84*, 225–233.

Goryashko, V., M. Jobs, L. Duc, J. Ericsson, and R. Ruber (2018). 12-way 100 kw reentrant cavity-based power combiner with doorknob couplers. *IEEE Microwave and Wireless Components Letters 28*(2), 111–113.

Gouveia, D., L. Costa, and M. Valente (2008). Resonant cavity for the measurement of microwave magnetic permeability using the small perturbation theory. *Microwave and Optical Technology Letters 50*(2), 399–402.

Guo, S., B. J. Lei, W. Hu, W. A. Shiroma, and A. T. Ohta (2012). A tunable low-pass filter using a liquid-metal reconfigurable periodic defected ground structure. In *2012 IEEE/MTT-S International Microwave Symposium Digest*, pp. 1–3.

Gutiérrez-Cano, J. D., P. Plaza-González, A. J. Canós, B. García-Baños, J. M. Catalá-Civera, and F. L. Peñaranda-Foix (2019). A new stand-alone microwave instrument for measuring the complex permittivity of materials at microwave frequencies. *IEEE Transactions on Instrumentation and Measurement 69*(6), 3595–3605.

Ha, A., M. H. Chae, and K. Kim (2019). Beamwidth control of an impulse radiating antenna using a liquid metal reflector. *IEEE Antennas and Wireless Propagation Letters 18*(4), 571–575.

Hage-Ali, S., N. Tiercelin, P. Coquet, R. Sauleau, V. Preobrazhensky, and P. Pernod (2010). A millimeter-wave inflatable frequency-agile elastomeric antenna. *IEEE Antennas and Wireless Propagation Letters 9*, 1131–1134.

Hao, J., J. Ren, X. Du, J. H. Mikkelsen, M. Shen, and Y. Z. Yin (2021). Pattern-reconfigurable yagi-uda antenna based on liquid metal. *IEEE Antennas and Wireless Propagation Letters 20*(4), 587–591.

Hayes, G. J., J.-H. So, A. Qusba, M. D. Dickey, and G. Lazzi (2012). Flexible liquid metal alloy (egain) microstrip patch antenna. *IEEE Transactions on Antennas and Propagation 60*(5), 2151–2156.

Hill, D. A. (2009). *Electromagnetic Fields in Cavities: Deterministic and Statistical Theories*. Piscataway, N.J: IEEE.

Hu, T. C. and A. B. Kahng (2016). *Duality and Complementary Slackness*, pp. 61–72. Springer International Publishing.

Hua, C. and Z. Shen (2015). Shunt-excited sea-water monopole antenna of high efficiency. *IEEE Transactions on Antennas and Propagation 63*(11), 5185–5190.

Hua, C., Z. Shen, and J. Lu (2014). High-efficiency sea-water monopole antenna for maritime wireless communications. *IEEE Transactions on Antennas and Propagation 62*(12), 5968–5973.

Hua, C., S. Wang, Z. Hu, Z. Zhu, Z. Ren, W. Wu, and Z. Shen (2021). Reconfigurable antennas based on pure water. *IEEE Open Journal of Antennas and Propagation 2*, 623–633.

Huang, K.-W., M. Bică, U. Mitra, and V. Koivunen (2015). Radar waveform design in spectrum sharing environment: Coexistence and cognition. In *2015 IEEE Radar Conference (RadarCon)*, pp. 1698–1703. IEEE.

Huang, Y., L. Xing, C. Song, S. Wang, and F. Elhouni (2021). Liquid antennas: Past, present and future. *IEEE Open Journal of Antennas and Propagation 2*, 473–487.

Jacobsen, R. E., S. Arslanagic, and A. V. Lavrinenko (2021). Water-based devices for advanced control of electromagnetic waves. *Applied Physics Reviews 8*(041304).

Jha, A. K. and M. J. Akhtar (2014a). A generalized rectangular cavity approach for determination of complex permittivity of materials. *IEEE Transactions on Instrumentation and Measurement 63*(11), 2632–2641.

Jha, A. K. and M. J. Akhtar (2014b). An improved rectangular cavity approach for measurement of complex permeability of materials. *IEEE Transactions on Instrumentation and Measurement 64*(4), 995–1003.

Jiang, Y., H. Zha, J. Shi, M. Peng, X. Lin, and H. Chen (2021). A compact X-Band microwave pulse compressor using a corrugated cylindrical cavity. *IEEE Transactions on Microwave Theory and Techniques 69*(3), 1586–1593.

Jin, G., M. Li, D. Liu, and G. Zeng (2018). A simple planar pattern-reconfigurable antenna based on arc dipoles. *IEEE Antennas and Wireless Propagation Letters 17*(9), 1664–1668.

Jobs, M., K. Hjort, A. Rydberg, and Z. Wu (2013). A tunable spherical cap microfluidic electrically small antenna. *Small 9*, 3230–3234.

Karatay, A. (2022). A symmetrical self-diplexing microstrip antenna with eight-shaped defects. *Journal of Electromagnetic Waves and Applications 36*(16), 2305–2319.

Karatay, A., D. Orcan, C. Özkal, and F. Yaman (2019). Implementation and experimental verifications of microstrip antennas for angular scanning of a Doppler radar. *AEU-International Journal of Electronics and Communications 101*, 76–84.

Karatay, A. and F. Yaman (2024a). Liquid metal-controlled dual-band doppler radar for enhanced velocity measurement. *IEEE Transactions on Instrumentation and Measurement 73*(8001108).

Karatay, A. and F. Yaman (2024b). Liquid metal-tunable miniaturized bimodal cavity for enhanced measurement accuracy in the ism bands. *IEEE Transactions on Instrumentation and Measurement 73*(8001109).

Karatay, A. and F. Yaman (2024c). Mixture-based dielectric permittivity measurements through gallium-excited cavities. *IEEE Transactions on Instrumentation and Measurement 73*(6007808).

Karatay, A., H. Ö. Yılmaz, C. Özkal, and F. Yaman (2023). Cost-effective experiments with additively manufactured waveguide and cavities in the S-band. *Measurement Science and Technology 34*(8), 085904.

Kelley, M., C. Koo, H. McQuilken, B. Lawrence, S. Li, A. Han, and G. Huff (2013). Frequency reconfigurable patch antenna using liquid metal as switching mechanism. *Electronics Letters 49*(22), 1370–1371.

Khan, M. R., G. J. Hayes, S. Zhang, M. D. Dickey, and G. Lazzi (2012). A pressure responsive fluidic microstrip open stub resonator using a liquid metal alloy. *IEEE Microwave and Wireless Components Letters 22*(11), 577–579.

Khan, T., M. Rahman, A. Akram, Y. Amin, and H. Tenhunen (2019). A low-cost cpw-fed multiband frequency reconfigurable antenna for wireless applications. *Electronics 8*(8), 1–17.

Kharkovsky, S. N. and U. C. Hasar (2003). Measurement of mode patterns in a high-power microwave cavity. *IEEE Transactions on Instrumentation and Measurement 52*(6), 1815–1819.

Kik, A. (2016). Complex permittivity measurement using a ridged waveguide cavity and the perturbation method. *IEEE Transactions on Microwave Theory and Techniques 64*(11), 3878–3886.

Kilic, E., U. Siart, O. Wiedenmann, U. Faz, R. Ramakrishnan, P. Saal, and T. F. Eibert (2012). Cavity resonator measurement of dielectric materials accounting for wall losses and a filling hole. *IEEE Transactions on Instrumentation and Measurement 62*(2), 401–407.

Kim, C.-K., L. Minz, and S.-O. Park (2020). Improved measurement method of material properties using continuous cavity perturbation without relocation. *IEEE Transactions on Instrumentation and Measurement 69*(8), 5702–5716.

Kim, H. K., D. Lee, and S. Lim (2016). Wideband-switchable metamaterial absorber using injected liquid metal. *Scientific Reports 6*(1), 31823.

King, A. J., J. F. Patrick, N. R. Sottos, S. R. White, G. H. Huff, and J. T. Bernhard (2013). Microfluidically switched frequency-reconfigurable slot antennas. *IEEE Antennas and Wireless Propagation Letters 12*, 828–831.

Krupka, J. (2006). Frequency domain complex permittivity measurements at microwave frequencies. *Measurement Science and Technology 17*(6), R55.

Kumar, A. (1979). Complex permittivity and microwave heating of pure water, tap water and salt solution. *International Journal of Electronics 47*(6), 531–536.

Kumar, A. and S. Raghavan (2018). Planar cavity-backed self-diplexing antenna using two-layered structure. *Progress in Electromagnetics Research Letters 76*, 91–96.

Kwon, H., G. D'Aguanno, and A. Alu (2021). Optically transparent microwave absorber based on water-based moth-eye structures. *Optics Express 29*(6), 9190–9198.

La Gioia, A., E. Porter, I. Merunka, A. Shahzad, S. Salahuddin, M. Jones, and

M. O'Halloran (2018). Open-ended coaxial probe technique for dielectric measurement of biological tissues: Challenges and common practices. *Diagnostics 8*(2), 40.

Lee, M., H. Son, D. Lim, S. Lee, and S. Lim (2019). Liquid-metal-fluidically polarization reconfigurable microstrip patch antenna. *Microwave and Optical Technology Letters 61*(10), 2306–2314.

Lei, Z., G. Tan, Q. Man, M. Ning, S. Wang, S. Chen, Z. Yang, and R.-W. Li (2021). A flexible metamaterial based on liquid metal patterns embedded in magnetic medium for lightweight microwave absorber. *Materials Research Bulletin 137*, 111199.

Li, B., Y. Yin, Y. Zhao, Y. Ding, and R. Zou (2011). Dual-polarised patch antenna with low cross-polarisation and high isolation for wimax applications. *Electronics Letters 47*, 592–593.

Li, L., X. Yan, H. C. Zhang, and Q. Wang (2021). Polarization-and frequency-reconfigurable patch antenna using gravity-controlled liquid metal. *IEEE Transactions on Circuits and Systems II: Express Briefs 69*(3), 1029 – 1033.

Li, Y. and K.-M. Luk (2015). A water dense dielectric patch antenna. *IEEE Access 3*, 274–280.

Li, Z., C. Wu, Z. Meng, C. Soutis, Z. Chen, P. Wang, and A. Gibson (2022). Accurate thickness measurement of multiple coating layers on carbon fiber composites using microwave cavity perturbation. *IEEE Transactions on Instrumentation and Measurement 71*, 1–10.

Liang, J.-J., G.-L. Huang, K.-W. Qian, S.-L. Zhang, and T. Yuan (2018). An azimuth-pattern reconfigurable antenna based on water grating reflector. *IEEE Access 6*, 34804–34811.

Ling, K., K. Kim, and S. Lim (2015). Flexible liquid metal-filled metamaterial absorber on polydimethylsiloxane (pdms). *Optics express 23*(16), 21375–21383.

McClung, S. N., S. Saeedi, and H. H. Sigmarsson (2018). Band-reconfigurable filter with liquid metal actuation. *IEEE Transactions on Microwave Theory and*

Techniques 66(6), 3073–3080.

Meaney, P. M., C. J. Fox, S. D. Geimer, and K. D. Paulsen (2017). Electrical characterization of glycerin: Water mixtures: Implications for use as a coupling medium in microwave tomography. *IEEE Transactions on Microwave Theory and Techniques 65*(5), 1471–1478.

Motovilova, E. and S. Y. Huang (2020). A review on reconfigurable liquid dielectric antennas. *Materials 13*, 1–28.

Mukherjee, S. and A. Biswas (2016). Design of self-diplexing substrate integrated waveguide cavity-backed slot antenna. *IEEE Antennas and Wireless Propagation Letters 15*, 1775–1778.

Munoz-Ferreras, J.-M., Z. Peng, Y. Tang, R. Gomez-Garcia, D. Liang, and C. Li (2016). Short-range doppler-radar signatures from industrial wind turbines: Theory, simulations, and measurements. *IEEE Transactions on Instrumentation and Measurement 65*(9), 2108–2119.

Murray, C. and R. R. Franklin (2014). Independently tunable annular slot antenna resonant frequencies using fluids. *IEEE Antennas and Wireless Propagation Letters 13*, 1449–1452.

Nandi, S. and A. Mohan (2017). An SIW cavity-backed self-diplexing antenna. *IEEE Antennas and Wireless Propagation Letters 16*, 2708–2711.

Nandi, S. and A. Mohan (2018). SIW-based cavity-backed self-diplexing antenna with plus-shaped slot. *Microwave and Optical Technology Letters 60*, 822–827.

Navarro-Mendez, D. V., L. F. Carrera-Suarez, E. Antonino-Daviu, M. Ferrando-Bataller, M. Baquero-Escudero, M. Gallo, and D. Zamberlan (2015). Compact wideband vivaldi monopole for lte mobile communications. *IEEE Antennas and Wireless Propagation Letters 14*, 1068–1071.

Nawaz, H. and I. Tekin (2015). Dual port single patch antenna with high interport isolation for 2.4 ghz in-band full duplex wireless applications. *Microwave and Optical Technology Letters 58*, 1756–1759.

Nawaz, H. and I. Tekin (2018). Double-differential-fed, dual-polarized patch antenna with 90 db interport rf isolation for a 2.4 ghz in-band full-duplex transceiver. *IEEE Antennas and Wireless Propagation Letters 17*, 287–290.

Nikam, P. B., J. Kumar, V. Sivanagaraju, and A. Baidya (2022). Dual-band reconfigurable ebg loaded circular patch mimo antenna using defected ground structure (dgs) and pin diode integrated branch-lines (bls). *Measurement 195*, 111127.

Nohlert, J., T. Rylander, and T. McKelvey (2020). Cavity resonator sensor and temporal signals analysis for object detection in granular flows. *Measurement 150*, 107027.

Özkal, C. and F. Yaman (2023). A non-resonant approach for dielectric constant reconstructions via newton iterations. *AEU - International Journal of Electronics and Communications 170*, 154802.

Patel, P., K. S. Subramanian, and D. D. Patil (2023). Additively manufactured microfluidically reconfigurable power divider. *IEEE Transactions on Components, Packaging and Manufacturing Technology 13*(11), 1868–1873.

Peng, Z., J.-Y. Hwang, and M. Andriese (2013). Maximum sample volume for permittivity measurements by cavity perturbation technique. *IEEE Transactions on Instrumentation and Measurement 63*(2), 450–455.

Perdana, M., T. Hariyadi, and Y. Wahyu (2017). Design of vivaldi microstrip antenna for ultra-wideband radar applications. In *IOP Conference Series: Materials Science and Engineering*, Volume 180, pp. 012058. IOP Publishing.

Petosa, A. (2012). An overview of tuning techniques for frequency-agile antennas. *IEEE Antennas and Propagation Magazine 54*(5), 271–296.

Pourghorban Saghati, A., J. Batra, J. Kameoka, and K. Entesari (2014). A microfluidically-switched cpw folded slot antenna. In *2014 IEEE Antennas and Propagation Society International Symposium (APSURSI)*, pp. 557–558.

Pozar, D. M. (2011). *Microwave Engineering*. John Wiley & Sons.

Pozar, D. M. and V. Sanchez (1988, June). Magnetic tuning of a microstrip antenna on a ferrite substrate. *Electronics Letters 24*, 729–731.

Pramudita, A. A. and F. Y. Suratman (2021). Low-power radar system for noncontact human respiration sensor. *IEEE Transactions on Instrumentation and Measurement 70*, 1–15.

Qian, Y.-H. and Q.-X. Chu (2017). A polarization-reconfigurable water-loaded microstrip antenna. *IEEE Antennas and Wireless Propagation Letters 16*, 2179–2182.

Ren, Z., S.-S. Qi, Z. Hu, Z. Shen, and W. Wu (2019). Wideband water helical antenna of circular polarization. *IEEE Transactions on Antennas and Propagation 67*(11), 6770–6777.

Ren, Z., S.-S. Qi, W. Wu, and Z. Shen (2021). Pattern-reconfigurable water horn antenna. *IEEE Transactions on Antennas and Propagation 69*(8), 5084–5089.

Robinson, J., S. Kingman, D. Irvine, P. Licence, A. Smith, G. Dimitrakis, D. Obermayer, and C. O. Kappe (2010). Understanding microwave heating effects in single mode type cavities-theory and experiment. *Physical Chemistry Chemical Physics 12*(18), 4750–4758.

Sadiku, M. N. (2000). *Numerical techniques in electromagnetics*. CRC press.

Santra, M. and K. Limaye (2005). Estimation of complex permittivity of arbitrary shape and size dielectric samples using cavity measurement technique at microwave frequencies. *IEEE Transactions on Microwave Theory and Techniques 53*(2), 718–722.

Sanusi, O. M., Y. Wang, and L. Roy (2021). Reconfigurable polarization converter using liquid metal based metasurface. *IEEE Transactions on Antennas and Propagation 70*(4), 2801 – 2810.

Sayem, A. S. M., R. B. V. B. Simorangkir, K. P. Esselle, R. M. Hashmi, and H. Liu (2020). A method to develop flexible robust optically transparent unidirectional antennas utilizing pure water, pdms, and transparent conductive mesh. *IEEE*

Transactions on Antennas and Propagation 68(10), 6943–6952.

Sen, P. and C.-J. C. Kim (2009). Microscale liquid-metal switches - a review. *IEEE Transactions on Industrial Electronics 56*(4), 1314–1330.

Sheen, J. (2009). Measurements of microwave dielectric properties by an amended cavity perturbation technique. *Measurement 42*(1), 57–61.

Sheen, J. and C.-M. Weng (2016). Modifications of the cavity perturbation technique for permittivity measurements of laminated samples. *IEEE Transactions on Dielectrics and Electrical Insulation 23*(1), 532–536.

Shi, Q., Q.-X. Chu, M.-Z. Xiao, F.-C. Chen, X.-Q. Huang, and X. He (2022). Complex permittivity measurement utilizing multiple modes of a rectangular cavity. *IEEE Transactions on Instrumentation and Measurement 72*, 1–8.

Singh, A., I. Goode, and C. E. Saavedra (2019). A multistate frequency reconfigurable monopole antenna using fluidic channels. *IEEE Antennas and Wireless Propagation Letters 18*(5), 856–860.

Smith Jr, R., S. Lee, H. Komori, and K. Arai (1998). Relative permittivity and dielectric relaxation in aqueous alcohol solutions. *Fluid Phase Equilibria 144*(1-2), 315–322.

Song, C., E. L. Bennett, J. Xiao, A. Alieldin, K.-M. Luk, and Y. Huang (2019). Metasurfaced, broadband, and circularly polarized liquid antennas using a simple structure. *IEEE Transactions on Antennas and Propagation 67*(7), 4907–4913.

Stenishchev, I. V. and A. A. Basharin (2017). Toroidal response in all-dielectric metamaterials based on water. *Scientific Reports 7*(9468), 1–9.

Sun, J. and K.-M. Luk (2017). A wideband low cost and optically transparent water patch antenna with omnidirectional conical beam radiation patterns. *IEEE Transactions on Antennas and Propagation 65*(9), 4478–4485.

Sun, J. and K.-M. Luk (2020a). A circularly polarized water patch antenna. *IEEE Antennas and Wireless Propagation Letters 19*(6), 926–929.

Sun, J. and K.-M. Luk (2020b). A wideband and optically transparent water patch antenna with broadside radiation pattern. *IEEE Antennas and Wireless Propagation Letters 19*(2), 341–345.

Sun, J. and K.-M. Luk (2021). A fully transparent wideband water patch antenna with l-shaped feed. *IEEE Open Journal of Antennas and Propagation 2*, 968–975.

Tang, H. and J.-X. Chen (2017). Microfluidically frequency-reconfigurable microstrip patch antenna and array. *IEEE Access 5*, 20470–20476.

Thakur, K. P. and W. S. Holmes (2001). An inverse technique to evaluate permittivity of material in a cavity. *IEEE Transactions on Microwave Theory and Techniques 49*(6), 1129–1132.

Tian, X.-L., C.-X. Hu, D. Zhang, and H.-F. Zhang (2021). A gravity field tailored metamaterial absorber containing liquid metal for polarization separation. *Physica B: Condensed Matter 614*, 413030.

Vahabisani, N., S. Khan, and M. Daneshmand (2017). A k-band reflective waveguide switch using liquid metal. *IEEE Antennas and Wireless Propagation Letters 16*, 1788–1791.

Verma, A. and D. C. Dube (2005). Measurement of dielectric parameters of small samples at x-band frequencies by cavity perturbation technique. *IEEE Transactions on Instrumentation and Measurement 54*(5), 2120–2123.

Wang, M. and Q.-X. Chu (2019). A wideband polarization-reconfigurable water dielectric resonator antenna. *IEEE Antennas and Wireless Propagation Letters 18*(2), 402–406.

Wang, Q., K. Bi, and S. Lim (2020). All-dielectric transparent metamaterial absorber with encapsulated water. *IEEE Access 8*, 175998–176004.

Wang, S., L. Zhu, and W. Wu (2017). A novel frequency-reconfigurable patch antenna using low-loss transformer oil. *IEEE Transactions on Antennas and Propagation 65*(12), 7316–7321.

Wang, X. H., L. Z. Wang, B. M. Zhang, Y. Xu, and X. W. Shi (2021). Design of frequency/passband adjustable filtering power divider based on liquid metal. *IEEE Transactions on Circuits and Systems II: Express Briefs 69*(3), 1074 – 1078.

Wang, Y.-W., G.-M. Wang, and B.-F. Zong (2013). Directivity improvement of vivaldi antenna using double-slot structure. *IEEE Antennas and Wireless Propagation Letters 12*, 1380–1383.

Winston, W. L., M. Venkataramanan, and J. B. Goldberg (2003). *Introduction to mathematical programming*, Volume 1. Thomson/Brooks/Cole Duxbury, Pacific Grove, CA.

Wu, B., Y. Hu, Y. T. Zhao, W. B. Lu, and W. Zhang (2018). Large angle beam steering thz antenna using active frequency selective surface based on hybrid graphene-gold structure. *Optics Express 26*(12), 15353–15361.

Wu, Y.-W., S. Alkaraki, S.-Y. Tang, Y. Wang, and J. R. Kelly (2023). Circuits and antennas incorporating gallium-based liquid metal. *Proceedings of the IEEE 111*(8), 955 – 977.

Xiao, W., Y. Liao, and K. Huang (2022). Measuring electron density of atmospheric microwave plasma jet by microwave perturbation method. *IEEE Transactions on Instrumentation and Measurement 71*, 1–9.

Xing, L., Y. Huang, Q. Xu, and S. Aljaafreh (2015). A wideband hybrid water antenna with an f-shaped monopole. *IEEE Access 3*, 1179–1187.

Xing, L., Y. Huang, Q. Xu, and S. S. Alja'afreh (2015). Overview of water antenna designs for wireless communications. In *2015 IEEE 4th Asia-Pacific Conference on Antennas and Propagation (APCAP)*, pp. 233–234.

Xing, L., J. Zhu, Q. Xu, W. Zhen, and J. Zhou (2019). Possible liquid candidates for liquid microwave components. In *2019 International Symposium on Antennas and Propagation (ISAP)*, pp. 1–3.

Yaghmaee, P., O. H. Karabey, B. Bates, C. Fumeaux, and R. Jakoby (2013). Electrically tuned microwave devices using liquid crystal technology. *International Journal of*

Antennas and Propagation 2013(824214), 1–9.

Yılmaz, H. Ö. and F. Yaman (2019). Metamaterial antenna designs for a 5.8-ghz doppler radar. *IEEE Transactions on Instrumentation and Measurement 69*(4), 1775–1782.

Yu, C., Y. Tu, Y. Zhang, X. He, Y. Li, and E. Li (2021). An improved cavity-perturbation approach for simultaneously measuring the permittivity and permeability of magneto-dielectric materials in sub-6g. *IEEE Access 9*, 14807–14815.

Zhang, G. B., R. C. Gough, M. R. Moorefield, K. J. Cho, A. T. Ohta, and W. A. Shiroma (2018). A liquid-metal polarization-pattern-reconfigurable dipole antenna. *IEEE Antennas and Wireless Propagation Letters 17*(1), 50–53.

Zhang, X., F. Yana, X. Du, W. Wang, and M. Zhang (2020). Broadband water-based metamaterial absorber with wide angle and thermal stability. *AIP Advances 10*(2020), 1–8.

Zhang, X., D. Zhang, Y. Fu, S. Li, Y. Wei, K. Chen, X. Wang, and S. Zhuang (2020). 3-d printed swastika-shaped ultrabroadband water-based microwave absorber. *IEEE Antennas and Wireless Propagation Letters 19*(5), 821–825.

Zhang, Z. and L. Dai (2022). Pattern-division multiplexing for continuous-aperture mimo. In *ICC 2022-IEEE International Conference on Communications*, pp. 3287–3292. IEEE.

Zhou, M., Z. Shen, and J. Xiao, Pan (2016). Frequency-reconfigurable water antenna of circular polarization. *Applied Physics Letters 108*(1), 014102.

Zou, M. and J. Pan (2015). Investigation of resonant modes in wideband hybrid omnidirectional rectangular dielectric resonator antenna. *IEEE Transactions on Antennas and Propagation 63*(7), 3272–3275.

Zou, Y., X. Kong, L. Xing, S. Jiang, X. Wang, H. Wang, Z. Liu, Y. Zhao, and J. Bornemann (2022). A slot antenna array with reconfigurable rcs using liquid absorber. *IEEE Transactions on Antennas and Propagation 70*(7), 6095 – 6100.

VITA

EDUCATION

2020 - 2024 Doctor of Philosophy in Electronics and Communication Engineering

Graduate School, İzmir Institute of Technology, Türkiye

Thesis Title: Fluidically reconfigurable microwave systems with conductive and dielectric liquid materials

Supervisor: Prof. Dr. Mustafa A. Altınkaya

Co-supervisor: Assoc. Prof. Dr. Fatih Yaman

2017 - 2020 Master of Science in Electronics and Communication Engineering

Graduate School of Engineering and Sciences, İzmir Institute of Technology, Türkiye

Thesis Title: Elliptical cavity designs, fabrications and experiments to investigate cell misalignment and surface roughness effects

Supervisor: Assoc. Prof. Dr. Fatih Yaman

2012 - 2017 Bachelor of Electronics and Communication Engineering

Department of Electrical and Electronics Engineering, İzmir Institute of Technology, Türkiye

PUBLICATIONS

SCI/SCI-e Journals

Karatay, A. and F. Yaman (2024). Mixture-based Dielectric Permittivity Measurements through Gallium-Excited Cavities. IEEE Trans Instrum Meas 73, 6007808.

Karatay, A. and F. Yaman (2024). Liquid Metal-Tunable Miniaturized Bimodal Cavity for Enhanced Measurement Accuracy in the ISM Bands. IEEE Trans Instrum Meas 73, 8001009.

Karatay, A. and F. Yaman (2024). Liquid Metal-Controlled Dual-Band Doppler Radar for Enhanced Velocity Measurement. IEEE Trans Instrum Meas 73, 8001108.

Karatay, A., E. Ataç and F. Yaman (2024). Toward Cost-Effective and Lightweight Doppler Radars: Papercraft-Based Components and Comparisons with Aluminum and 3-D Printed Alternatives. IEEE Trans Antennas Propag 72, 1241 - 1249.

Ataç E., A. Karatay and M. S. Dinleyici (2023). Enhancing thickness determination of nanoscale dielectric films in phase diffraction-based optical characterization systems with radial basis function neural networks. Meas Sci Technol 34 (12), 125201.

Karatay, A., H. Ö. Yılmaz, C. Özkal and F. Yaman (2023). Cost-effective experiments with additively manufactured waveguide and cavities in the S-band. Meas Sci Technol 34 (8), 085904.

Karatay, A. (2022). A symmetrical self-diplexing microstrip antenna with eight-shaped defects. J. Electromagn. Waves Appl. 36 (16), 2305-2319.

Karatay, A. and F. Yaman (2021). Electromagnetic effects of equatorially misaligned RF cavities. J Instrum 16 (06), P06014.

Karatay, A. and F. Yaman (2019). Electromagnetic simulations of mechanical imperfections for accelerator cavities. IEEE Trans Nucl Sci 66 (11), 2295-2304.

Karatay, A., D. Orcan, C. Özkal and F. Yaman (2019). Implementation and experimental verifications of microstrip antennas for angular scanning of a Doppler radar. AEÜ-Int J Electron C 101, 76-84.

Conference Proceedings

Karatay, A., B. O. Olcay and F. Yaman (2023). Improving Microwave Component Characterization Using Wavelet Denoising Method. In 31st Signal Processing and Communications Applications Conference, pp. 1-4, IEEE.

Karatay, A., E. Ataç and F. Yaman (2023). An Origami-Inspired Low-Cost Waveguide Design, Fabrication and Measurements for X-band Satellite Communication Systems. In 31st Signal Processing and Communications Applications Conference, pp. 1-4, IEEE.

Kilicgedik A., et al. (2023). Manufacturing and testing of the 800 MHz RFQ at KAHVELab. In 14th International Particle Accelerator Conference, 866-868.

Esen S., et al. (2022). Compact Proton Accelerator in UHF Band At KAHVELab. In 31st Int. Linear Accel. Conf, pp. 1434-437.

Karatay A. and F. Yaman (2019). Fully 3D Printed Bead-Pull Measurement of an Elliptical Cavity. In Book of Full Text Proceedings Turkish Physical Society 35th International Physics Congress, pp. 42-49.